SYNTHESIS AND CHARACTERIZATION OF CONDUCTIVE NANOWIRES USING DNA AS A TEMPLATE

By

SAID AL-GHAMDI

A DISSERTATION

Submitted in partial fulfilment of the requirements

for the degree of Doctor of Philosophy

in the Graduate School of

Newcastle University

Newcastle Upon Tyne, UK

2010

Abstract

The preparation and characterisation of conductive nanowires and nanoropes on DNA templates is the focus of this work. This work is motivated by the search for alternative bottom-up approaches to nanoscale electronics.

The structures and composition of prepared nanowires were determined by Fourier transform infrared (FTIR) spectroscopy, ultraviolet-visible (UV-Vis) absorption spectroscopy, X-ray diffraction (XRD) and X-ray photoelectron (XPS) spectroscopy. The morphology and physical properties were examined by atomic force microscopy (AFM), electrostatic force microscopy (EFM), conductive atomic force microscopy (C-AFM) and two-terminal current-voltage (I-V) measurements using microelectrodes fabricated by photolithography techniques.

Polypyrrole (PPy) nanoropes were formed by chemical polymerization of pyrrole on a DNA template. The diameter of these 'nanoropes' was between 5–30 nm. At room temperature, the conductivity of a PPy-DNA nanorope is confirmed by C-AFM, while the temperature dependence of the conductivity was observed to follow a simple Arrhenius behaviour with a characteristic temperature of T_0 = 4000K.

Silver (Ag) nanoparticle chains were grown along λ-DNA templates using Tollens' reagent under mild conditions (50 ºC, 10 min). UV–Vis spectroscopy of these nanowires exhibited an absorption band at 400-440 nm due to the Ag plasmon. The DNA-templated Ag wires were found to be coated with an oxidized shell. Unlike DNA-templated polypyrrole, these nanowires were often rough. Using metal-binding functionality (alkynyl) introduced into DNA-templated polymer nanowires by chemical modification of the monomer, the morphology of the wire was improved on this hybrid template.

Finally, DNA was used as a template for the growth of cuprous oxide (Cu_2O) nanowires using Benedict's reagent and ascorbic acid as reducing agent at room temperature. AFM showed that these nanowires are uniform and continuous (diameters of 5-30 nm and lengths of 5-16 μm). C-AFM revealed that the average resistance of Cu_2O–DNA nanowires was in the range from 0.13-0.18 MΩ depending on deflection setpoints, which suggests the material is doped. In summary, a range of inorganic and organic materials can be templated on DNA in the form of nanowires and various methods for measuring the conductivity of these nanowires have been established.

Acknowledgments

Firstly, I would like to express my sincere gratitude to my supervisors, Dr. Ben Horrocks and Professor Nick Wright for their valuable guidance, scientific support, and assistance, which made the completion of this work possible. I would like also to thank Professor Andrew Houlton for his encouragement and guidance during Nanowire's group meetings. I am also grateful to my group members, Dr. Stela Pruneanu, Dr. Reda Hassanien, Dr. Scott Watson, Dr. Miguel Galindo and Dr. Andrew Pike for their support and useful discussions. I could never forget the support of other academic staff at Newcastle University and their help and friendship. Special thanks go to Dr. Lidija Siller and her student Ross Little for their help in the XPS analysis. Learning how to handle some of the equipment in the cleanroom needed in fabrication of microelectrodes was not that easy, but the help I received from Dr. Konstantin Vasilevski made it possible. Beside the cleanroom equipment challenge, other equipment posed a softer challenge, i.e. those used in characterization of our nanowires, such as AFM and its modules of application; EFM and C-AFM was also one of the challenges in the early stages of my PhD. Support and help from Prof. Andrew Houlton and Dr. Ben Horrocks by inviting the Veeco technician for training, also made it possible. On the other hand, the chemistry involved in this project would not have happened without the contribution from Dr. Stela Pruneanu and Dr. Reda Hassanien in preparing solutions needed in some of the chemical synthesis. I should also thank Dr. Jerry Hagon for his help in installing and solving software problems I faced during my study. My peers have been great help and support, providing a sound environment, and a useful source of information. Particular mention must go to Dr Tom Hollis, Tim Hawkins and Joseph Hedley and other students in the Chemistry and EECE Schools. I must also thank the Ministry of Higher Education in Saudi Arabia for the financial support without which this work could never have happened. Finally, big thanks goes to my family members, who provided me with an amount of warmth in the cold days, especially my wife and little daughters; Judy and Joanne, who gave me a lot of love, hope and inspiration.

Contents

List of Abbreviations and Symbols

Å	angstrom
AFM	atomic force microscopy
Ag	silver
Al	aluminium
Au	gold
°C	degrees Celsius
C-AFM	conducting atomic force microscopy
CT-DNA	calf thymus DNA
Cu	copper
Cu_2O	cuprous oxide
CuS	copper sulfide
1D	one dimensional
3D	three dimensional
DC	direct current
D	diameter
DMF	dimethylformamide
DNA	deoxyribonucleic acid
poly(dG)	poly guanine
poly(dC)	poly cytosine
eV	electron volt
EFM	electrostatic force microscopy
$FeCl_3$	ferric chloride
E_{Kin}	kinetic energy
E_B	binding energy
FTIR	Fourier transmission infrared

FWHM	full-width-at-half-maximum
f_0	resonance frequency
ϕ	work function
G	conductance
HOMO	highest occupied molecular orbital
HOPG	highly oriented pyrolytic graphite
$h\nu$	photon energy
I-V	current-voltage
IC	Integrated Circuit
In/Ga	indium/gallium
IPA	isopropanol
K	Kelvin
KPM	Kelvin probe microscopy
ℓ	length
LUMO	lowest unoccupied molecular orbital
Me_3SiCl	chlorotrimethylsilane
min	minutes
mM	milli molar
N_2	nitrogen
nm	nanometre
n	integer number
pA	pico amperes
PIn	polyIndole
Py	pyrrole
PPy	polypyrrole
PR	photoresist

QCM	quartz crystal microbalance
RT	room temperature
s	second
SCM	scanning capacitance microscopy
SPM	scanning probe microscopy
STM	scanning tunneling microscope
XPS	X-ray photoelectron spectroscopy
µm	micrometre
λ-DNA	lambda DNA from bacteriophage
θ	reflection angle (theta)
λ	wavelength
UV	ultraviolet
R	resistance
ρ	resistivity
S	Siemens (conductance)
σ	conductivity
VRH	variable-range hopping
UV-Vis	ultraviolet-visible
Ω	ohm (resistance)
Si	silicon
TP	thiophenyl pyrrole
SiO_2	silicon dioxide
XRD	x-ray diffraction

List of Tables

List of Figures

List of Schemes

Chapter 1: Conductive Nanowires; an Introduction

1.1 Background and motivation

There are different techniques that can be used to fabricate nanostructures. Electron beam lithography is one of these techniques and can be used to produce nanostructures with a reasonable level of control [1]. However, sub-100-nanometer writing and printing requires the use of x-rays, electron beams, or focused ion beams [1-3]. Higher energy electrons produce more secondary electrons, which travel through the solid and expose a larger volume of photoresist (PR). This ultimately puts a limit on the smallest achievable feature [2, 3]. Features less than 10 nm are theoretically possible, but rarely demonstrated [4]. For example, Intel Corporation developed extreme-ultraviolet lithography with 13.5 nm wavelength for making future microprocessors. Recently, in a method developed by Linjie *et al*, employing spatial phase-shaping of the deactivation laser beam, a feature down to a 40-nm minimum size was demonstrated [5]. This method is expected to permit printing of circuits and wires with figure sizes less than 30 nm, which is beyond the capability of optical lithography.

As mentioned above, the generation of secondary electrons during electron bombardment and the high cost of the process still make it difficult to achieve sub-10-nm patterns. To overcome these limitations, it is necessary to construct or modify a new generation of technologies, develop new infrastructure and alternative methods. One of these methods is using conductive nanowires templated by DNA as a promising way towards future nanoelectronic devices, which is one of the main objectives of this work.

The aim of this work is to contribute to the development of interconnects that can be used to fabricate future nanodevices. It is expected that investigating new interconnect materials and methods will help to maintain the motivation for alternative future bottom-up approaches. Further, new methods and techniques for conductive nanowire fabrications may lead to a better understanding of their properties.

The importance of this work is that it may lead to improve fabrication of nanowires with potential for use as interconnects in current microdevices. Moreover, non-

lithography-based approaches to form nanostructures may reduce the cost of employing nanostructures and increase their adoption in a range of technologies, including electronics and sensing.

Natta discovered the effect of doping with bromine or iodine on increasing the conductivity of organic polymers in 1958. This was followed by the work of Shirakawa, Macdiarmid and Heeger, who obtained highly conductive polyacetylene thin films in 1977 and stimulated huge interest in such conducting polymers [6]. Many researchers are now investigating conducting polymers owing to their promising technological applications in, e.g., sensing, batteries and plastic electronics. Extensive research has focused on polypyrrole in particular, because of its low cost, mechanical flexibility, electrical conductivity, chemical and thermal stability[7].

Conducting nanowires (1 nm=10^{-9} metres) are made of materials, which are electrically conductive. These nanowires have attracted much interest because of their potential in fabricating future nanodevices. The ability to make a structure made of a conducting polymer by oxidation (p-doping) or reduction (n-doping) has opened the way to the fabrication of many devices such as organic light-emitting diodes [8], field-effect transistors [9, 10] and memory devices [11-13].

1.2 DNA templated nanowire fabrication

DNA, from a biological point of view, will not be considered in this work. Instead it has been utilized as a template to guide the formation of very well defined conductive nanowires with diameters in the range of nanometres. Also, the electrical properties of these nanowires templated by DNA, and the possibility of using them to make simple devices will be considered. The three dimensional (3D) helix structure of DNA [14] will be our template for guiding the assembly of a nanoscopic building blocks to fabricate conductive nanowires. The DNA molecule has a diameter of approximately 2 nm[15]. It contains two antiparallel polynucleotide strands surrounding each other in a helical structure sharing the same axis [16]. The two helices are formed by phosphate deoxyribose backbones linked by hydrogen bonding base pairs (A-T & G-C). A single strand of DNA is shown in Figure 1.1.

The commercial λ-DNA (lambda bacteriophage), used in this work, is about 16 μm

long and contains precisely 48502 base pairs. Since this DNA has a well-defined length, it is an ideal self-assembly template for polymers and inorganic materials that do not naturally form long wire-like structures. Moreover, the negatively-charged phosphate groups allow DNA to interact with positively charged species in a controllable manner and therefore can act as a template for a wide range of organic and inorganic materials prepared from cationic precursors.

DNA templated nanowires are expected to be used in many applications in the future, such as biosensors. Yet, these nanowires must first overcome most of the current difficulties and problems of interconnects fabricated by the conventional lithography technique, such as electromigration [17]. Moreover, nanowires templated by DNA must be easy to align on the substrate surfaces and have the possibility of being integrated in microdevices chips [16].

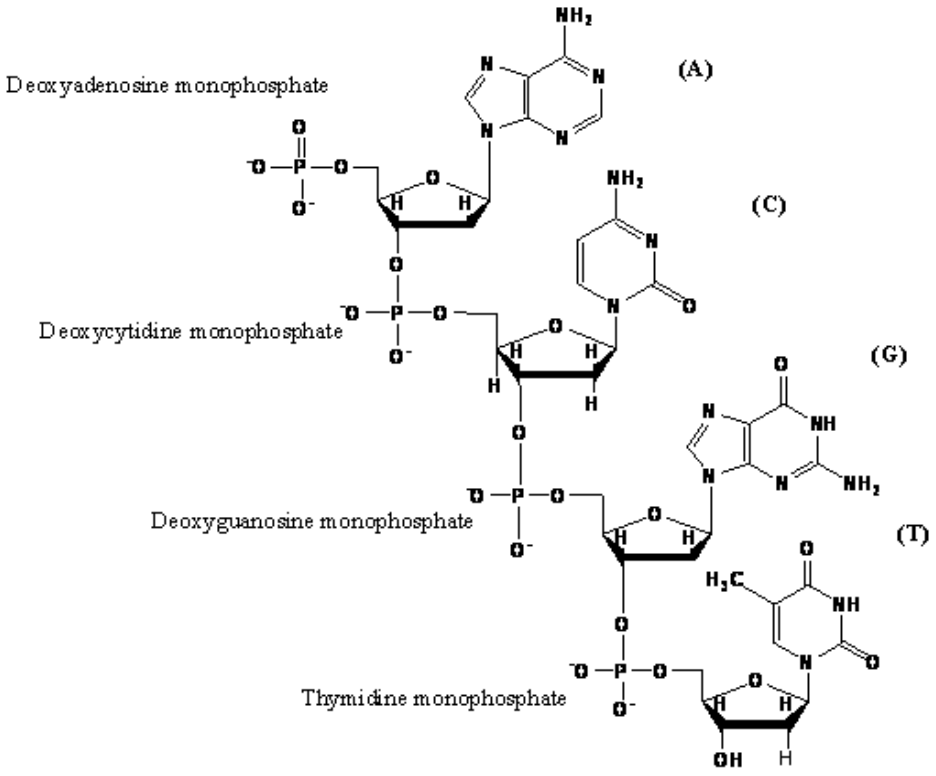

Figure 1.1: Structure of a single strand of DNA showing a chain of four nucleotides [16]

Most of the measurements carried out on DNA revealed that its conductivity is very low [18], and the carrier transport through it follows different behaviours. The reported DNA resistance had different values depending on different factors, such as the

techniques used, equipment employed and experimental conditions. For example, it is reported that a single dry DNA strand behaves as an insulator and its resistance ranges from 10 MΩ to 2 GΩ depending on the quinine-cytosine content in the sequence[19]. While the resistance of a thin film of DNA base sequence (poly(dG)·poly(dC)) under atmospheric conditions was measured and found to be 1.7×10^{10} Ω, whereas under vacuum conditions, it is estimated to be 3.9×10^{12} Ω [20]. Due to its high resistance, DNA prevented its direct use in electronic devices. Because of that, there were many attempts to use DNA as a building block, instead of direct use in fabricating nanodevices by means of what is now called DNA-templated self-assembly [16].

1.3 Polypyrrole-DNA nanowires

Due to its stability and good conductivity under typical atmospheric conditions, Polypyrrole (PPy)[7] has been used in this work to fabricate conductive nanowires templated by DNA. PPy can be made by the chemical or electrochemical oxidation of the pyrrole (Py) monomer [21] to form a chain of Py called PPy, see Figure 1.2 (a) and (b) respectively.

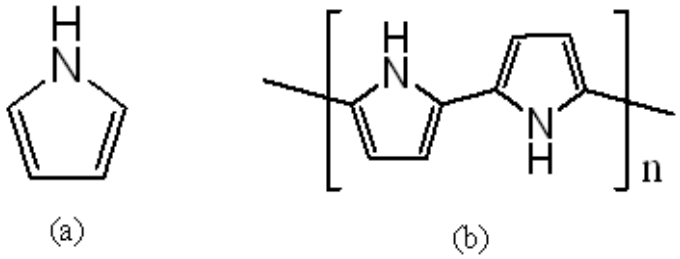

Figure 1.2: a) Structure of Py, an aromatic five membered ring and b) Structure of PPy

Pyrrole can be oxidised to make positive sites (p-doping or holes) that can interact with negative charges of the DNA backbone.

Conducting PPy can be either reduced when doped with electron donors or oxidized when doped with electron acceptors, which causes a significant rise in its electrical conductivity. PPy was discovered to be a conductive material when doped with iodine. As a result, the PPy chains gain positive charges [21]. Since then, researches continued probing its conductivity using different reducing agents. In this work, the focus has

been on using iron trichloride ($FeCl_3$) as an oxidising agent for the PPy as described in reference [22]. This procedure naturally produces cationic PPy (p-doped material).

1.4 DNA templated metal nanoparticles

Metal nanoparticles can also be used to form conductive nanowires templated by DNA. Different transition metals can bind to the nitrogen atoms on DNA bases and to phosphate groups [23]. For example, silver [18, 24], palladium [25], platinum [26], gold [21, 22] or copper [27] nanowires have been successfully used to increase DNA conductivity, which involves the reduction of metal ions bound to DNA. Among metals, silver has attracted a special attention due to its high electrical conductivity, which makes it an excellent candidate for incorporation in micro-electronics.

Owing to the multiple binding sites for metal ions (negatively charged phosphate groups and aromatic bases), DNA has been used also as a template for conducting polymers, as well as for nanoparticles [16]. It has been used as a template for both conductive and semiconductive nanomaterials, including wires and particle arrays [28]. Braun *et al* used DNA as a template for Ag nanoparticles as the first attempt to increase DNA conductivity by templating [18]. He stretched these nanowires across two Au electrodes and measured their resistance. His achievement was also among the earliest to fabricate a nanostructure beyond the limitations of photolithography. More details of Braun's method will be discussed in chapter 4. Dittmer and Simmel have successfully grown copper sulfide (CuS) as a p-type semiconductor on DNA both on a surface and in solution [29]. Several other groups studied the formation of a range of semiconductor nanostructures using DNA as a template [30-32]. The production of nanoscale interconnects using conducting and semiconducting nanowires as building blocks is the basis of what is often called the 'bottom-up' approach to electronic devices.

In this work, DNA is used as a template for Ag metal and semiconducting Cu_2O beside PPy and investigated the possibility of integrating these nanowires into a two terminal electrical device. The preparation and characterisation of these nanowires will be discussed in detail in next chapters.

1.5 The photolithography technique and its limitations

The photolithography technique can be used to pattern microstructured materials. This technique is exploited here to make the microelectrodes as interconnects between the synthesised nanowires and the external electrical test system for electrical characterization. The basic idea of photolithography techniques for microfabrication and some of its limitations will be discussed in this chapter; more details of the photolithography technique used can be found in chapter 2.

In this technique, a series of processes are established in order to transfer patterns onto a substrate using a mask and UV radiation to selectively expose a photoresist (PR) layer in certain areas. The process starts by growing a silicon oxide (SiO_2) layer on a Si substrate by wet or dry oxidation before patterning the structure.

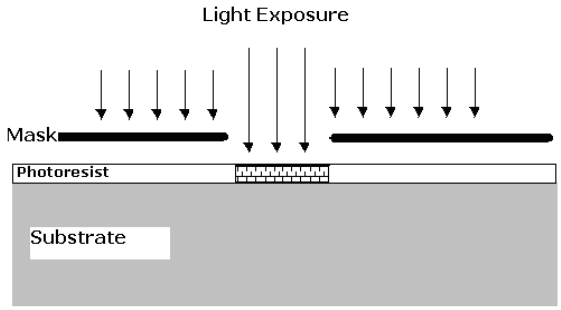

Figure 1.3: Basic schematic diagram of photolithography process

In the photolithography technique, PR is applied by spin-coating upon the surface of the SiO_2/Si substrate, followed by exposure to UV light through a suitable chrome/quartz/glass mask. The mask has opaque areas which prevent certain defined areas of the PR from being exposed to the light, and transparent areas to deliberately expose other areas of the PR to light as shown in Figure 1.3. Positive PR becomes more soluble after exposure to light, leaving unexposed areas as patterns on the SiO_2 surface, whilst negative PR hardens, and so non-hardened regions can be removed chemically. The PR in this case is used as a mask to transfer patterns onto the SiO_2.

In order to transfer the pattern onto the SiO_2, wet (chemical) or dry (plasma) etching can be used to etch those parts of the SiO_2 uncovered by the PR, and then a lift-off process can be used to remove the unwanted PR and mask metals (Cr and Au in this case) deposited on the substrate, leaving the desired thin metal patterns deposited on

the surface. Reactive Ion Etching (RIE) was used to etch the SiO_2 and Electron Beam Deposition (E-Beam) is used to deposit metals onto the substrate surface.

1.5.1 Reactive ion etching (RIE)

RIE is a dry etching technique utilized to pattern microstructures and nanostructures and is an important step in the conventional top-down approach. It is used to remove unwanted regions of material from the SiO_2 surface when bombarded by reactive plasma generated at low pressure in a high intensity electromagnetic field. This environment generates an ionized reactive gas that can be accelerated towards the surface to produce etching.

As depicted in Figure 1.4, two parallel plates are used to create an electric field that accelerates ions in the gas towards the bottom plate, where the sample is located, and physically knocks atoms out of the surface. In Figure 1.4, (1) and (4) denote electrodes used to produce the electric field (3), while (2) represents accelerating ions bombarding exposed regions on the surface of the sample (5). Unlike wet etching, which has limitations of its own, dry etching makes an anisotropic etch, where the etching is unidirectional reducing the undercutting seen during an isotropic etch.

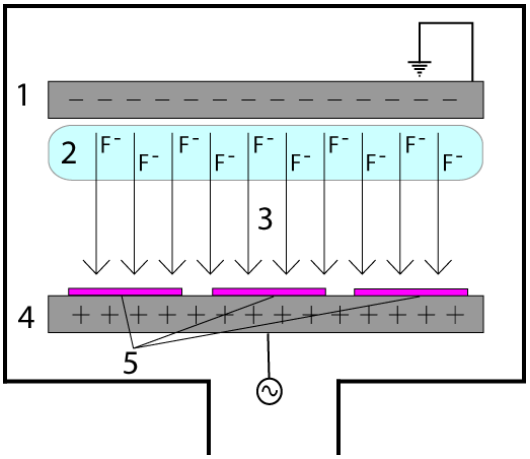

Figure 1.4: Schematic diagram of reactive ion etching (RIE) basic setup. F^- represents accelerated fluorine ions

1.6 Thesis overview

The structure of this work is as follows; Chapter 1, an introduction, presents the background of the thesis and the motivation for the work. It also gives a brief description of the following; DNA templated conductive nanowires and nanoparticles, and the microfabrication and its limitations. Chapter 1 also discusses related work in the field of nanowires fabrications. Chapter 2 reviews techniques used for fabrication and characterizations of nanowires and details of micro-fabrication methods used to fabricate microelectrodes, which enables the study of the nanowire's electrical properties before employing them in more complex circuits. These characterizations are essential to fully explore the nanowire properties. It also reviews the nanowire alignment technique used on Si substrates prior nanowire characterisations. Chapter 3 covers self-assembly of DNA-templated PPy nanowires, and presents the experimental methods used in preparing these samples. Atomic force microscopy (AFM) characterization of fabricated PPy-DNA nanowires and nanoropes, and its structures and mechanism of the self-assembly are also discussed in this chapter. The observation of the conductivity of PPy–DNA nanoropes using conductive atomic force microscopy (C-AFM) as a direct two-terminal method is also investigated. I–V measurements done on a single PPy-DNA nanowire and the temperature dependence of electrical conductivity of PPy-DNA nanoropes are also examined in this chapter. The chapter discusses Fourier transform infrared (FTIR) spectroscopy investigations as a function of temperature for PPy-DNA nanowires; these measurements reveal the extent to which temperature produces chemical changes in the nanowires. The diameter uniformity analysis of PPy-DNA nanowires connecting 2 Au electrodes and the method used to align PPy–DNA nanowires and nanoropes are described. Finally, the chapter presents the temperature-dependent and thermal stability of PPy-DNA nanowires. Chapter 4 discusses synthesis and characterization of Ag nanoparticles templated by DNA. In this chapter, Ag-DNA nanowire preparation is presented along with ultraviolet-visible absorption spectroscopy (UV-Vis), X-ray diffraction (XRD) and X-ray photoelectron spectroscopy (XPS). The morphology and physical properties examined by (AFM), electrostatic force microscopy (EFM) and C-AFM is also presented. In addition, two terminal measurements, temperature-dependent measurements, with FTIR spectroscopy investigations included during the fabrication

process are presented in this chapter. Chapter 5 is on templating Ag nanoparticles on DNA polymer hybrid nanowires and control of the metal growth morphology using functional monomers. It shows how metal-binding functionalities (alkynyl) can be introduced onto DNA-templated polymer nanowires by chemical modification of the 2-(thiophen-2-yl)-1H-pyrrole (TP) monomer, and may be used to improve the morphology of Ag deposited on this hybrid template. AFM, EFM and C-AFM results for morphological and electrical investigations of these nanowires are also presented in this chapter. Chapter 6 covers synthesis and characterization of conductive DNA-templated Cu_2O nanowires. Chemical synthesis, FTIR, UV-Vis absorption spectroscopy, XRD, XPS, AFM and C-AFM characterizations are presented in analysing and characterizing these nanowires. Chapter 7 presents the conclusions, and summarises the findings of this work and the importance of the results achieved and suggests future work. Finally a list of published and pending articles related the subject and a list of references are provided.

Chapter 2: Techniques used for Fabrication and Characterization

2.1 Electrodes fabrication

In this work, microelectrodes were fabricated using gold (Au) (with dimensions shown in Figure 2.1) to facilitate electrical testing of the nanowires. These electrodes are used as an interface between the nanowire and the electrical probe. A summary of the fabrication process can be seen below, while the details of the fabrication process can be found in session 2.5.

First, a thin SiO_2 layer is grown on Si(100) substrate using the dry oxidation process. Trenches are etched by SF_6 ions in the SiO_2 using reactive ion etching (RIE) and filled with Au to ensure that the height of the step at the Au/SiO_2 edge is minimal; this facilitates AFM imaging and also maintains electrical isolation of the electrodes from each other.

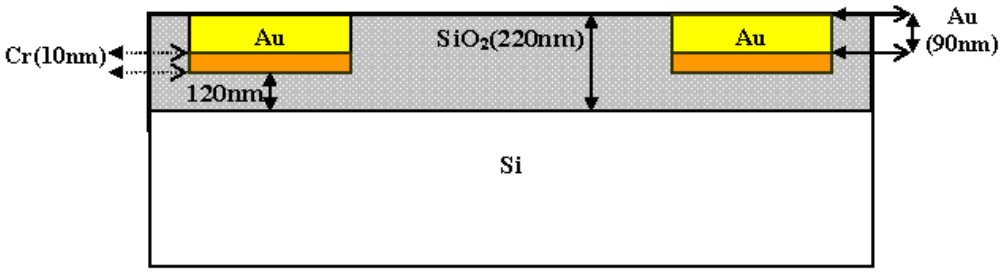

Figure 2.1: Not to scale schematic diagram of the Au electrodes arrangement

Some of the electrodes were fabricated using direct photolithography technique and the others were fabricated using the image reversal positive photoresist (PR) method discussed in the next sections.

2.2 Direct photolithography

The main aim of photolithography is to transfer desired patterns printed in the mask to the substrate covered by photoresist (PR). Subsequent steps of etching and depositions are used to transfer these patterns to the SiO_2 thin layer. These steps are schematically represented in Figure 2.2 and in Figure 2.3, and are described in the following steps:

the substrate surface is cleaned and prepared; then a layer of PR is spun onto the surface, soft baked, and then exposed by UV. Unwanted PR is dissolved with developer, leaving a pattern of the resist on the surface.

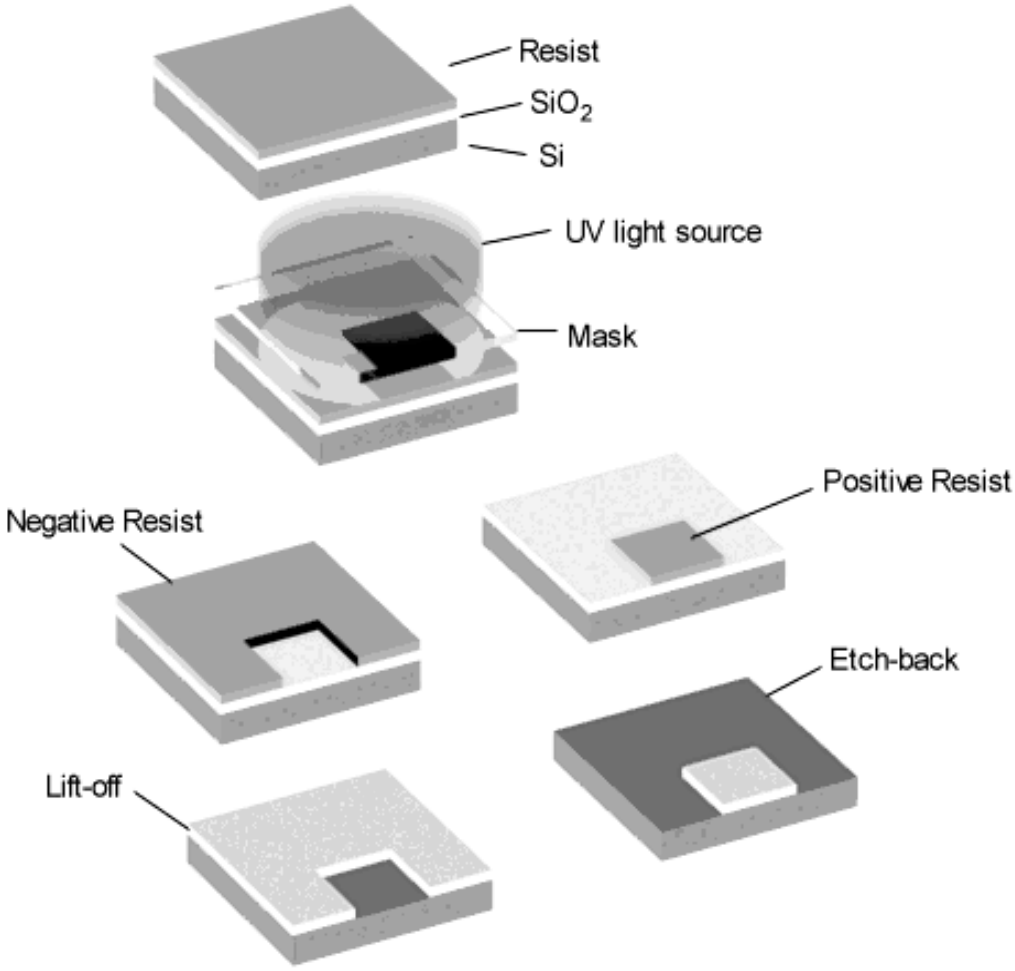

Figure 2.2: Schematic diagram of the main processes in photolithography

Above the PR pattenrs a thin layer of metal can be deposited followed by lift-off process using acetone leaving metal patterns on the surface. On other hand, Al can be used as a second mask before etching SiO_2 using RIE as shown in Figure 2.3.

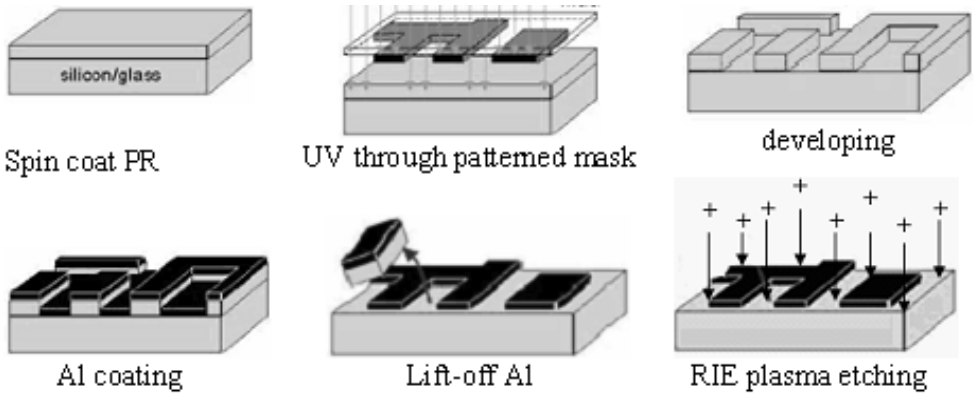

Figure 2.3: Process steps of the Al lift-off and plasma etching

2.3 Image reversal positive photoresist method

To provide undercut profile for lift-off and prevent continuous deposition of metal films over the features, image reversal positive photoresist is used instead of direct photolithography. When this method is used (Figure 2.4), the PR is applied to the surface of the substrate using a spin coater at an appropriate speed; then the substrate is soft-baked. Using a mask aligner, PR is then exposed to UV through a mask with patterns of the electrodes, after that it is baked again (120 °C) and flood exposed without a mask. In this case, previously unexposed PR is removed with the developer. Afterwards, an e-beam coater is used to deposit a thin layer of Al mask all over the sample. Using acetone, the PR and Al layer above it is removed (lift-off), leaving the Al with patterns masking the SiO_2 layer. The patterns are then transferred from the Al mask to the SiO_2 surface by RIE (dry etching). This will allow an adhesion layer, chromium (Cr), and Au to be deposited on the desired areas. Then the Au thin film layer is deposited all over the sample surface, including regions (trenches) that are uncovered by Al. Finally, the Al is removed with etchant with thin metals above it. After removing Al, Au electrodes remain embedded in the SiO_2.

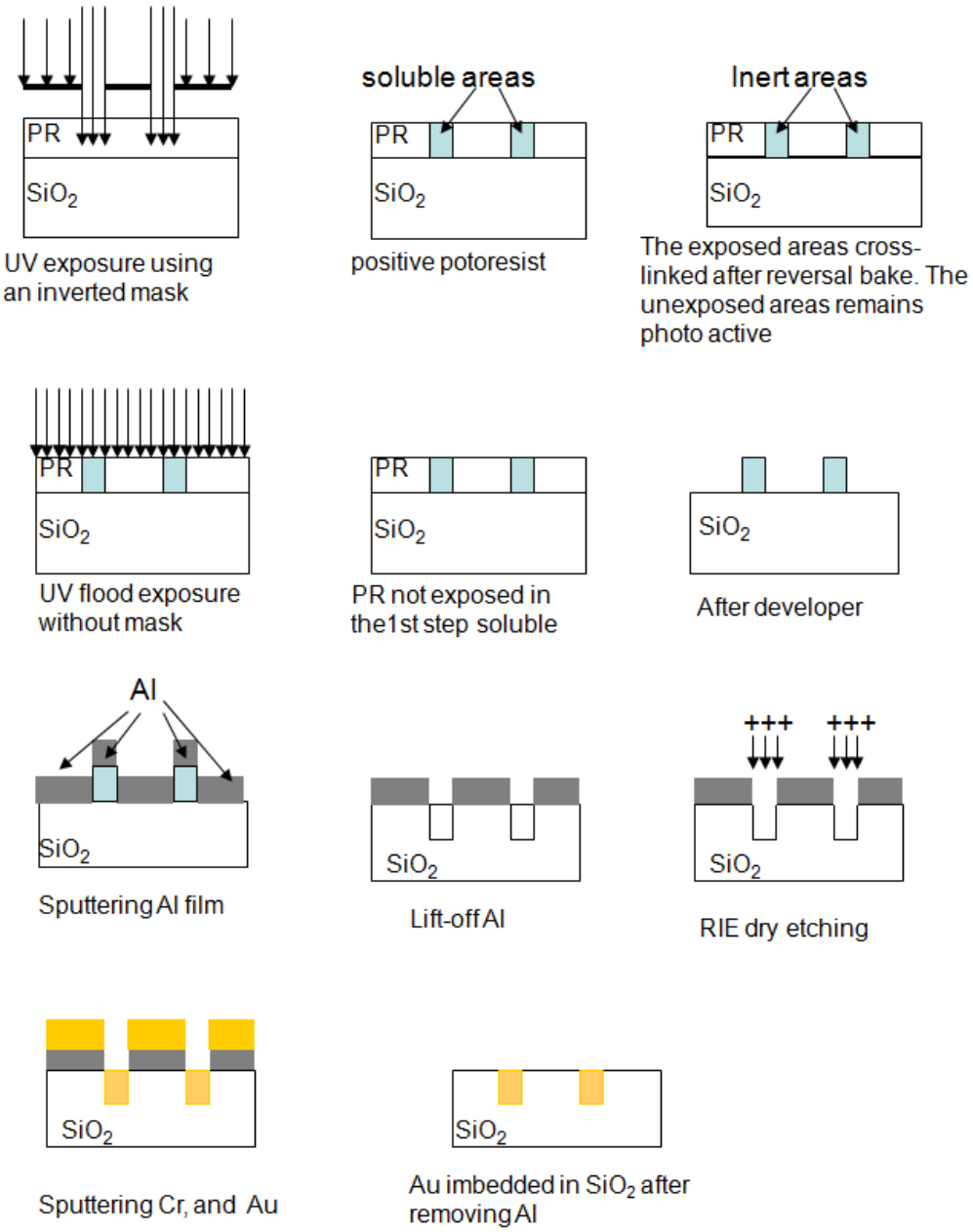

Figure 2.4: Not to scale schematic diagram of the image reversal positive photoresist process

2.4 Substrate cleaning

2.4.1. Preliminary cleaning

Silicon (100) of 100 mm diameter and 525±50 μm thickness and 1-10 Ω cm resistance was used. Substrates were cleaned after cutting into 1x1cm^2 chips using standard cleaning as follows: chips were boiled (~80°C) in trichloroethelene (TCE), (~80°C)

acetone, (~80°C) propan-2-ol (IPA) for 7 minutes in each step.

2.4.2. RCA Cleaning

After standard cleaning, it was found that RCA cleaning is the most suitable method to treat Si substrates before inserting them into the furnace. RCA cleaning can be summarized as follows:

RCA1: Chips were placed in a quartz vat with a mixture of ammonia solution (NH_4OH-20 mL) and hydrogen peroxide (H_2O_2-15 mL) at 70°C under ultrasonic agitation for 2 minutes. The chips were then cleaned with DI water.

RCA2: Chips were transferred carefully into a mixture of 15 mL hydrochloric acid (HCl), 30 % hydrogen peroxide (H_2O_2), and 15 ml ultrapure DI water (H_2O) under ultrasonic agitation at 70°C.

2.4.3. HF cleaning

Chips were inserted into a 40 mL HF(aq) (48%) mixed with 2L of DI water for about 10 seconds. Sample surfaces exhibited hydrophobicity immediately when removed from the solution. Hydrofluoric acid cleaning should be carried out using a polypropylene vessel.

2.4.4. Dry oxidisation

After chips were dried with nitrogen, they were inserted into a furnace at 1100°C with oxygen flow of 80 mL/min using a quartz boat to obtain a layer of oxide of about 250 nm thick. Details of oxidation process can be found in the following section.

2.4.5. SiO_2 Oxidation Growth Rate

Silicon dioxide (SiO_2) is a good insulator used between the Au electrodes. Before the process of electrode fabrication starts, the growth rate of SiO_2 on the Si surface has to first be calibrated to determine the thickness of SiO_2 needed. Thermal oxidation of Si is achieved by heating the substrate in a furnace. Pure oxygen is allowed to flow through the furnace where oxidation takes place. Molecules diffuse easily through the

growing SiO_2 layer at these high temperatures. Oxygen arriving at the Si surface can then combine with silicon to form silicon dioxide. At low SiO_2 thicknesses, i.e. below 0.1 μm, the reaction $Si + O_2 \rightarrow SiO_2$ follows a linear growth law. However, when the SiO_2 layer thickness increases, diffusion through the SiO_2 layer is the dominant growth rate controlling factor. Si chips were inserted into the furnace after it was brought to desired temperature. At certain time intervals, chips were taken out of the furnace. The SiO_2 thickness of each chip was measured several times at different locations on the surface using a Filmetrics F40 thin-film-analyzer. SiO_2 thicknesses were plotted against oxidation time, as shown in Figure 2.5 . As expected, the plotted data was found to have a square root dependence on time, characteristic of diffusion controlled oxidation kinetics.

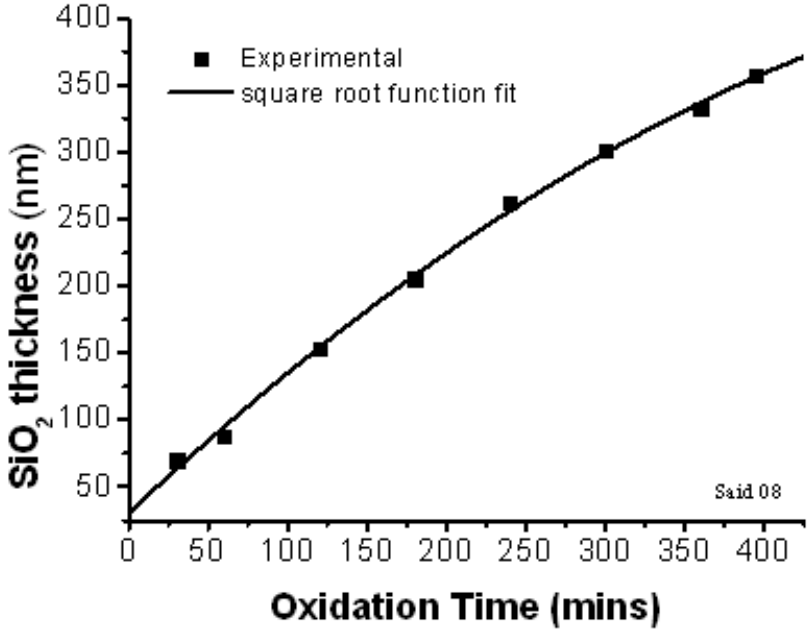

Figure 2.5: Dry oxidation calibration curve. The symbol sizes represent the error range. Oxygen flow rate 80 mL/min. Furnace temperature 1150 °C. Substrate used Si(100) n-type (phosphorus) with resistivity = 1-10 Ω cm

2.5 Direct Photolithography technique

The following steps describe the fabrication process of the Au electrodes using the direct photolithography technique.

2.5.1. Oxidation

A silicon dioxide layer (about 220 nm) is grown on a 1 mm-thick Si(100) wafer using the dry oxidation method described above. The furnace temperature was set to 1100 °C for 6 hours. Since silicon dioxide is a very good insulator, a few micrometers are enough to isolate the Au electrodes from each other electrically.

2.5.2. Cleaning and spin coating

If SiO_2 samples were taken directly from furnace to spin coater, they would not need to be cleaned. Otherwise, samples must be cleaned using the following procedure: O^+ ion sputtering, and then cleaning with acetone and IPA in an ultrasound bath for 10 minutes, then a nitrogen blowgun is used in order to remove any contamination. Then pre-bake the sample for 1 minute, spin coat the PR (3000-5000) rpm for 30 seconds, followed by soft baking at 90°C for 3 minutes.

2.5.3. Mask aligning

A designed mask (few millimeters thick plate with chrome opaque pattern) provided by School of EECE, University of Newcastle, was used. It is usually cleaned by applying acetone and IPA then dried immediately before use. The SLEE Co. Mask Aligner shown in Figure 2.6 and UV exposure are used to print features on the mask onto the PR layer.

2.5.4. Developing

Using mask aligner, positive AZ 5214E PR is used where the region that is exposed to the UV radiation is weakened, and can be easily removed with the developer AZ-326 MIF from A2 Electronic Material (Germany). The transferred patterns are frequently

observed using the microscope. The developing process stops when the sample is rinsed in DI water. Nitrogen blowgun and/or dry spinning are used to remove water before chemical etching. The best results are achieved when UV exposure time is 35-45s and developing time is 50-60s. The developing time changes according to the freshness of the developer itself.

2.5.5. Metal mask deposition

A thin layer of Al (100 nm) is deposited as a second mask all over the sample surface including the PR patterns using an E-beam coater system shown in Figure 2.8. The deposition rate of the Al was 0.14 nm/s at $1.7x10^{-5}$ mbar pressure with 4.9 kV high voltage and 293 mA current. The deposited rate of Al must be as low as possible to prevent Al from accumulating in clusters formed on the SiO_2 surface.

Figure 2.6: SLEE Co. Mask Aligner used in the cleanroom

2.5.6. Lift-off process

Using acetone, the PR and Al layer (120nm) above it are removed, leaving the Al masking the SiO_2 layer and allowing SiO_2 to be etched to the desired thickness, and Au deposited on the etched areas. The lift-off time was 2 hours in acetone.

2.5.7. SiO_2 plasma etching using RIE

In this step, patterns are transferred from Al mask to the SiO_2 surface. The areas on SiO_2, which are not covered by Al that mask the PR are etched using RIE described in chapter 1, section 1.5.1, producing trenches of about 90 nm.

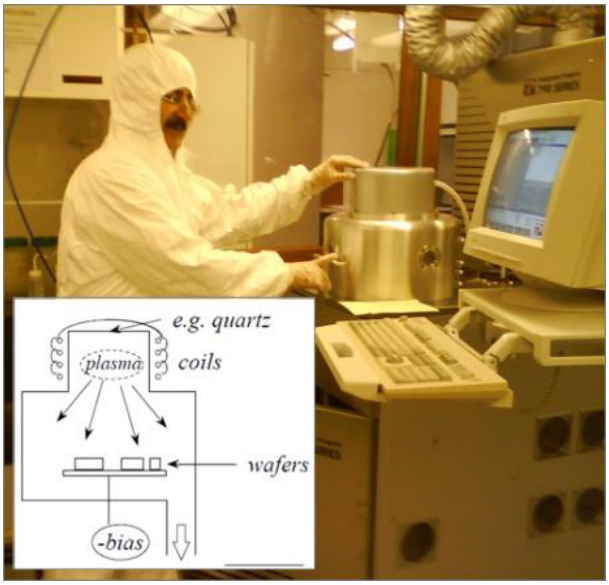

Figure 2.7: Plasma-Therm 790 series RIE machine used in the cleanroom, EECE School, University of Newcastle. Inset: Basic schematic diagram of the RIE machine.

2.5.8. Depositing Au

BOC-Edwards auto e-beam evaporator (Figure 2.8) is used to deposit Au, and the Cr layer on the chip surface, including the trenches made. Samples were then cleaned using a special cleaning recipe, as discussed before, including diluted HF.

Figure 2.8: BOC-Edwards auto e-beam evaporator used to deposit metal thin films, in the cleanroom, EECE School, University of Newcastle

2.5.9. Etching the Aluminium

The Al is etched using suitable chemical etchant called Al etchant (Mixture of H_2O, CH_3COOH, HNO_3 AND $H3PO_4$) with etching rate of 30 nm/min at 30°C. An Au electrode is left embedded in the SiO_2 as a unique chip to facilitate nanowire alignment, AFM imaging and two terminal measurements. After cleaning the sample, Tencor (P-1) Profilometer was used to check the Au thickness. If Au is lower than SiO_2, it is favourable to etch SiO_2 again using RIE.

2.5.10. UV exposure

A spin coater was used at a speed of 3500 rpm for 45 seconds to make a thin layer (3.15 μm) of the photoresist. This was soft-baked at (90 ºC) for 3 minutes before UV exposure (6.0 mW/cm^2 at 405 nm). As mentioned above, the mask is cleaned and a drop of toluene is added on the PR before using the Mask Aligner with UV exposure system. The best result is achieved when exposure time is about 35 seconds and developing time between 50-60 seconds. Positive PR regions that are exposed to the UV radiation are weakened and removed with the developer. For a better result, samples are observed frequently using the microscope (Leitz Wetzlar , Optical Microscope in polarised light). The developing process stops when the sample is rinsed in DI water. Nitrogen blowgun and/ dry spinning is used to remove water before etching. The structure result is shown in Figure 2.9.

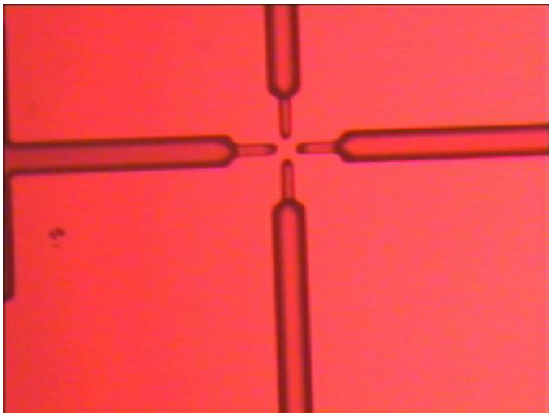

Figure 2.9: Optical image of PR patterns

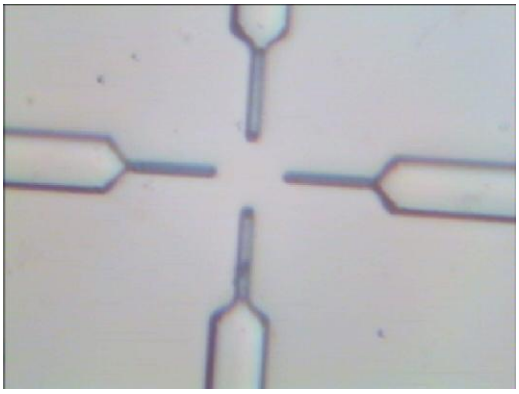

Figure 2.10: A thin layer of Al is deposited all over the sample surface including the PR patterns using E-beam coater

Using acetone, PR and the Al layer above it are removed leaving the Al masking the SiO_2. This will allow Au to be deposited on the desired areas that are etched using the RIE system. The patterns are then transferred from Al mask to the SiO_2 surface, where the areas on SiO_2, not covered by Al, are etched. The thickness of the etched SiO_2 must be in the range of 90 to 150 nm using RIE (Reactive Ion Etching Machine, Plasma-Therm 790 Series) at 150W power, and etching rate, 50 nm/min.

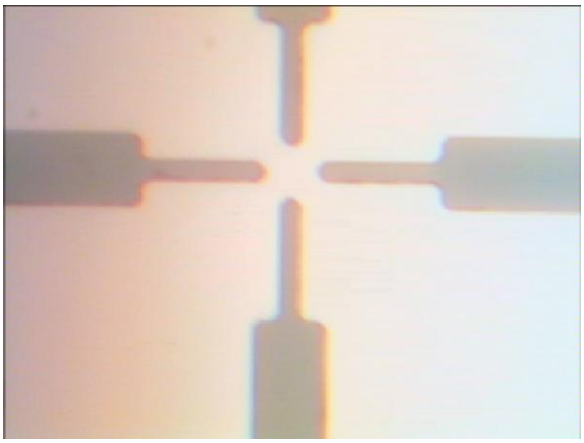

Figure 2.11: Aluminium mask after lift-off

Before depositing Au, a thin layer of Cr (about 10 nm) is deposited using the e-beam evaporator to enhance the adhesion of the Au on the SiO_2. Then a 90 to 150 nm Au thin film is deposited all over the sample surface, including regions that are covered by Al. The Al is then removed as in Figure 2.11 with the Au above it, using the chemical etchant of Al. The etching rate was 30 nm/min at 30 ºC. After removing the Al, the Au electrode is expected to remain embedded in the SiO_2.

2.5.11. Metal deposition and Al lift-off

Samples were placed in the e-beam evaporator and chamber pressure reduced to about $5x10^{-6}$ mbar. An adhesion layer of 10 nm Cr is deposited before the Au is also deposited. The Au layer thickness was in the range 90–100 nm with deposition rate of 0.25 nm/s, current 72 mA and $1x10^{-4}$ mbar pressure.

After the evaporator, vented samples were recovered and placed in Al etchant solution at 30°C for the lift-off process to take place. The Al and unwanted Cr/Au above it are removed (30nm/min). Chips are thoroughly rinsed with IPA and checked with an optical microscope to ensure that all unwanted metals on the chip were etched. Figure 2.12 shows an optical image of Au electrodes embedded into the SiO_2 chips after lifting the Al mask; a cross-section schematic diagram of the electrodes in the inset.

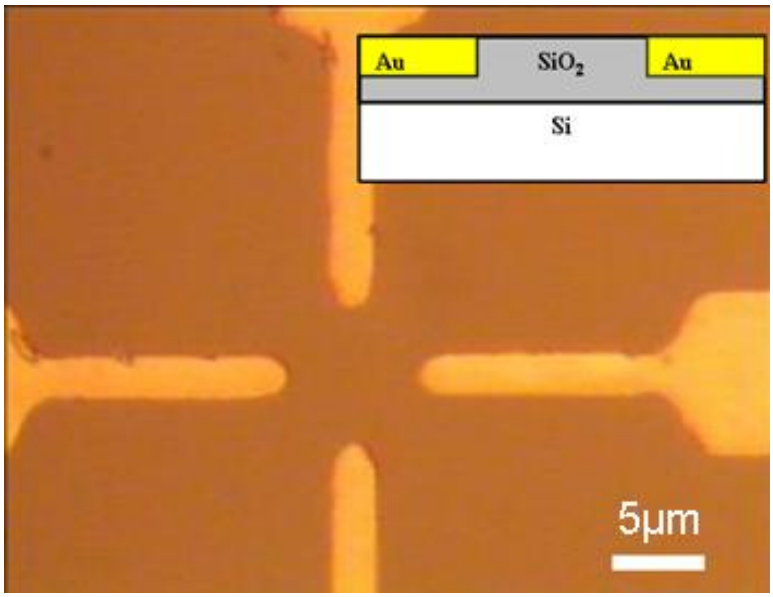

Figure 2.12: Au electrodes embedded into SiO_2 after etching Al. Scale bar 4µm. Inset: a cross-section schematic diagram of the electrodes, scale bar 1.5µm

After cleaning the sample, a Tencor P-1 Profilometer was used to check the level of the Au electrodes with respect to the SiO_2 surface, to see if there was a substantial step at the Au/SiO_2 boundary that would interfere with AFM imaging. If the SiO_2 was found to be above the level of the SiO_2 and Au, it was etched again using RIE.

2.6 Materials

All general chemical reagents were from Sigma–Aldrich and were of Analar grade or equivalent. Lambda DNA was from New England Biolabs, cat no. N30011S (New England Biolabs (UK) Ltd. Hitchin, Herts. SG4 0TY United Kingdom). Pyrrole (Py) was also obtained from Sigma–Aldrich and distilled under N_2. All the solutions were prepared in Ultrapure water; nominal resistivity 18.2 MΩ cm. The chemical reactions were performed in the Chemical Nanoscience Laboratory, School of Chemistry at Newcastle University.

2.7 Alignment of Nanowires

The molecular combing method is used in this work to align nanowires by moving a small drop of solution containing nanowires upon the substrate surface. This method was first developed by Bensimon *et al* (1995) [15, 33]. Molecular combing relies on attachment of one end of the DNA molecule to be aligned to a solid surface and extending the other end by the receding air-water interface on the surface. It utilises the fluid and surface tension forces of the solution drop to elongate the nanowires in the direction of the flow. Yokota *et al* [34] adapted Braun's [18] method to stretch DNA molecules by combing, but including spin coating as well. This technique was utilised and found more reliable, quick and practical technique to align nanowires on SiO_2/Si substrates. In this work, Bensimon's and Braun's methods were adapted, where the drop after spinning is removed by a pipette and/or wicking with filter paper in one direction. This results in aligning individual nanowires upon surfaces or positioning them across Au electrodes for imaging and electrical characterization.

2.8 Nanowires characterisation

The chemical composition of nanowires in a solution was characterized by means of Fourier transform infrared (FTIR) spectroscopy, UV-Vis absorption spectroscopy, X-ray diffraction (XRD) techniques and X-ray photoelectron (XPS) spectroscopy. The morphology and electrical properties of nanowires are studied using different techniques. The morphology of the nanowires was investigated by AFM; while their electrical properties were investigated using EFM, C-AFM and the two-terminal

technique using a probe station and the gold microelectrodes described before. AFM, EFM and C-AFM can also image and measure the dimensions of DNA templates, as well as the templated nanomaterials. The details and underlying concepts of these techniques will be presented in the following sections.

2.8.1 Infrared spectroscopy (IR)

IR spectroscopy is a useful method for determining aspects of the structure of unknown molecules from their infrared spectrum by identifying the frequency of the normal vibrational modes of the molecule. Many of these normal modes are well localised to particular chemical functional groups and can be used to determine particular chemical bonds or functional groups as, e.g., a C-H stretch, the presence of which indicates the presence of carbon-hydrogen bonds. These frequencies are quantised and are slightly different for each molecule; the IR spectrum consists of absorption bands at the relevant frequencies or wavenumbers. The basic principle of operation of IR spectroscopy, in general, is described as follows; A range of frequencies (infrared radiation) are emitted from the source, as depicted in Figure 2.13, and passed through a sample, then the energy of photons with certain frequencies absorbed is measured.

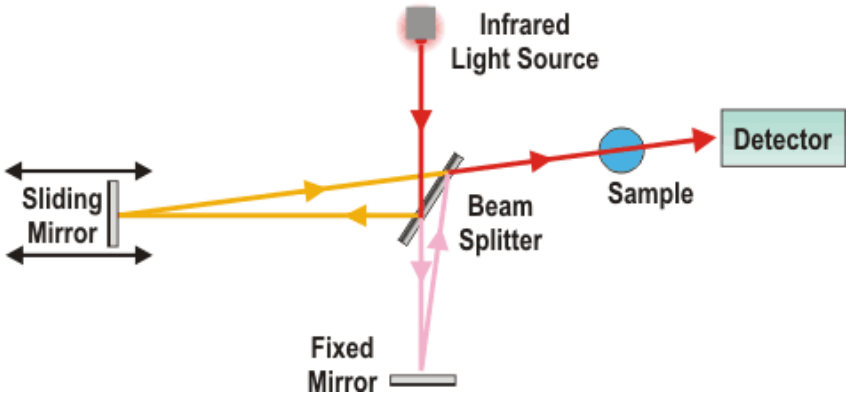

Figure 2.13: Block diagram of FTIR spectrometer

Unlike traditional dispersive instruments- that use a monochromator to focus the IR beam on a grating or prism to be dispersed into a spectrum corresponds to its component wavenumbers- FTIR collects all wavelengths simultaneously resulting in an improvement of its sensitivity. It utilizes a beam splitter to divide the beam that

passes through, and sends one beam to a fixed mirror then back to the beam splitter. The other beam goes to a moving mirror (typically a few millimetres). The path length of the second beam is now variable against that reflected from the stationary-mirror beam due to the motion of the mirror. The two beams combine again at the beam splitter with difference path lengths producing a unique constructive and destructive interference signal (an interferogram). The interferogram produced contains information from every wavelength reflected from or transmitted through the sample in a time-domain form. The fast Fourier transformation mathematical method is then used to extract the intensity of light at each individual frequency using computer software. Different bonds in different materials will absorb different frequencies of the incident beam obtaining spectra with intensity against wavenumbers [35]. In this work, a Biorad FTS-40 and Varian 7000 FTIR spectrometer are used to obtain spectra of the samples in the range from 600 to 4000 cm^{-1} with 4 cm^{-1} resolution. Despite the importance of the FTIR technique in this kind of work, it has some limitations, such as difficulty in analysing spectra obtained with complex mixtures and assigning their peaks.

2.8.2 Ultraviolet-Visible (UV-Vis) absorption spectroscopy

UV-Vis spectroscopy is an absorption spectroscopy technique, in which the transitions are due to excitation of electrons. The technique deals with transitions of molecules or materials from the ground state to an excited state, which can be used to detect very low concentrations of components. UV-Vis spectroscopy utilizes a light source, monochromator (dispersion element), and a detector allied to a personal computer. Usually, a hydrogen or deuterium lamp is used as a source for the UV light, while a tungsten halogen source is used for visible light. At room temperature, all the electrons in the molecules settle in the ground state. These molecules can be excited to a higher energy state when they absorb the energy of incident photons coming from a source. The source should emit a continuous range of wavelengths in both the UV and visible region. In this work, a spectrophotometer (Thermo Spectronic GENESYS 6) with wavelength range from 250 to 900 nm was used. The double monochromator has more advantages than a single beam in the easy control afforded by using microprocessors. In addition, it has better spectral resolution and higher quality by limiting unwanted

light. As shown in Figure 2.14, two identical beams are allowed to pass to the detector. One of them passes through the sample, while the other passes through a reference solution. The beams have intensities of (I) and (I_0) for sample and reference respectively. The detector records the ratio of the beam intensities of that passed through the sample to that of reference solution. This ratio is then sent by the spectrometer to the computer to determine the absorbance ($\log_{10} I_0/I$) corresponding to the amount of UV absorbed.

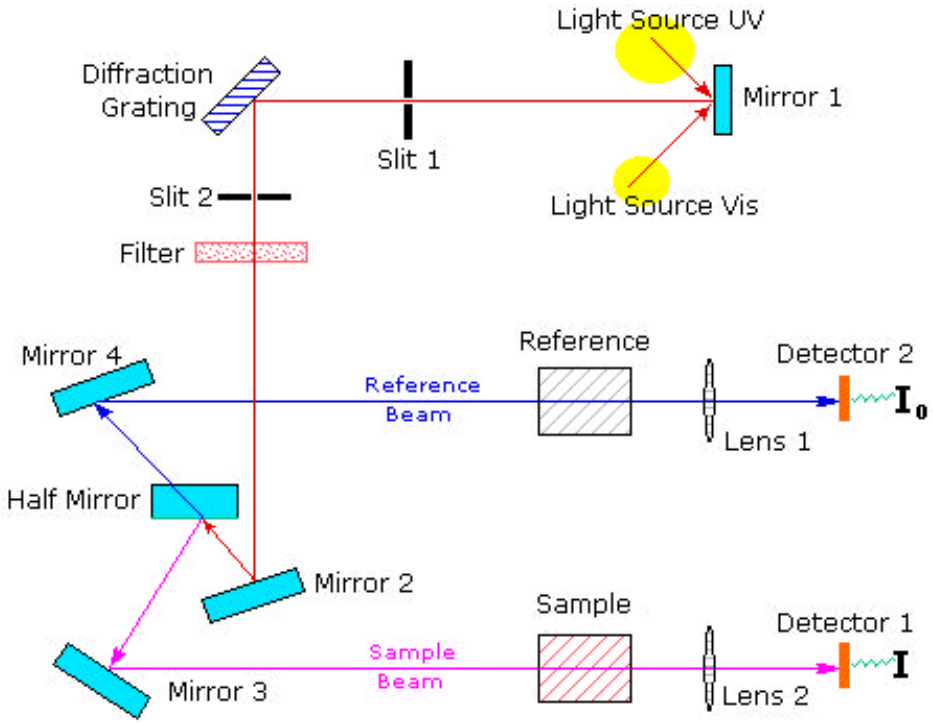

Figure 2.14: Schematic diagram of UV beam path in double beam spectroscopy

The absorbance as a function of wavelength in nm is recorded. Each peak appearing in the recorded spectrum corresponds to the absorption of energy at this wavelength by the molecule in the solution. Positions of wavelengths in the spectrum in which maxima occur correspond to different molecules. Depending on the structure of the molecule, the wavelength position and degree of absorption obtained in the spectrum are considered characteristic of this molecule. In particular, DNA has a strong absorption band centred at about 260 nm.

2.8.3 X-ray diffraction (XRD)

XRD is a useful technique for the structural characterization of nanomaterials. It can be used to determine the precise position of atoms in crystal lattices or ions within a molecule due to the extra energy that can be absorbed by core electrons. XRD can also be used to estimate the particle sizes using the Scherrer formula as in equation 2.1 [36]. The X-ray wavelength (λ) is comparable to the inter-atomic distance, and diffraction of X-rays from a crystal occurs at characteristic angles depending on the lattice plane separation according to the well-known Bragg equation (2.2). The width of the diffracted peaks is related to crystallite size by the Scherrer equation:

$$D = \frac{K\lambda}{\beta\cos(\theta)} \qquad (2.1)$$

Where K is the Scherrer constant, θ is the Bragg angle, β is the line broadening at half maximum intensity in radians and D represents the size of the nanoparticle.

In this work, the PANalytical X'Pert pro multipurpose diffractometer (MPD) fitted with an X'Celerator and a secondary graphite monochromatized Cu K_β radiation (λ = 0.15418 nm) is used. X'Celerator is a movable ultra-fast X-ray detector that uses real time multiple strip (RTM) technology that works by an array of a hundred of detectors simultaneously collecting X-rays diffracted from a sample over a range of 2θ angels. The Bragg relationship holds and can be written as [37]:

$$n\lambda = 2d\sin\theta \qquad (2.2)$$

Where λ is the wavelength of the X-ray, d is the distance between adjacent lattice planes (Figure 2.5), n is the order of reflection and θ is the angle between the incoming X-rays and the normal to the reflecting lattice plane. When X-rays are scattered by the lattice plane, these interfere constructively according to Bragg's Law, enabling calculation of d and obtaining diffractograms as a function of 2θ, while rotating the sample. In Figure 2.15, beam 2 travels $2d\sin\theta$ further than beam 1. If this difference is an integer number of λ, then constructive interference occurs. In the XRD system used, the secondary monochromator eliminates florescent scattering from the specimen and results in better peak to background ratio from sample that contains transition metals and rare earth elements. Diffraction lines occur as a result of the

existence of a certain crystal planes at the correct angles with the incident X-rays creating constructive interference over a range of angels (2θ = 25-80°) with 0.0334° and 150 seconds steps. In case of powder and polycrystalline samples, the configuration of the system is set so that the sample is immobile in the horizontal point while the X-ray tube and the detector both travel simultaneously over the angular range θ. In the polycrystalline sample with all possible *h,k,l* planes, only crystallites having reflecting planes (*h,k,l*) parallel to the specimen surface will contribute to the reflected intensities. If the sample is in a powder form, every possible reflection from a certain set of *h, k, l* planes will have an equivalent number of crystallites contributing to it. Therefore, the incident X-ray beam should be rotated through all angles in order to produce all possible reflections.

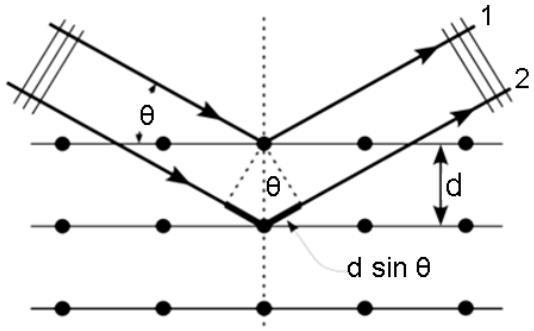

Figure 2.15: Basic feature of X-ray used. Reflection of X-ray from the 1st and 2nd rows of atoms in a solid lattice. The bold line is the path length difference ($2d\sin\theta$) [38]

2.8.4 X-ray photoelectron (XPS) spectroscopy

XPS is also a useful technique to chemically analyse very thin layers (~10 nm) of surfaces. The photoelectric effect is the basis of this technique. When a photon of energy $E = h\nu$ greater than the work function ϕ (the minimum energy required to remove an electron from highest occupied energy level) is incident on a solid, it induces electron emission. In XPS, X-rays can cause photoemission from core (inner quantum shell) or valence levels of a solid surface. In this work, monochromic Al K_α X-ray source is used as the excitation source with photon energy 1486.7eV. Since the core electrons inside the atom are relatively insensitive to their surroundings, but strongly influenced by the Coulomb interaction with the nucleus, their binding energy

E_B is used as a signature of its atomic number. The kinetic energy of emitted photoelectrons is described by the equation [39]:

$$E_{Kin} = h\nu - E_B - \phi \qquad (2.3)$$

The binding energy of the electron in the solid is related to the Fermi level (the highest occupied energy level in the system). Knowing the incident frequency and the work function ϕ, elements can be identified by calculating the binding energy from equation 2.3. The output bands (Figure 2.16b) are displayed as number of electrons detected versus binding energy. The number of electrons can be measured by an electrostatic energy analyser comprising two isolated hemispheres with a potential difference between them as shown in Figure 2.16 (a).

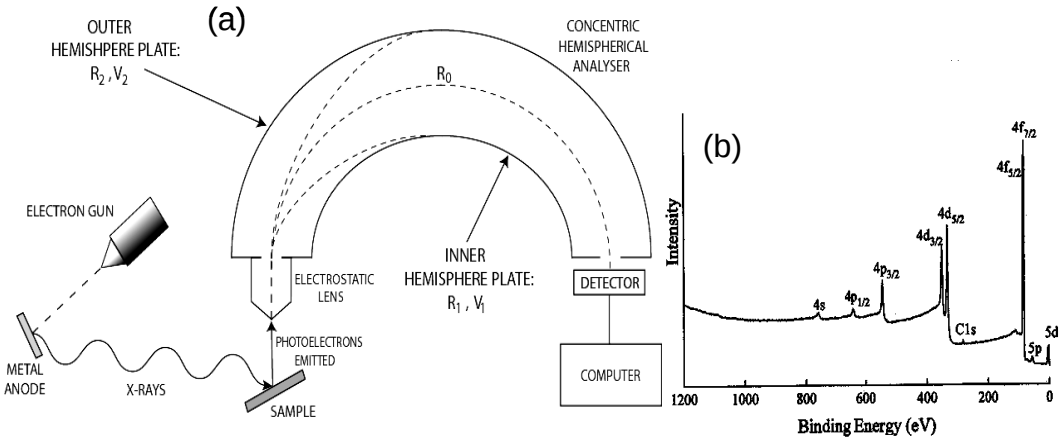

Figure 2.16: a) Schematic diagram of electrostatic energy analyser in the XPS ,b) spectrum obtained from gold sample [39]

For example, the energy spectrum (Figure 2.16b) of gold sample obtained from the ejected electrons with background and resonance peaks suggest information about the sample surface. Peaks in the spectrum correspond to electrons ejected due to the photoelectric effect. The lowest binding energy peaks correspond to emission from the valence band followed by a series of peaks of increasing binding energy. The spectrum also shows a 284 eV binding energy peak suggesting the presence of carbon in the sample surface.

2.9 Characterization with Scanning Probe Microscope (SPM)

2.9.1 Atomic force microscopy (AFM)

In this work, AFM imaging of the nanowires was performed in air using a Dimension Nanoscope V system (Veeco Inc., Metrology group) with 200-250 (μm) long probes at 60-100 (kHz) resonant frequency, a 1-5 (N m^{-1}) spring constant and NanoProbe tips (Veeco Inc.). Vibrational noise was reduced with an isolation system (Manfrotto). All of the AFM height images of nanowires were recorded in Tapping mode™ on bare Si or Si/SiO_2 surfaces at room temperature, unless otherwise indicated.

AFM is a form of SPM invented by Binnig, Gerber and Quate in 1986. It has resolution near the atomic scale. Although not capable of the resolution of Scanning Tunneling Microscope (STM), it has become an indispensable tool in science because it is equally applicable to conducting and non-conducting samples. A schematic diagram of AFM is shown in Figure 2.17(a). It shows that the cantilever oscillates freely at its resonant frequency when it is away from the surface. The piezo crystal attached to the cantilever is used to excite the tip vertically causing the cantilever itself to oscillate. As it oscillates, the photodiode array receives the laser beam that reflected back from the surface causing an electronic signal. The reflected laser beam reveals information (topographical information) about the sample surface under investigation. The resonant frequency of the cantilever is given by the equation[40]:

$$f_0 = \sqrt{\frac{\text{spring constant}}{\text{effective mass}}} \qquad (2.4)$$

A high resonance frequency can be obtained by reducing the cantilever mass. A high resonance frequency makes the scan time shorter. While fabricating a highly flexible cantilever with low spring constant for soft samples is needed to protect from damage during scanning.

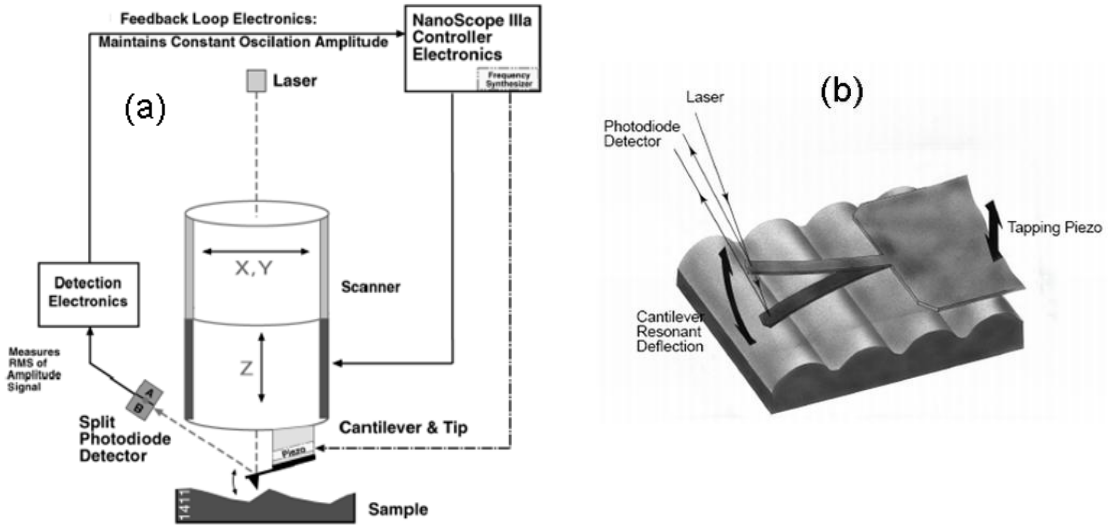

Figure 2.17: (a) AFM schematic representation, (b) tapping cantilever on sample. Reference; di Dimension Instruction manual, Veeco Instruments Inc. 2004 manual

Tapping mode is usually used to image soft samples, such as colloidal particles on a surface, due to reduced frictional and shear forces. Electrical measurements can be made in the AFM system using conductive tips, by directly contacting the sample or by sensing the electrical forces; an EFM phase image can be used to produce images of features in the nanometre size with clearer fine features, alongside electrical information on the sample.

2.9.2 Conductive AFM characterization (C-AFM)

C-AFM techniques can provide direct electrical characterization, as well as the surface topography, of individual nanowires through the use of a metal coated tip to contact the nanowire. The main technical difficulty lies in making a second connection between the nanowire and the external circuit. In C-AFM experiments, single nanowires were selected at the edge of a dense mass of nanowires on a hydrophilic SiO_2/Si substrate [41]. The dense mass of nanowires served as one contact (Figure 2.18), and was itself connected to the metallic chuck using In/Ga eutectic. Alternatively, a single nanowire can be attached to a Au electrode and then eutectic can provide the connection to the Au instead of the dense nanowires as shown in Figure 2.18 (b). The other electrical contact was the tip of a metal coated cantilever; although the tip was located about 1 mm from the In/Ga contact.

The C-AFM images were recorded with different biases applied between the cantilever and the metallic chuck. Zero current was observed when the tip was above bare Si/SiO_2. However, currents were observed when the tip was in contact with the nanowire. After collecting an image, the closed loop positioning system of the Nanoscope V is used to touch the nanowire at defined points and an I-V curve was recorded over a range of bias voltages. The slope of this I-V curve at zero bias was used to estimate the conductance of the nanowire. The data is interpreted in terms of a simple series circuit comprising three resistances; R_{tip} , R_{ext} and R_{wire}. Where R_{tip} is the tip/nanowire contact resistance, R_{ext} is the resistance between the nanowire and the external circuit and R_{wire} is the resistance of the portion of the nanowire between the tip and the main drop deposit. The measured circuit resistance is clearly the sum of these, and it is assumed that all the distance dependence lies in R_{wire}.

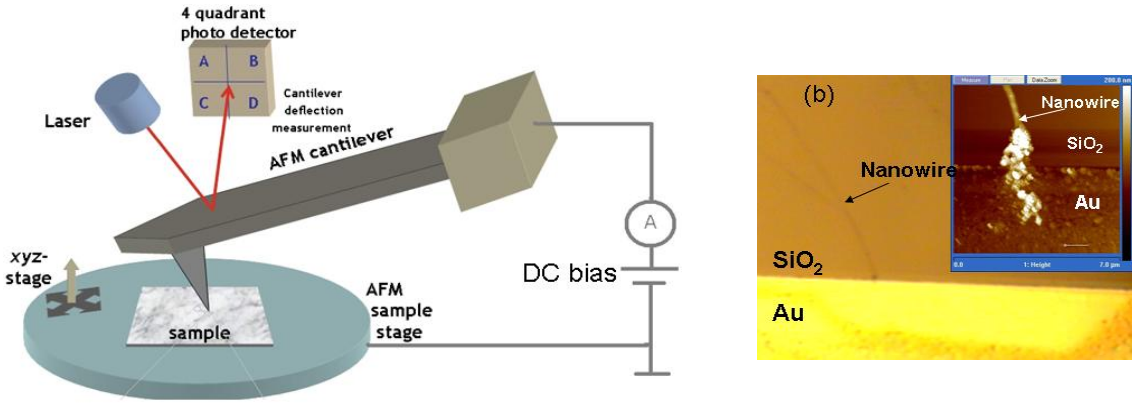

Figure 2.18: (a) Schematic representation of C-AFM measurements, (b) Optical image of nanowire attached to Au electrode, inset; AFM image of the nanowire aligned on the SiO_2, scale bar 1 μm

As an example of using C-AFM to study electrical properties of nanowires, a single conductive nanowire was prepared and aligned on a SiO_2/Si substrate then connected to the metallic chuck using the eutectic. The other electrical contact was made with the tip of a metal coated cantilever. The C-AFM image was recorded at a bias range (0-10 V) applied between the cantilever and the metallic chuck. The imaged area was about 1mm away from the In/Ga. All the measurements were performed by bringing the tip to a spot on the nanowire, and at the maximum tip indentation. I-V curves were acquired in air and at room temperature. In order to study the change of resistance with length, I-V curves were recorded at different fixed spots along the nanowire with a bias between -7 to 7V,

and prior to the acquisition of I-V data, the loading force applied to the contact was selected. Figure 2.19 shows the resistance change of a single nanowire with distance (the inset of Figure 2.19). In the plot, the circuit resistance increases in a roughly linear manner with *d*, because the current must flow through a longer portion of the nanowire, and $R_{wire}(d)$ is the largest resistance in the circuit. However, to make a quantitative analysis, it is necessary to evaluate also R_{tip} and R_{ext} . Figure 2.19 also shows the effect of increasing the tip/nanowire contact force by increasing the setpoint voltage from 0V to 1.0V. A clear decrease in the intercept on the resistance axis is observed at higher forces, which is expected if R_{tip} rather than R_{ext} is the dominant contribution to this intercept. There is also a small apparent change in the slope of the least square regression lines, which is not expected on the basis of a simple series resistance model of the experiment. However, this effect is probably not statistically significant given the scatter. The slope of the best fit lines gives the nanowire resistance per unit length = $1.0 \pm 0.2 \times 10^{11}$ Ω cm^{-1}. Using the diameter of the nanowire observed in the contact mode image (Figure 2.19 inset), an estimated conductivity of 2.5±0.5 S cm^{-1} for the nanowire was obtained. The error in measuring resistance of the nanowire could be as a result of the roughness of the surface morphology, so it is not appropriate to assume that the contact resistance of the C-AFM is constant at each point along the nanowire.

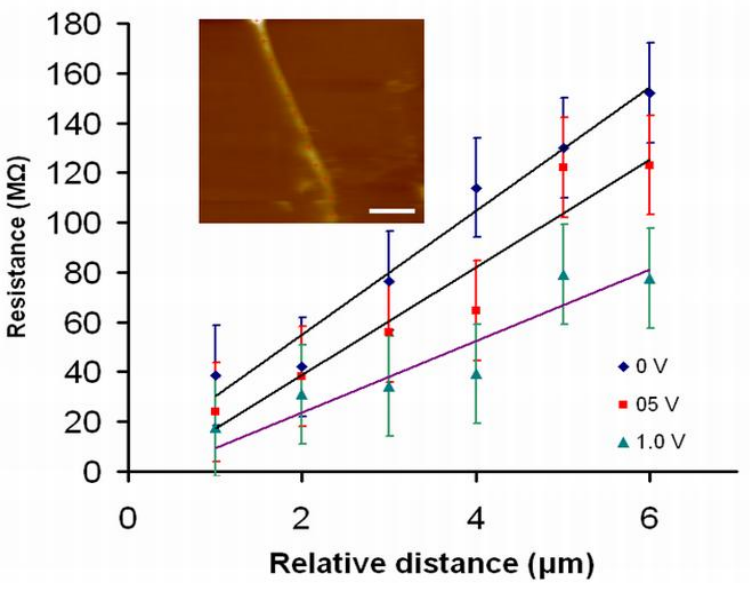

Figure 2.19: PolyIndole-DNA nanowire resistance as a function of tip-contact relative distance for different applied forces. The best fitting lines for the data appear unparallel because of the scatter. The inset shows a C-AFM image of the nanowire, scale bar 1 µm[41]

2.9.3 Electrostatic force microscopy (EFM) characterization

The EFM technique is useful in investigating conductivity of nanostructure materials and determining surface charges distribution. For example, it has been used to detect charges in silicon nanocrystals in SiO_2 dielectric films [42] and semiconductor nanocrystals [43]. Furthermore, it has been used to probe the electrical conductivity of carbon nanotubes and DNA [44, 45], charge distribution or dopant concentration in the nanometre scale [47, 48]. In addition, the EFM technique has been used to measure the permittivity of insulating materials, such as polymer fibers [46].

EFM phase imaging maps the force gradient above the sample with the application of a DC potential bias between the sample and the tip and observing the phase angle between the driving force applied to the cantilever and the tip response. This has also been called scanned conductance microscopy, because conductive objects on a dielectric film modify the capacitance between the tip and the substrate in a manner distinct from that due to polarisable insulators [51].

In EFM measurements, a DC tip-sample bias is applied with the tip at a fixed height above the nanowire, which is aligned on a dielectric film (SiO_2 in our work) as shown in the schematic diagram (Figure 2.20). Measurements are taken in two passes as depicted in Figure 2.21. During the first pass, the tip performs a main scan in Tapping Mode™ to image the surface topography. The tip is then raised to a specified scan height (>50nm), and a second interleave scan is performed, while maintaining a constant separation between the tip and local surface topography.

In general, EFM maps the attractive and repulsive forces between the tip and the sample as shown in Figure 2.22. The long-range electric forces shift the resonance frequency of the oscillating cantilever. This shift is detected, and produces the phase image.

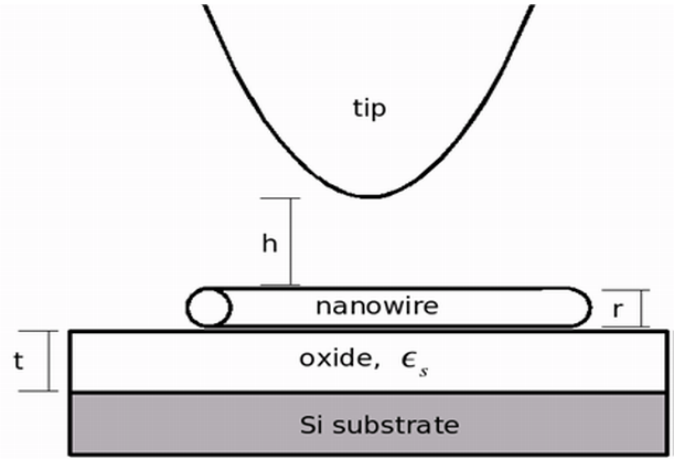

Figure 2.20: Schematic diagram of EFM Lift Mode™ measurement. Nanowire with radius r and length l is aligned on an insulator thin layer of SiO_2 with a thickness t, and scan height *h*

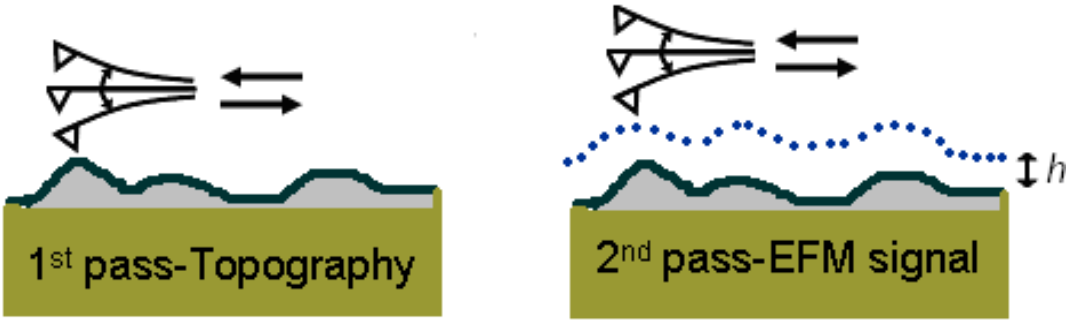

Figure 2.21: Schematic diagram of the EFM two-pass scan

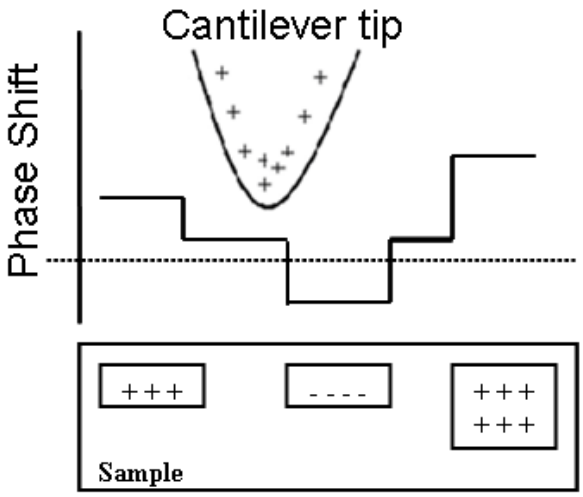

Figure 2.22: Schematic diagram of the attractive and repulsive forces in the EFM experiment

The tip-sample interaction changes the AFM cantilever resonance frequency. The resonant frequency is sensitive to any force gradient. Attractive forces make the cantilever softer reducing its resonant frequency, while repulsive forces make it stiffer increasing its resonant frequency.

One of the advantages of using tapping mode is that it does not disturb or damage the sample under investigation. In EFM experiments, a DC bias is applied between the conductive tip of the cantilever and the sample, with the tip lifted at a fixed height above the nanowire. The phase shift of the cantilever resonant frequency with respect to the driving frequency depends on the DC voltage, and the capacitance between the tip and the underlying substrate. As the tip passes over the nanowire, the phase shifts with respect to the background value over the dielectric/substrate, which forms the phase image are recorded. The phase of the tip motion with respect to the driving force depends on the DC voltage and the capacitance between the tip and the underlying substrate.

2.10 EFM Theory

In literature the cantilever considered as a harmonic oscillator, driven with frequency ω (damping coefficient γ) and resonant frequency $\omega_0 = \sqrt{k/m}$, then the phase shift φ between the driving force and the cantilever resonance frequency ω_0 is given by [46]:

$$\tan\phi = -\frac{\gamma\omega}{\omega_0^2 - \omega^2} \qquad (2.5)$$

From equation (2.5), the phase shift is negative when ($\omega < \omega_0$). Whereas, it is positive when ($\omega > \omega_0$), as can be seen in Figure 2.23.

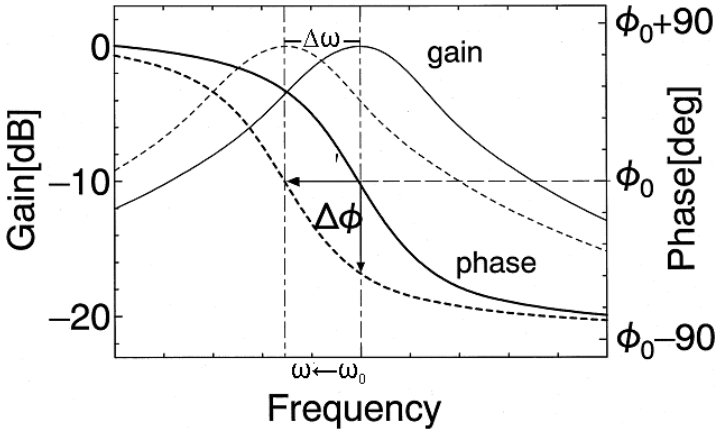

Figure 2.23: Resonance curve. The resonance frequency shifted $\Delta\omega$ from ω_0 to $\omega = \omega_0 + \Delta\omega$, and phase shift $\Delta\varphi$ occurs at the frequency ω_0 [47]

At resonance, the phase shift $\phi = -\pi/2$. But, under usual EFM conventions, the bare substrate exhibits zero phase shift. This is because $\pi/2$ is subtracted from all measured phase shifts:

$$\Phi = \phi - (-\pi/2) = \phi + \pi/2 \qquad (2.6)$$

The energy stored in a spring is given by:

$$E_{spring} = 1/2\ k\ h^2 \qquad (2.7)$$

The energy stored in capacitance is given by:

$$E = 1/2\ C\ V^2 \qquad (2.8)$$

So, the total energy, as a function of *h*:

$$E_{tot} = 1/2\ k h^2 + 1/2 C(h) V^2 \qquad (2.9)$$

$$\frac{\partial^2 E_{tot}}{\partial h^2} = k + 1/2\, C''(h) V^2 = k + \Delta k \qquad (2.10)$$

Where $C(h)$ is the tip-substrate capacitance, k is the spring constant of the cantilever, and V is the bias voltage applied between the tip and the substrate. Therefore, $\frac{1}{2} C''(h) V^2$ is equivalent to a change in k; Δk. For small forces, $F'(h)$ << k, the frequency shift $\Delta\omega$ and the phase shift $\Delta\Phi$ are proportional to the force gradient

$F'(h)$ [54, 55]:

$$\Delta\omega = -(\omega_0/2k)\,F'(h) = -(\omega_0/4k)\,C''(h)V^2 \qquad (2.11)$$

$$\Delta\Phi = -(Q/k)\,F'(h) = -(Q/2k)\,C''(h)\,V^2 \qquad (2.12)$$

Where $C''(h)$ is the second derivative of the tip-sample capacitance, and Q is the quality factor. When the tip is above the substrate, and C_1 is the tip-sample capacitance $F(h) = 1/2\,C_1'(h)V_{tip}^2$, hence a negative phase shift results as shown in Equation 2.12.

$$\tan\Phi_0 = -\frac{Q}{2k}\,C_1''(h)V_{tip}^2 \qquad (2.13)$$

Staii *et al* suggested a model for the wire/substrate capacitance[46]. They considered the tip and sample as a sphere and dielectric plane capacitor. When the tip is at a distance h above bare SiO_2, the second derivative of the capacitance can be written as:

$$C_1''(h) = \frac{2\pi R_{tip}^2\,\varepsilon_0}{(h + t_{ox}/\varepsilon_{ox})^3} \qquad (2.14)$$

Where ε_{ox} is the SiO_2 dielectric constant, t_{ox} is the oxide thickness and R_{tip} is the tip radius. But, when the tip is above the nanowires aligned on the oxide surface, another capacitance $C_2(h)$ should be added with electrostatic force $F_2(h)$ and phase shift Φ :

$$C_2''(h) = \frac{2\pi R_{tip}^2\,\varepsilon_0}{(h + t_{ox}/\varepsilon_{ox} + D/\varepsilon_{nw})^3} \qquad (2.15)$$

Where ε_{nw} is the dielectric constant of the nanowires, and D its diameter.

So, the shift when the electrostatic forces are small can be written as:

$$\tan(\Phi - \Phi_0) \approx \frac{Q}{2k}\,(C_1''(h) - C_2''(h))V_{tip}^2 \qquad (2.16)$$

Equations (2.15) and (2.16) show that the insulating materials always exhibit a positive phase shift with respect to the bare SiO_2 insulators. For conductive, as opposed to merely polarisable materials, the charge can move along the nanowire and the relevant length is the nanowire length, not the tip radius. This increases the effect of the nanowire capacitance in equation 2.15 and can result in a negative phase shift. Further, it predicts a parabolic dependence of the phase shift as a function of the applied bias.

Figure 2.24 and Figure 2.25 illustrate this dependency when applying negative and positive voltages between the tip and the nanowire aligned on SiO_2.

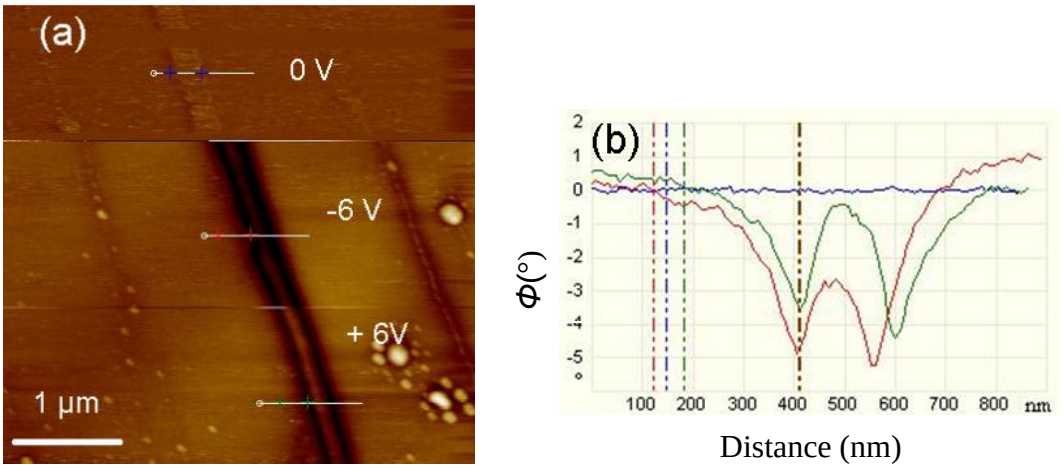

Figure 2.24: (a) EFM phase image of Cu_2O-DNA nanowire when a bias of 0, -6 and +6 V was applied between the cantilever's tip and the substrate. Scale bar 1µm and scale height 3°. (b) Cross section profile of blue, red, and green lines corresponds to 0, -6 and +6 V respectively

As shown in Figure 2.24 and Figure 2.25, when the sum of the two forces is larger than each individual one, the phase shift shows a darker area when the cantilever is on each side of the nanowire. Therefore, the EFM phase image of the nanowire exhibits a double negative phase shift corresponding to the dark line on each side (Figure 2.25b).

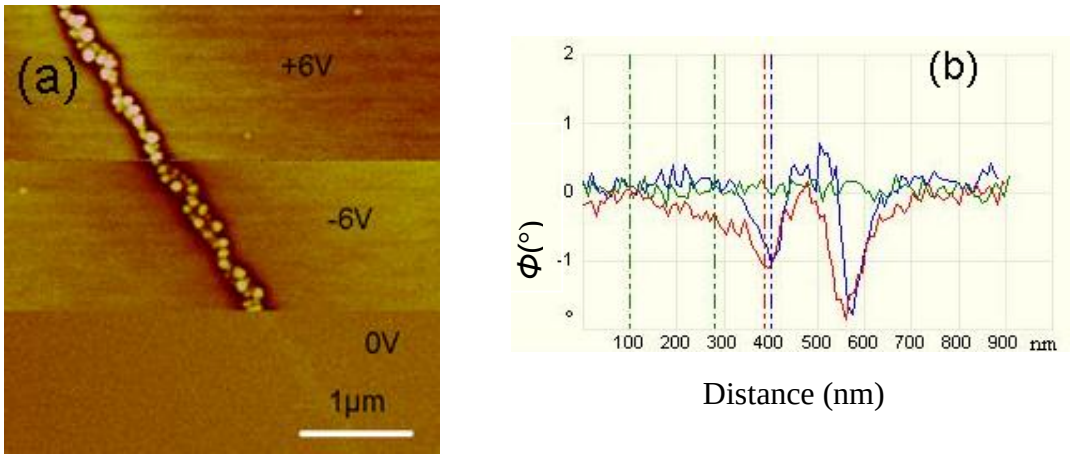

Figure 2.25: (a) EFM phase image of Ag-DNA nanowire when a bias of +6, -6 and 0 V was applied between the cantilever tip and the substrate. Scale bar 1µm and scale height 3°. (b) Cross section profile of (a) red, blue and green corresponds to +6 V, -6 V and 0 V respectively

2.11 The conductivity of nanowires and hopping theory

The conductivity σ of wires with diameter larger than 10 nm can be calculated from the resistance R of a material of given cross sectional area A, and length l using equation:

$$\sigma = \frac{l}{RA} \qquad (2.17)$$

Siemens per centimetre (S cm^{-1}) is the unit of the conductivity, which is the reciprocal of resistivity. The conductivity of any material changes with temperature and depending on the direction of this change it is possible to identify the nature of this material (metal, semiconductor etc). The conductivity of an intrinsic semiconductor increases with increasing temperature, because more valence electrons are exited into the conduction band, whereas it decreases in the case of metals (because of electron-phonon scattering). In polymers the situation is different and will be explained in the next paragraphs.

Impurities are exploited to improve the electrical conductivity of semiconductors, as these introduce quantum states in the semiconductor's band gap. Donor dopants (extra electrons) with states below the conduction band can be easily ionised into the conduction band (n-type material). While acceptor dopants (holes) have energy states close to the valence band. When these holes are occupied by electrons from another atom in the system, it leaves a mobile hole in the valence band (p-type material).

In crystalline semiconductors, the lattice is more rigid than in conductive polymers (1D). This means that the wavefunction of the electron (or hole) in a crystalline semiconductor is well described by a Bloch function (plane wave times a function periodic in the lattice). In contrast, because the "lattice" in a polymer chain distorts easily (elastic energy required is much less than in a crystal), the lattice will distort, if it can lower the energy of the charge carrier (holes in our case). The wavefunction in a crystalline semiconductor is delocalized $\psi \approx e^{ikx}u(x)$, where $u(x)$ has the periodicity of the lattice with momentum $p = \hbar k$. However in a polymer the wavefunction typically is more "atomic or molecular" in nature, e.g., $\psi \approx e^{-r/a_0}$ and is localized. There is usually no equivalent of the crystal momentum, k.

By distorting the bond lengths in the polymer chain, the hole can be localised at the cost of an increase in elastic energy and also an increase in kinetic energy (via the uncertainty principle). However, as well as the increase in those contributions to the energy, there is a decrease in localisation because of the greatly increased Coulomb interaction between the hole and the "dopant" anion. In conductive polymers this decrease is very strong and is generally thought to lead to a localisation of the hole (electron) wavefunctions on a length scale equal to few monomer sub units [48].

This difference in the electronic structure between "normal" crystalline semiconductors and conjugated polymers means that the mechanism of charge transport is completely different. For example, electrons in Si accelerate in an electric field and scatter by interaction with lattice vibrations (the quanta of which are called phonons). Whereas, holes or electrons in conjugated polymers make hops between sites, which are localised. The rate of these hops depends on the electric field, the temperature and to the product of concentrations of neighbouring empty and filled sites [49].

Moreover, in conductive polymer doping is not the same as the doping in semiconductors. In the latter, for example doping Si with phosphorus atoms, the Si acquire extra electrons weakly bonded to the nucleus. While in conducting polymer, for example PPy, it can be doped by removing an electron to make positive charges (called radical cations in the chemistry literature and polarons in the physics literature) the PPy must be neutral over all, so counter anions are present. These charges are strongly localized within a region of size 3-4 rings of Py, because of strong electrostatic interaction. They are therefore present at a high concentration when compared to the dopants in crystalline semiconductors. In a semiconductor such as Si the typical dopant density of phosphorus is about 1 dopant/100,000 atoms for material of moderate resistivity.

When applying electric field, in case of polymer samples, two possibilities are expected; first, mobile ions for example chloride ions (Cl^-), tend to move to the positive electrode. On the other hand, positive ions, such as Na^+, will move to the other side (negative electrode). If there are only Cl^- ions as in this case and when apply a bias, Cl^- ions move toward the positive electrode creating a deficit of Cl^- in one

electrode and excess Cl^- on the other electrode as depicted in the schematic diagram (Figure 2.26 b). When a bias is applied, chloride ions move creating a space charge layers on both sides, that means, nearly all the potential appears in the very thin layer in the left hand side of Figure 2.26 (c). In between it is neutral, where most of the potential is dropped. In this case, the result is an I-V curve as shown in Figure 2.26 (d) and by increasing the potential to higher values there are no changes in the current, which tends to saturate. By increasing the potential, the result is to end up with two space charge layers and electroneturality in the middle with chloride ions equal to positive charges at which the electric field equals zero and most of the resistance is in this region. In case of fixed anions (Figure 2.26 e), the space charge layers can be reduced to be very thin by controlling the bias. So, if the bias is increased, the electric field becomes bigger. In this case, the result is an I-V curve as the one shown in Figure 2.26 (f), exhibiting linear response near zero bias and rising approximately exponentially at larger potential differences. Larger potential differences cause migration of anions to diminish the voltage gradient in the polymer, with formation of space charge layers and electrolysis at the electrode/polymer interface as shown in Figure 2.26 (c). In the case when PPy wrapped on the DNA and the charges are the phosphate groups, which are the counter anions, where it cannot move, I-V behaviour as in Figure 2.26 (f) is observed. Equation (2.18) describes accurately this behaviour [49];

$$I = I_o(\exp(-\alpha\, nFV/RT) - \exp((1 - \alpha)\, nFV/RT)) \qquad (2.18)$$

Where V and I_o and α are the potential difference, exchange current and the barrier symmetry factor respectively. This equation describes the linear and the exponential I-V responses at small and large potential differences.

Here, DNA is used as a template for different types of nanomaterials to make conductive nanowires. As discussed in the previous sections, these nanowires can also be doped as in the bulk form to alter conductivity or compose its type. The conductivity of nanowires can be investigated also by other means such as the C-AFM method, the EFM technique and the two-terminal technique. Yet, the two-terminal technique can be used successfully to determine the type of these different nanowires during the temperature dependence of the conductivity experiment.

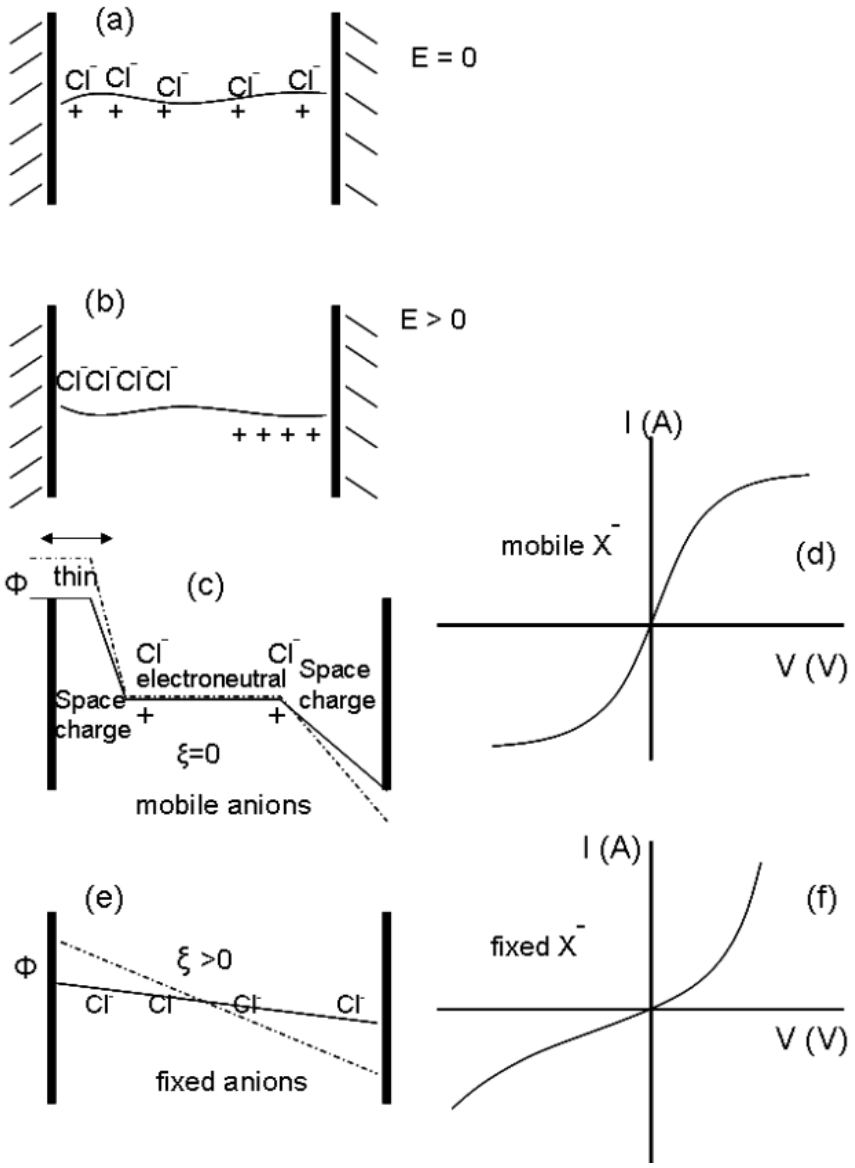

Figure 2.26: Schematic diagram of polymer nanowire between two electrodes and the mechanism of anions migration. (c) and (e) mobile and fixed anions cases with its expected I-V curves

2.12 Temperature dependence of conductivity of nanowires

Metals, semiconductors and conducting polymer are different in the way they conduct. The dominant contribution to the changing of conductivity with temperature in semiconductors is the changing of number of carriers. Therefore, conducting polymers can not be treated as if they are *n* or *p*-type semiconductors. For example, in Si, the electrons can be represented as plane waves and they are moving through the lattice until they scattered by phonon.

As discussed before, in semiconductors, electrons can be described in terms of very well delocalized Bloch function. Whereas, charge carriers in conducting polymer are well localized to particular sites with wavefunctions are more localized and the electronic structure is "molecular-like" and best described by molecular orbital. Though, localized charge carriers can move through the polymer by hopping from one localized site to the next [48, 50, 51].

In this work, I looked at several nanowire types and interpret their I-V characteristics in terms of temperature. I-V measurements were carried out on a single nanowire aligned between Au electrodes and the contact to the electrode pads was made using tungsten probes.

Chapter 3: Self-assembly of DNA-Templated PPy Nanowires: Spontaneous Formation of Nanoropes

3.1 Introduction

As discussed in chapter 1, it is difficult and expensive to achieve nanometre scale dimensions using conventional photolithography. For this reason, significant efforts have been focussed on developing new ways to fabricate at nanostructure dimensions. The bottom-up approach, where nanostructures are assembled from molecules, has become an alternative to top–down approaches.

Using DNA as a template for conductive materials is one of the approaches presented as an attractive method for the development of one-dimensional (1D) structures. Metals such as Au, [52] , Pt [26, 53, 54] and Pd [25] or semiconductors [30-32], and conducting polymers [22] have all been deposited on DNA to prepare conductive nanowires. The advantages of using DNA as a template can be summarized as follows:

First, it is a chemically robust material, which can be obtained in high purity.

Second, single molecules of DNA many micrometres long are available.

Third, DNA composition and structure are well defined which is important because templating reactions rely on the non-covalent interaction of the reagents with the template.

DNA possesses two classes of binding site, anionic phosphate groups and aromatic bases, which have been important for templating reactions. In the case of conductive polymers, the growing cationic polymer chains associate with the anionic phosphate backbone.

This chapter shows that over longer periods of time, a further self-assembly process occurs in which conductive PPy-DNA nanowires form rope-like structures (nanoropes). The conductivity of the nanowires formed by templating PPy on λ-DNA molecules were studied by means of C-AFM and two-terminal I–V measurements on a single nanorope.

A molecular combing method was used to align PPy–DNA nanoropes and make a simple two-terminal electrical device for I-V characterization. It was possible to

image their conducting behaviour by EFM and C-AFM techniques. The atomic force microscopic presented evidence that the 'nanorope' assembly process consists of individual PPy-DNA nanowires twisting around each other.

3.2 PPy–DNA nanowires preparation

A one-pot reaction was performed to synthesise PPy–DNA nanowires as in reference[22]. λ-DNA solution (20 μL; 500 ng μL^{-1} in 10 mM Tris-HCl pH 8 + 1 mM EDTA) is diluted in Nanopure water containing $MgCl_2$ (5 μL; 0.5 mM). The solution was mixed with freshly distilled Py (5 μL; 3mM), then mixed thoroughly. $FeCl_3$ (5 μL; 1 mM), an oxidant, was added and the solution was mixed and incubated at RT.

3.3 PPy–DNA nanowires alignment

To assist with alignment of nanowires and ropes across Au microelectrodes or upon substrate surface, the substrate or the chip was first treated with chlorotrimethylsilane (Me_3SiCl) vapour for 20 min. A methyl-terminated monolayer is formed on the oxide surface due to the reaction between hydroxyl-terminated SiO_2 and Me_3SiCl. This increases the water contact angle and reduces the surface wettability; the hydrophobic surface inhibits the adsorption of the PPy–DNA nanowires and enables one to study individual ropes rather than dense networks that adsorb on hydrophilic surfaces. Following silanization, a drop of PPy–DNA solution (3 μL) was deposited on the chip and after 10 s the drop was dragged using a pipette to align the nanowires across the surface.

3.4 Two-terminal current–voltage measurements

Au microelectrodes were manufactured using standard photolithographic techniques described in chapter 2. The nanowire was aligned between Au microelectrodes for electrical characterization. Each microelectrode (16 μm long, 2.5 μm width) was connected to a larger Au pad (0.5 mm x 1 mm), which served as probe contacts for I–V characterization. The procedure of embedding the Au into the oxide dielectric allowed to use thick, highly continuous, Au films, whilst retaining only a small step height at the Au/oxide boundary. This greatly facilitates the alignment and AFM imaging of the nanowires between electrode pairs.

A Cascade Microtech Summit 11000 series probe station with Hewlett Packard semiconductor device analyzer (HP/Agilent B1500A) controlled by Agilent EasyEXPERT software were used for the I–V measurements. Nanowires were placed inside the chamber of the probe station, which was sited on a vibration isolation table under N_2 gas in order to avoid parasitic currents arising from humid air.

3.5 Electrical measurements using scanning conductance microscopy

Nanowires were prepared by allowing a solution of PPy–DNA nanoropes (2 mL) to dry on a 1 cm^2 SiO_2/Si chip at room temperature for half an hour. The oxide thickness used was 220 nm as determined by the spectrometric thin film analyser (Filmetrics F40). Electrical contact was made by applying a drop of In/Ga eutectic to one corner of the chip and to the chuck. C-AFM and EFM electrical characterization was performed in air on a Dimension Nanoscope V system and on vibrational noise reduction.

For C-AFM and EFM measurements, MESP probes were used (n-doped Si cantilevers, with a metallic Co/Cr coating, Veeco Inc.). These probes are 200–250 μm long, with resonant frequency around 70 kHz, quality factor (Q) about 250, and a spring constant between 1 and 5 N m^{-1}. In our EFM experiments, an independently controlled bias was used to create an electrostatic field between the tip and the sample (the tip was grounded, while the bias was applied at the sample).

The images reported in section 3.6.2 shows the phase of the tip oscillation at a set lift height (50–70 nm typical) above the surface. In this mode, EFM has also been known as scanning conductance microscopy (SCM), because the phase is related to the force gradient and is sensitive to the conductance of nanowires, as well as their polarisability.

For C-AFM measurements, the bias (±10 V) was also applied between the tip and the sample grounded as shown in inset of Figure 3.1. The C-AFM imaging was performed in contact mode, with an applied bias of 9 V. The imaged area was about 1 mm away from the In/Ga contact.

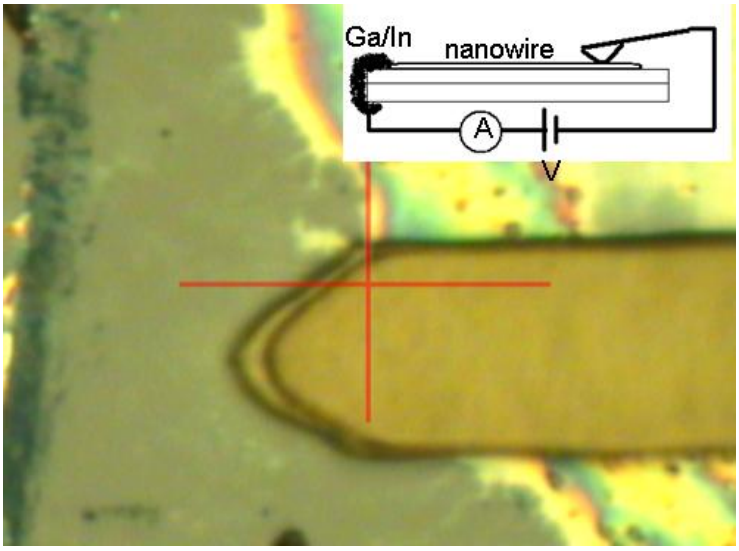

Figure 3.1: Optical image of AFM cantilever and nanowires. Inset; Schematic illustration of the experimental C-AFM set-up used

3.6 Results and discussion

3.6.1 Nanowires fabrication

The classical method of Py oxidation in the presence of $FeCl_3$ has been used for the formation of PPy–DNA nanowires[7]. Self-assembled PPy–DNA nanowires are formed when DNA is added to the polymerization solution as illustrated in Figure 3.2, because cationic PPy is strongly attracted to the anionic phosphate backbone of DNA. Any excess charge is compensated by cations or anions from the solution [22].

PPy–DNA solution was allowed to stand at room temperature and aliquots were removed, deposited on Si/SiO_2 and imaged after standing for different reaction times. The PPy–DNA strands were characterised by two-terminal I–V measurements and confirmed that the different monomer/oxidant ratio produces nanowires of similar conductance to those reported previously [22]. The electrostatic interaction between positive charges of PPy and negative charges of DNA induces the preferential growth of polymer along the DNA chains. With a reaction time of around 3 hours, thin nanowires can be visualised by AFM (apparent diameters between 1 and 3 nm). These nanowires consist of many PPy chains wrapped around a λ-DNA molecule referred to as ‘strands’ or nanowires. A longer incubation time (1–6 days) generates assemblies of nanowire strands, which are referred to as nanoropes (diameters between 5 and 30 nm); Illustration of the assembly of conductive polymer/λ-DNA ropes. The first step is

the templated growth of PPy on λ-DNA (1–3 h); the second step is the slower assembly by twisting or braiding of the PPy–DNA strands into ropes (1–6 days).

AFM images provide a convenient method to observe the polymerization because the apparent height of bare DNA molecules is around 0.5 nm, whereas the templated polymer nanowires are substantially thicker (>2 nm). Despite the fact that apparent heights of DNA molecules revealed by AFM are well known to be less than the true height, the technique nevertheless can detect the thickening of the strands as the polymerization process proceeds.

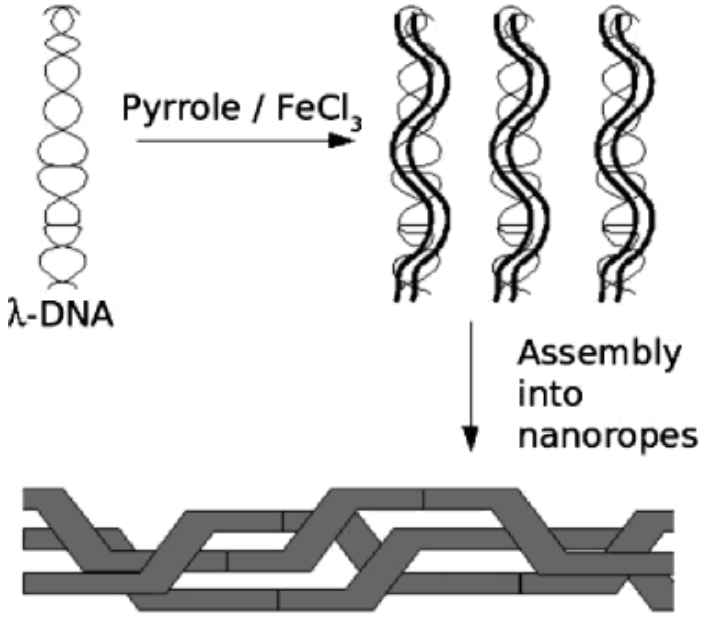

Figure 3.2: Illustration of the assembly of conductive polymer/λ-DNA ropes. The first step is the templated growth of PPy on λ-DNA (1–3 h); the second step is the slower assembly by twisting of the PPy–DNA strands into ropes (1–6 days)

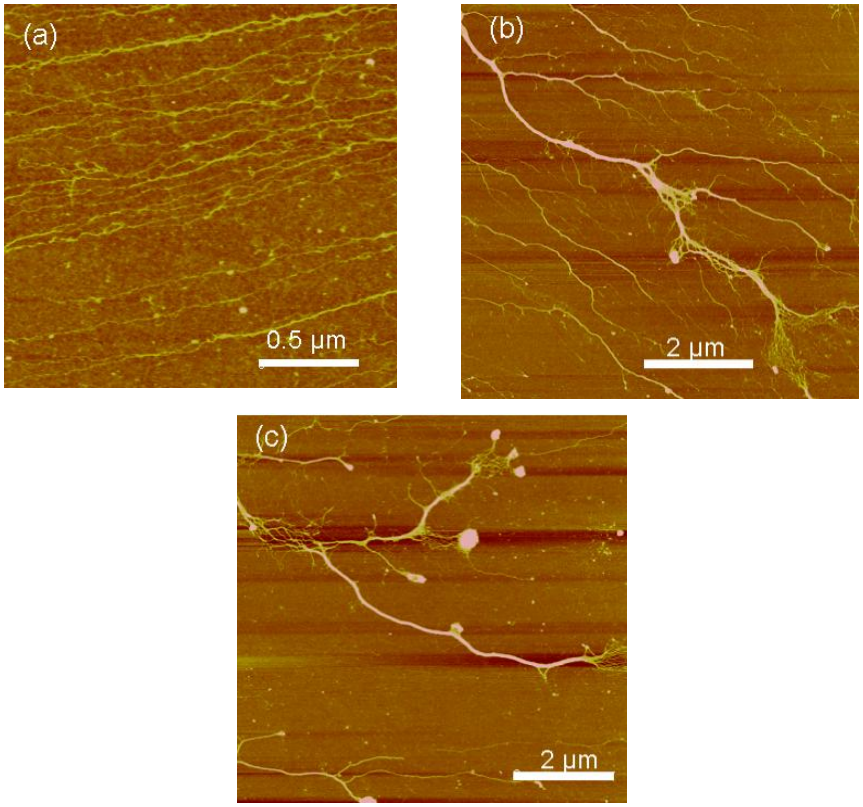

Figure 3.3: AFM images of PPy–DNA nanowires and nanoropes on a SiO_2/ Si surface. All images were taken in tapping mode and the data scale corresponds to a height range of 8 nm. a) Nanowires observed 3 h after preparation. The scale bar is 0.5 µm; b) and c) two representative images of 'nanorope' samples observed after standing for 24 h. The scale bar is 2 µm [55]

AFM images shown in Figure 3.3 (a) reveal a mixture of bare DNA molecules (height 0.5nm) and PPy–DNA nanowires (height 2nm) prepared at short reaction times (3h). The individual nanowire strands have uniform polymer coverage and there are few polymer deposits, which are not templated on the DNA; these observations support the idea that PPy chains formed during chemical oxidation are strongly bound to DNA molecules.

The thickness of the nanowires increased with time. The thin nanowires observed in Figure 3.3(a) undergo an agglomeration or assembly process, which is clearly evident in Figure 3.3(b) and (c) after a reaction time of 24h. This process cannot be simply a continual, slow polymerization of Py, because the oxidant, $FeCl_3$, supply is limited, and because the AFM images show that the thicker nanowires are entangled bundles as can be seen in Figure 3.3 (b) and (c). The bundles often show only a small variation in diameter along their length, but near their ends, they have a tendency to unravel and the individual PPy–DNA strands can be directly observed. These strands are too thick

to be single DNA molecules. Because of the resemblance of their ends to the frayed end of a rope, these structures are commonly referred to as nanoropes. In this work, it is proposed that the driving force for this process is similar to the condensation of DNA by multivalent cations [56] and cationic polymers [57, 58], although the structures formed by PPy–DNA appear to be rather different owing to the stiffness of PPy. Some similar bundles have been reported in the Zn^{2+}/ DNA system known as M-DNA [59].

The agglomeration process is gradual and continues for days, generating even thicker ropes. The bundle presented here is anchored in a very dense PPy–DNA network, resembling a net at the bottom of Figure 3.4. The end anchored to the net is thicker (12nm) than the opposite end (7.5nm), where the individual nanowires comprising the rope can be clearly seen; Figure 3.4, especially, has the appearance of a frayed shoe lace.

A 3:1 mole ratio of Py/oxidant was used with the expectation that the polymerization reaction will stop when the ferric ion in solution is depleted. However, the nanowires formed at short times can assemble non-covalently because of the compensation of the charge on the phosphate backbone of DNA [60]. A close examination of the end of the bundle presented in Figure 3.4 shows that individual nanowires have a thickness similar to that obtained for the nanowires formed after a short reaction time (1–2 nm). Data for the evolution of the nanowires and ropes are summarised in Table 3.1.

The mean thickness (AFM height) includes a small fraction of bare DNA strands (apparent thickness 0.3–0.5 nm), some individual nanowires (1–3nm) and, at longer times, some nanoropes (up to 18 nm after 2 days and 70 nm after 1 month). The presence of nanoropes in this data shows-up most clearly in the range of thicknesses measured (min–max) rather than the mean thickness, because the sample always includes some individual nanowires and a few bare DNA molecules.

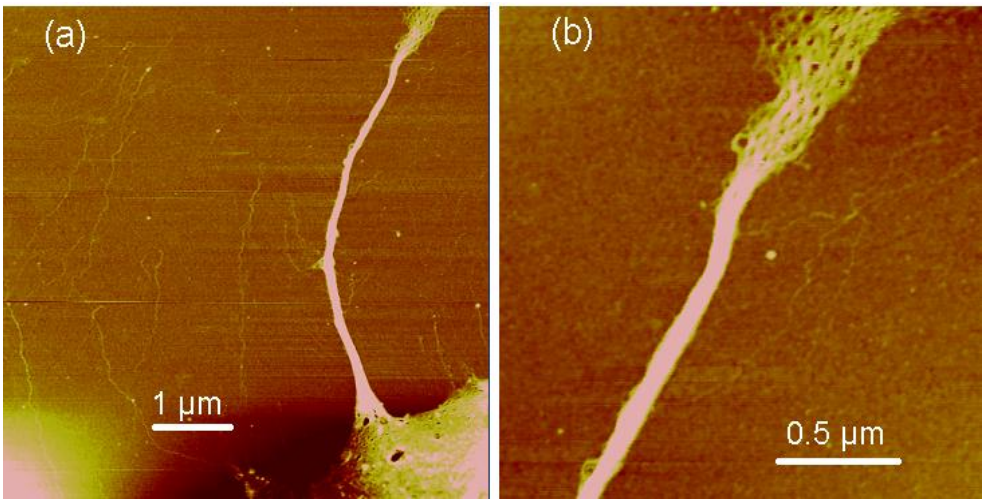

Figure 3.4. AFM images of PPy–DNA nanoropes (7.2 nm diameter) on a SiO_2/Si surface. This sample was left to assemble for 48 h before deposition on the surface for imaging. The 'frayed ends' in these examples confirm the rope-like nature of these structures. All images were taken in tapping mode. a) Scale bar 1 µm. b) Scale bar 500 nm. Data scale 8 nm in both cases [55]

Table 3.1: Mean thickness and range of thickness of nanowire and nanorope samples as a function of reaction time. The thickness measurements were estimated as the height observed in AFM image.

Time (h)	Mean thickness± standard deviation (nm)	Thickness (AFM height) range (nm)
3	0.93 ± 0.43	0.3–2.3
24	2.5 ± 1.9	0.3–6.9
48	3.0 ± 3.8	0.3–17.7
144	5.5 ± 6.7	0.3–30.0
672	9.7 ± 14	0.9–70.0

The assembly process appears very slow compared to, e.g. DNA condensation by multivalent ions, because only the presence of significant numbers of nanoropes after 24h is detected. The solutions were allowed to stand for periods of up to 1 month and observed that the nanoropes are still increasing in diameter during this time, as shown in Table 3.1. This data also strongly suggest that the reaction does not reach equilibrium after the longest times studied in this work, and the assembly of these structures are effectively irreversible at room temperature on normal experimental timescales.

AFM image of a PPy–DNA nanorope is shown in Figure 3.5(a), observed after 6 days from preparation, while Figure 3.5(b) shows nanowires 1 month after preparation. The

scale bars are 500 nm and the grayscale corresponds to a height of 12 nm in both cases. When the solution of nanoropes is allowed to stand for very long periods, up to 1 month, their width can increase up to 150–200 nm (Figure 3.5(b)) and in very few cases structures with apparent heights of 70 nm were observed. It should also be noted that the structures formed after 1 month are much less regular and less smooth than those present after a few days; the example in Figure 3.5(b) shows a thick main trunk with many thinner branches.

Additional AFM investigations of the structure of the nanoropes were possible by imaging the defects rather than the smooth sections, i.e. the frayed ends and similar structures sometimes observed in the middle of a nanorope.

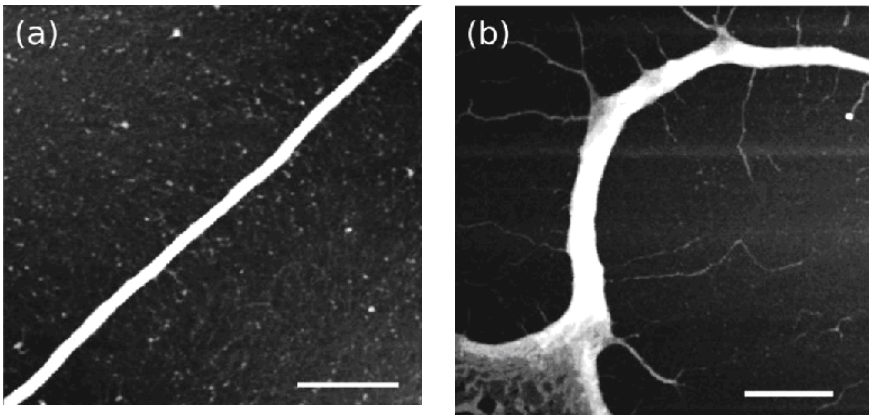

Figure 3.5. a) Tapping mode AFM image of a PPy–DNA nanorope, observed 6 days after preparation; the substrate is a SiO_2/Si surface; b) 1 month after preparation. The scale bars are 500 nm and the grayscale corresponds to a height of 12 nm in both cases[55]

In order to template conductive polymers on DNA by chemical oxidation of the monomer, it is necessary for the monomer and DNA to be soluble in a common solvent and that the monomer can be oxidised at sufficiently low potentials to minimise side reactions. These nanoropes all show regions where their morphology is rather smooth and their diameter is relatively constant. Other regions, analogous to those seen in Figure 3.4 with frayed ends, are also observed.

Examination of the frayed ends in AFM images, where individual polymer/DNA strands are visible, suggests that the assembly process involves the braiding of individual strands, where the term strand denotes the 1–3 nm thick nanowires and not necessarily single molecules. There is some regularity in the process, which can also be detected in the line section taken along an apparently smooth portion of a rope away

from the frayed end. It is proposed that the regular undulations seen in these line sections are the result of an assembly process in which several strands are simply twisted together to form a simple rope structure. The regular undulations are therefore a reflection of the regularity of the twisting. On their own, the line sections cannot establish that the ropes are formed solely by twisting strands together without some more complex braiding. However, this hypothesis also provides a natural explanation for the 'unravelling' that can be observed in the middle of some nanoropes.

The AFM images are generally not able to resolve the question of whether the braiding of the strands in any particular example is trivial or not, because not all the crossings can be observed. However, Figure 3.6 shows one example of a PPy–DNA sample where the braiding is certainly more complex than a simple twisting of the strands about each other. In summary, the assembly process proceeds by the braiding of polymer/DNA strands to form ropes; both trivial and non-trivial braiding is observed.

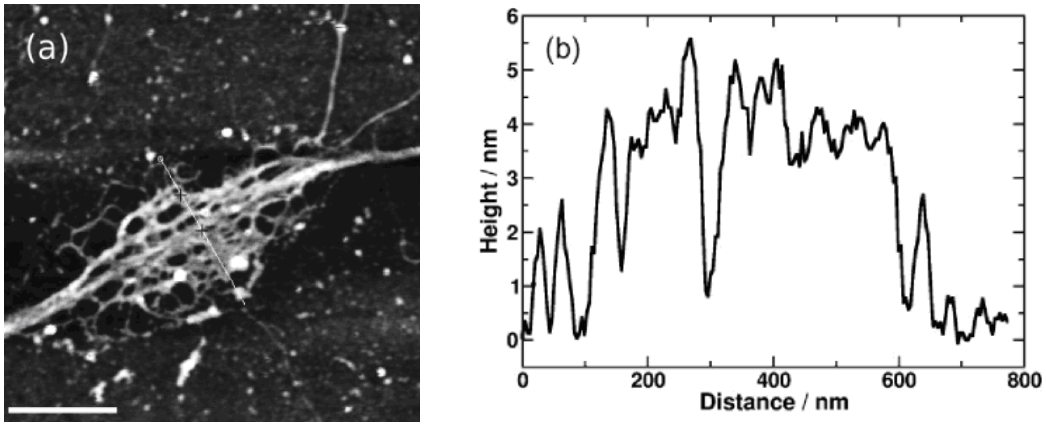

Figure 3.6. a) AFM image of two interconnected PPy–DNA nanowires and its profile cross-section (b) [55]

In order to align single molecules, nanowires or nanoropes between microfabricated Au electrodes, it is clearly desirable to have a low density of nanowires/nanoropes on the surface. Nanowires and nanoropes of PPy–DNA combed by dragging a droplet of solution across the surface: the fluid flow causes alignment in the direction of movement as long as the adhesion to the surface is low. The optimum contact angle of the surface to produce single nanowires/nanoropes spanning contact electrodes was found before in the range of 65–70° [55]. I have measured the contact angle of different substrate surfaces used and the data obtained confirm previously reported values, and fall in the same range with ± 5° error. In general, a silanization time of 20

minutes is employed in order to fabricate devices consisting of a single nanorope stretched between two Au microelectrodes. The procedure is also facilitated by embedding the Au into the SiO_2 layer so that there is a minimal height difference between the Au and the oxide.

3.6.2 Electrostatic force microscopy measurements

Since C-AFM uses contact mode and is best applied to dense networks of nanoropes (see below), EFM was also used to provide independent observations of the conduction of single nanoropes.

In the qualitative analysis, the electrostatic force is negligible compared to the short range forces in the first pass, but that the electrostatic force dominates in the second pass [61]. As shown by previous workers [46], negative phase shifts (with respect to the background) are only observed when imaging 1D structures that are conductive. As discussed before in chapter 2, section 2.10, equation (2.12) represents the phase shift, which proportional to the second derivative of the tip/surface capacitance with respect to the lift height. The capacitance is the series combination of the tip/nanorope and nanorope/surface capacitors. From equations (2.13), (2.14) and (2.15), the phase shift for an insulating object estimated using a model geometry in which the nanorope is represented by the area of a thin dielectric strip directly under the tip, itself modelled as a disc of radius R,

$$\tan(\Phi - \Phi_0) = \frac{Q V_{tip}^2}{2k} \varepsilon_o \pi R_{tip}^2 \left(\frac{1}{(h + t/\varepsilon_{ox})^3} - \frac{1}{(h + t/\varepsilon_{ox} + D/\varepsilon_{nw})^3} \right) \quad (3.1)$$

where Q is the quality factor, k the cantilever spring constant, t_{ox} the oxide thickness and D is the diameter of the nanorope. The first term is the background contribution due to the tip/oxide/Si capacitance and the second term is due to the tip/ nanorope/Si capacitance. Whilst equation 3.1 is based on an approximate geometry, it clearly shows that the phase shift is positive for any finite value of the dielectric constant of the nanorope. A negative phase shift cannot occur solely as a result of the nanorope polarisability. However, when the nanorope is conductive, the charge stored on the PPy-DNA nanorope/Si capacitor can be spread along the whole length of the nanorope, l. In effect, the second term in Equation (3.1) becomes much larger, because

the capacitance is determined by ℓ instead of R_{tip}. Equation (3.1) also exhibits a parabolic dependence of the tangent of the phase shift on the applied DC voltage. This contrasts with the linear dependence of the phase shift on potential that arises from the electrostatic force caused by trapped charges.

In this work, a method in a qualitative fashion to demonstrate the conductive nature of fabricated nanoropes was used. EFM provides a complementary way to image conductance in a convenient contactless imaging experiment where the artefacts produced by the movement of the nanoropes/wires by the tip in the contact mode C-AFM do not occur.

In EFM imaging (Figure 3.7), the tip was lifted a height of 70 nm and a DC bias was applied to the sample with the tip grounded. At 500 mV bias, no EFM phase image appeared, indicating a very weak electric field gradient. On gradually increasing the bias to 3500 mV, an EFM image of the PPy–DNA was recorded (Figure 3.7b); the image is somewhat diffuse compared to the tapping mode (height) image, as expected and shown in Figure 3.8. The images also became diffuse, and weaker, as the lift height increased. Beyond a lift height of about 120 nm, the phase shift became too small to measure. At a higher bias (5500 mV), the image contrast increased and the variation of phase along the PPy– DNA due to changes in dimension and conductance is clear (Figure 3.7c). These images also demonstrate that the other features (non-templated PPy) in Figure 3.7 (a) do not contribute to the conduction between the electrodes. The positive contrast (light area) in Figure 3.7 (a) suggests that some insulating material or static charges are present, probably a result of the combing process. Figure 3.9 presents phase shift versus bias for two similar nanoropes. The variation of phase shift with voltage is clearly parabolic, though there is a slight asymmetry in the curves, which may be a result of a minor contribution from trapped charges.

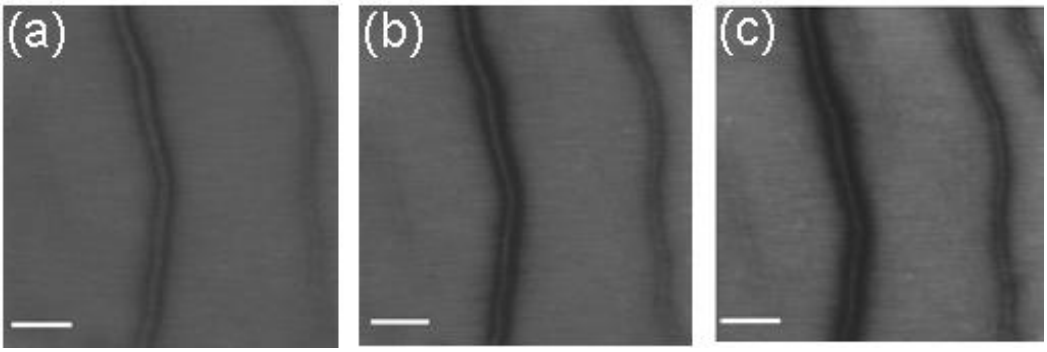

Figure 3.7. EFM phase images of a nanorope at different tip/sample biases. The images show the phase angle of the tip oscillation at the following tip/sample potentials: -3 V(a); -4 V (b); -5 V (c). The lift height was 70 nm, the scale bars are 400 nm and the grayscale corresponds to a phase angle of 3° [55]

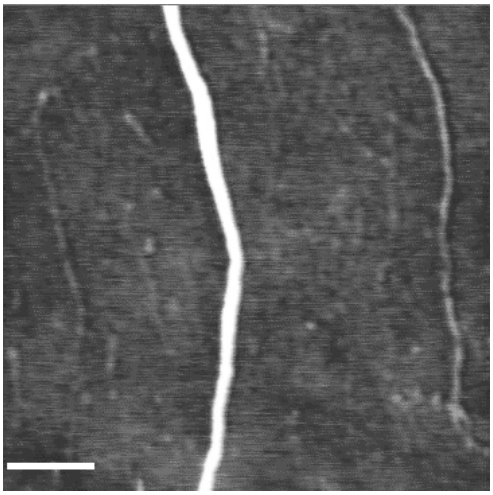

Figure 3.8. Tapping mode™ AFM image of PPy-DNA nanorope and nanowires aligned on a Si/SiO_2 substrate. The scale bar is 400 nm and the grayscale corresponds to a height of 10 nm [55]

Figure 3.8 shows a tapping mode image of a nanorope, and illustrates that these can be rather smooth in appearance, i.e., there is no evidence of this particular rope unravelling. The mean diameter, estimated from the AFM height, is 8.1 nm in the image shown. The variation in the cross-section of the rope over the length shown is also small: the relative standard deviation of the diameter over the length shown is about 10%. Quantitative data for the EFM phase angle is given in Figure 3.9.

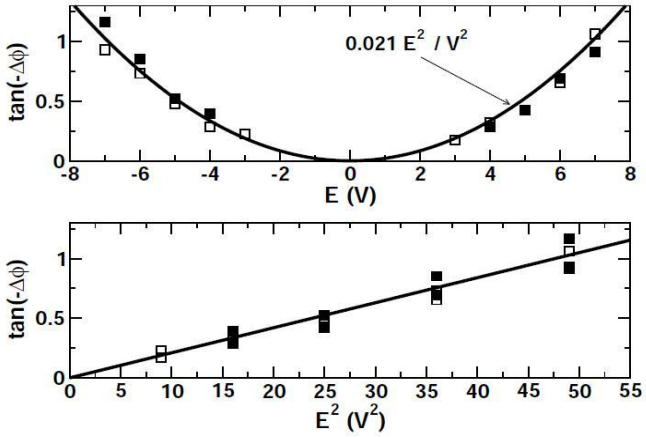

Figure 3.9. EFM data as a function of tip/sample bias for two nanoropes of AFM height 6.8 and 8 nm. The lift height was 60 nm. Tangent of phase angle versus tip/sample bias, E above and E^2 below. The solid lines are the fits to the parabolic dependence on tip/sample bias expected when the origin of the phase shift is purely due to the conductive nature of a 1D object being imaged [55]

EFM images of 1D objects can be influenced by electrostatic forces from trapped charge, Van der Waal's forces or capacitive effects characteristic of extended conducting objects. These can be distinguished by their characteristic dependence of the EFM phase angle on the applied tip/sample bias. The dispersion interactions or other non-electrostatic forces show no potential dependence, whereas the trapped charge effect gives rise to a linear dependence of tangent of phase angle on bias voltage and the conductance effect to a parabolic dependence. It is clear from the symmetric, parabolic curves of Figure 3.9 that the conductance effect dominates in the images. This allowed using EFM-phase imaging to map the current path along these nanoropes. Together, Figure 3.9 and Figure 3.11 confirm that the conduction pathway, which produces the I–V characteristics in Figure 3.11 (a) lies through the nanoropes.

3.6.3 Conductance of non-uniform PPy–DNA nanowires

Topographical characteristics of the nanorope and the electrodes that are slightly recessed into the oxide of PPy–DNA nanorope (10-15 nm diameters) are shown in Figure 3.10. It shows that the end of the rope adheres to the Au electrodes (the dark areas to the left and right of the image). This nanorope does not have a uniform diameter along its length, being thicker in the middle; because there is some non-templated PPy present, it also illustrates the utility of EFM in observing the conduction path between the electrodes. Figure 3.10 (b) and (c) are the EFM phase images acquired simultaneously with the conductive objects (nanoropes and Au electrodes),

which produce a negative phase shift compared to the background over the SiO_2. EFM result confirmed the direct I–V measurements done on this nanorope. I–V curves of the nanorope before and after cutting using the AFM tip are shown in Figure 3.11(a). The original background current of the two microelectrodes, measured immediately after chip fabrication is also presented. I–V curves are noticeably nonlinear; such curves are found in systems where the system shows a significant gap in the energy spectrum, or the electric field is large on a molecular scale. However, the asymmetry of the curves, in a Au-wire-Au system suggests instead that the resistance of the polymer/Au contact is important, and that the two interfaces are not equivalent in any particular device.

The nanoropes proved to be rather robust and resistant to damage by the AFM tip, except under very high loads in contact mode AFM. Nevertheless, at sufficiently high normal forces (~0.13 mN) it was possible to cut the nanoropes. After cutting the nanorope, the conductance dropped. Figure 3.10(a) shows that it is certainly carrying the current. However, some residual conduction is still present, which is probably due to debris from the cutting procedure Figure 3.10(b). For this reason, conductive AFM and EFM phase imaging was used to confirm that the conduction observed in Figure 3.10 is via the PPy–DNA and not via leakage paths across the surface due to humidity, ionic impurities or through defects in the oxide. It is also worth noting that heat treatment of such devices to drive off water did not remove the conductivity, as would occur if ionic impurities and humidity were important in the conduction mechanism.

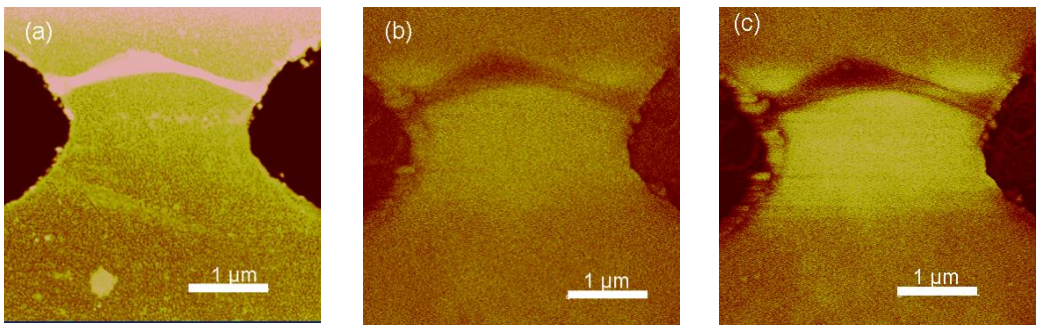

Figure 3.10. AFM and EFM images of PPy–DNA nanorope on a SiO_2/Si surface with two Au microelectrodes for I–V characterization. a) Tapping mode AFM, scale bar 1 µm and height 25 nm. b) EFM phase image of the nanorope in a) at a bias of 3.5 V, lift height 70 nm, scale bar 1 µm and the grayscale corresponds to a phase angle of 3°. c) EFM phase image of the nanorope in a) at a bias of 5.5 V, lift height 70 nm, scale bar 1 µm and the grayscale corresponds to a phase angle of 3°[55]

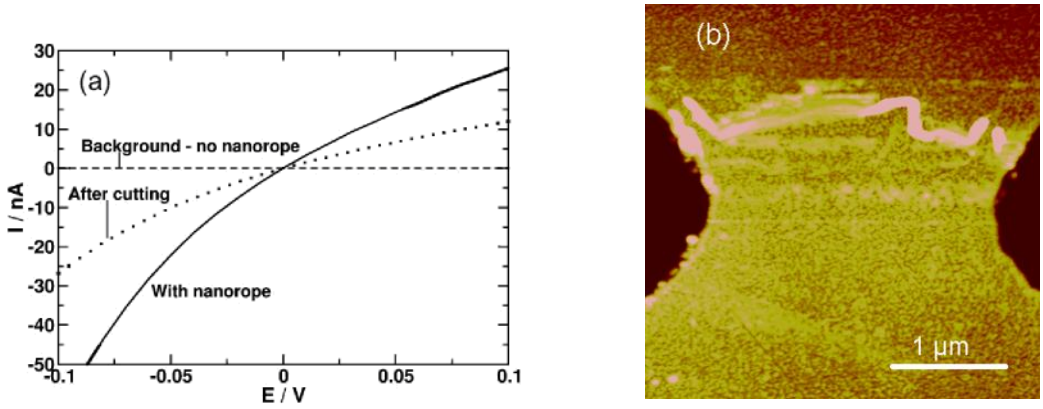

Figure 3.11. a) I–V characteristics of the nanorope crossing the two Au microelectrodes. b) AFM image of the nanorope after cutting., with scale bar 1µm and grayscale 20 nm[55]

In the conductive AFM experiment, it was observed that networks of nanoropes could be imaged reliably, whereas single ropes were not. That is because sinlge nanowire is not strongly adhered to the substrate surface and can be easily affected by the movement of the cantilever's tip, while in case of networks, there is a stronger interfacial adhesion between the nanoropes and the substrate surface. In this experiment, therefore, multiple nanoropes are deposited on a hydrophobic, oxidised silicon chip to form a rather dense network. C-AFM provides a direct means to establish that the nanoropes are conductive. However, because C-AFM measurements employ contact mode to maximise the time spent by the tip in electrical contact with the nanoropes, there is a greater tendency for the tip to disturb the nanoropes and the images show evidence of some artefacts due to movement of the nanoropes during imaging. A single contact to this network is made by applying a drop of In/Ga eutectic to one corner of the chip; the imaged area is about 1 mm from this contact.

Figure 3.12 shows typical data for PPy–DNA nanoropes on non-silanised Si/SiO_2 surfaces; the usual contact mode height image (Figure 3.12a) shows the presence of about 7–8 nanoropes μm^{-2}. The deflection error, which is the difference between the measured deflection and the setpoint, was also recorded and provides a slightly clearer image (Figure 3.12 b), because it is less affected by slow events related to the movement of the nanowires. The current image, which was acquired simultaneously with the tip held at a potential of 9 V with respect to the In/Ga contact, shows clearly that high currents are associated with the image features in Figure 3.12(a) and (b) due to nanoropes and, importantly, the current over the bare portions of the oxide is below the

detection limit of the current amplifier (~10 pA). The nanoropes are lying on a 200 nm-thick SiO_2 film on a 1 x 1 cm Si chip. There is a remote In/Ga eutectic contact at one corner of the chip and the current flows through the network of nanoropes to this remote contact. No measurable current was observed in the regions where no ropes are present (dark regions, Figure 3.12c), which demonstrates that there is no current leakage through the oxide and the current path is via the nanoropes. These images demonstrate that the current path from the tip to the In/Ga contact is through the nanoropes lying on the surface and that charge does not leak across the oxide and reach the contact by transport through the Si substrate. In Figure 3.12 (b) deflection error image, it can be observed that the structure looks sharper and brighter and clearly represents pieces of a nanowires-like structure. Nanowires in the tapping image shown in Figure 3.12 (a) are not very clear, that's because nanowires are not strongly adhered to the substrate surface and disturbed by the movement of the cantileaver's tip. On other hand, the current image seen in Figure 3.12 (c) acquired at the same time as the previous two images show current flowing between the tip and the contact. It can be observed that when the tip is contacting areas with very few nanowires there is no current (shown as dark areas), whereas areas showing particular nanowires, which are visible in tapping and deflection errors images, show white features, that represent actual nanowire currying a current.

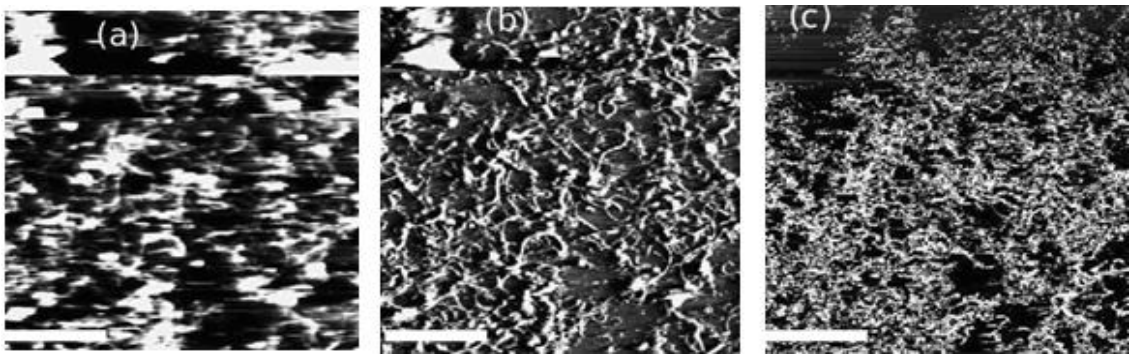

Figure 3.12. C-AFM measurements of PPy–DNA nanoropes and nanowires aligned on a 220 nm SiO_2/Si substrate. a) Contact mode image the grayscale corresponds to a height of 13 nm; b) Deflection error image (the grayscale corresponds to a height of 10 nm) and c) C-AFM current image (the grayscale corresponds to a current of 100 nA). The area imaged was 7 μm^2. The grayscale is white = +100 nA and black corresponds to 0 nA. Scale bars 2 μm.

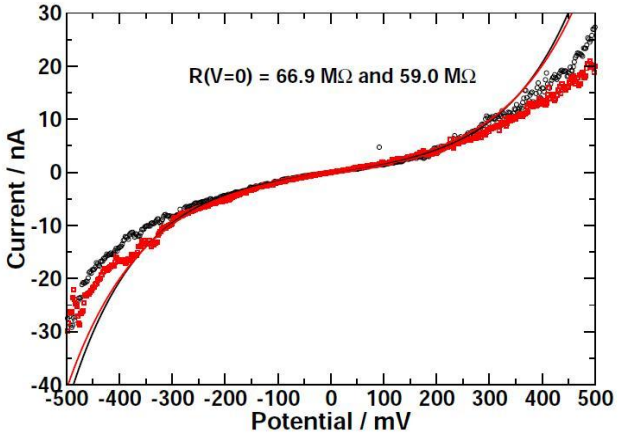

Figure 3.13. Typical single point I-V curves reordered during the c-AFM experiment of a nanorope with about 20 nm diameter and about 1 μm relative length

Single points I–V curves are given in Figure 3.13. The tip is held stationary at a pre-defined point on the image corresponding to a conductive object and the tip/sample voltage is applied. The smooth curves are weighted least-squares fits to equation 3.2 over a range of +/- 0.1 V. These fits were used solely to extract the resistance at zero bias. This function found consistence with data and mach equation (2.17) discussed in chapter 2, section 2.9. This equation can be reduced to the form y=-ax+c as follows;

$$I = I_0\left[e^{\alpha x} - e^{-(1-\alpha)x}\right] \qquad (3.2)$$

Where $x = FV/RT$. For $x \ll 1$, $I = I_0 FV/RT = G_0 V$, where $G_0 = I_0 F/RT$ is the zero bias conductance. This is the linear region around zero bias, which represents the case of fixed anions. This provides evidence that the shape of the curve shown in Figure 3.13 very much like the curve in chapter 2, Figure 2.26 (f) and fit equation (3.2).

3.6.4 Temperature dependence of conductivity of PPy-DNA Nanoropes

Due to their potential applications in nanometre-scale electronics, conductive polymers have received considerable attention in recent years. Among these polymers, great interest has been devoted to polypyrrole (PPy) to determine its electrical properties. PPy has been prepared as thin-films [62-64], nanotubes [9, 65], nanowires [66] and as a bulk solid [67]. However, PPy conductivity has been reported to vary according to its structure and the preparation technique employed. For example, the conductivity of doped PPy as a 600 nm thick film prepared by the in situ vapour-phase polymerization

method was found to be about 6×10^2 S cm^{-1} depending on deposition time [63]. The resistivity of PPy nanotubes (120 nm diameter) was found by Park, J.G and *et al* to be in the range of 1 Ω cm measured by scanning probe microscopy [65]. Bocharova *et al* measured the conductivity of a single PPy nanowire (50-60 nm in diameter) grown onto a device comprising Au microelectrodes (1 μm apart), and found it to be about 1-3 S cm^{-1} [66].

As a consequence of the variability of conductivities for different PPy samples and preparation procedures, the conduction mechanism, as deduced from temperature-dependent conduction data, has been reported to follow different models. For example, Barde and co-workers suggested that temperature-dependent of conductivity of PPy thin films chemically synthesized using $FeCl_3$ as an oxidant obey the Vogler-Tamman-Fulcher (VTF) model ($\sigma = A/T^{1/2}\, e^{(-B/k(T-T_0))}$) with crossover to the Arrhenius model between 308 to 383 K, where T is the absolute temperature; A, B and T_0 are the fitting constants, while 'k' is Boltzmann constant. Here A is the pre-exponential factor related to the number of charge carriers and B is the pseudo activation energy related to activation energy of the ion transport [68]. Other workers found that the temperature dependence of the conductivity shows also a clear crossover from one model to another. For example, the transition to Arrhenius behaviour above a critical temperature was observed in polypyrrole thin films by Bof and Heinzel [69]. Gence, *et al* studied the effect of temperature on single PPy nanowire of different diameters spanning two gold electrodes in the range between 4 and 300K; over this range of temperatures, it was found that its behaviour follows the 3D-Mott variable-range-hopping model for samples above 40 nm in diameters and nonmetallic behaviour for all investigated samples [70]. Shen, *et al* investigated the electrical conductivity of a single PPy nanowire (38.4 S cm^{-1}) prepared electrochemically upon an alumina template and measured using the four-terminal technique in the range between 77-300 K [71]. In their work, the resistance of the PPy nanowire was found to increase with decreasing temperature, following Mott variable-range-hopping model. Moreover, temperature dependence studies on thin film of PPy fibers by Spatz, *et al* suggested that the resistivity crossover from 2D to 3D Mott variable range hopping model over range of temperatures depends on the thickness of the film [72]. On other hand, a study by Sandra C. *et al*, showed that the Arrhenius conduction can be used successfully to describe the charge transport in long conducting PPy nanowires [73].

In this work, PPy-DNA nanowire aligned across Au electrodes was placed in a CMS cascade Microtech summit 11000 series probe station with DCM positioner to study its conductance as a function of temperature. A high performance DC probe holder with probe tips of 9 μm radius was used to connect the nanowire through the pad electrodes to the external microcircuits. A Leica S8 stereo zoom microscope was used to observe the probe tips and pad electrode, to ensure that the tips or the Au pads were not damaged by applying excessive force. Temperature variation was achieved using a thermal chuck system (Model ETC-200 L, ESPEC, Japan) equipped with refrigerator unit. The current-voltage sweep measurements were carried out on PPy-DNA nanoropes using a Hewlett Packard semiconductor device analyzer (HP/Agilent B1500A) controlled by Aligent EasyEXPERT software. The sample was placed on a vibration isolation table inside a chamber under nitrogen gas.

The current and voltage-drop across the nanowire was measured over a temperature range from 213 to 345 K. All measurements were taken in the dark. The conductivity of single PPy-DNA nanowire at room temperature is calculated using the relationship, equation 2.16, chapter 2. Where l is the length of the PPy-DNA nanowire in μm, A its average cross-sectional area and R its resistance in Ohm (Ω). The length, diameter and cross-sectional area are estimated from AFM images of the nanowire. The resistance is calculated from the ohmic part at the origin of the I-V curve and the conductance, the reciprocal value of the resistance, in Siemens (S) is obtained accordingly. The decrease in the nanowire's dimensions increases its resistivity. This increase is related to the grain boundary and surface scattering. That is because more reflections at the surface by the electrons occur as the nanowire's diameter reduced. The uncertainty in the dimensions of the PPy-DNA nanowire expected to influence the value of its resistivity. For that reason, investigations of the PPy-DNA nanowire's uniformity were carried out and found to be very high (smooth nanowire). The result of the PPy-DNA nanowire's uniformity investigations can be found in section 3.6.6.

This section presents work done to study the effect of temperature on electrical conductivity of PPy-DNA nanowires and nanoropes. The conductivity of PPy nanowire templated by DNA chemically prepared using $FeCl_3$ as an oxidant at room-temperature was determined to be in the range of 4 S cm^{-1}, which is markedly higher than the previously reported value of rod-shaped PPy templated by alumina templates (3 m S cm^{-1}). This conductivity is of the same order as the conductivity of bulk PPy

powder (1.7 S cm^{-1}) prepared chemically by $FeCl_3$. In these experiments the focus was on investigating the conductivity of DNA-templated polypyrrole nanowires as a function of temperature to explore the basic conduction mechanism and demonstrate the thermal stability of the polymer nanowires. The temperature-dependent measurements were performed on a single PPy-DNA nanowire aligned between two micro-fabricated Au electrodes (8.5 μm separation) embedded in SiO_2. The unique structure of the fabricated electrodes allowed to align easily varieties of polymer nanowires, study their morphology by AFM and record their I-V curves. PPy-DNA nanowires were examined also by FTIR spectroscopy as a function of temperature.

For temperature dependent experiment, PPy-DNA nanowires were synthesized, as described in section 3.2 of this chapter in a one-pot reaction to avoid a long process, where cationic (positive charges) of polypyrrole (PPy) interact electrostatically with the anionic (negative charges) of DNA provoking the privileged growth of polymer along DNA chains. Before aligning the nanowires, the SiO_2 surfaces of the chips were treated by exposure to Me_3SiCl vapour for 25 minutes, in this case, forming a methyl-terminated monolayer on the substrate, and producing a hydrophobic surface. Then a drop of 3.5 μL of the solution was dispensed in the middle of the chip, and spun (300 rpm for 2 minutes) before applying molecular combing.

3.6.5 Alignment of PPy-DNA nanowires for temperature dependent measurements

To facilitate alignment of nanowire across electrode for I-V measurements, face-to-face four microelectrodes were fabricated (about 16 μm tip length and 2.5 μm width connected to 10 x 20 μm Au pads with a larger pads of about 0.5 mm x 1 mm) for electrical measurements. The separation between any two facing electrodes measured by AFM is about 8.5 μm. This arrangement allowed a single PPy-DNA nanowire to be connected easily to one of the face-to-face pair electrode tips and aligned across the gap between them. The large pads were used to connect the nanowire to the probe station for the I-V measurements. Details of the microfabrication process used were presented before in chapter 2.

Molecular combing discussed in section 2.7 has been adapted here to align the nanowires across the Au microelectrodes [15]. It is found that spinning a drop of the solution containing nanowires prior to applying the combing technique facilitated the

alignment of the nanowires upon the substrate surfaces. The optimum speed of rotation, in order to obtain individual nanowire alignment, was between 100 and 300 rpm. Figure 3.14(a) shows an AFM image of individual and well defined nanowires stretched upon Si substrate surface with spinning speed of 250 rpm, followed by combing. The diameters of aligned nanowires, shown in Figure 3.14, range from about 3 to 13 nm. Figure 3.14 (b) shows a single nanowire aligned across two electrodes after being spun at 250 rpm. It appears uniform and homogenous. Examples of nanowires spun at higher speed (>500 rpm) before combing are shown in Figure 3.15(a) and (b). Typically, 3.5 µL drop of solution of PPy-DNA nanowires was dispensed on the area containing the microelectrodes and spun for 30 seconds before removing the remaining solution using a micropipette and filter paper.

The Au electrodes and the surrounding oxide were treated with chlorotrimethylsilane (Me_3SiCl) for 25 minutes producing an appropriate hydrophobic surface prior to stretching and aligning the DNA-PPy nanowires. A very thin self-assembled monolayer of silane is formed on the surface when it reacts with the hydroxyl-terminated SiO_2.

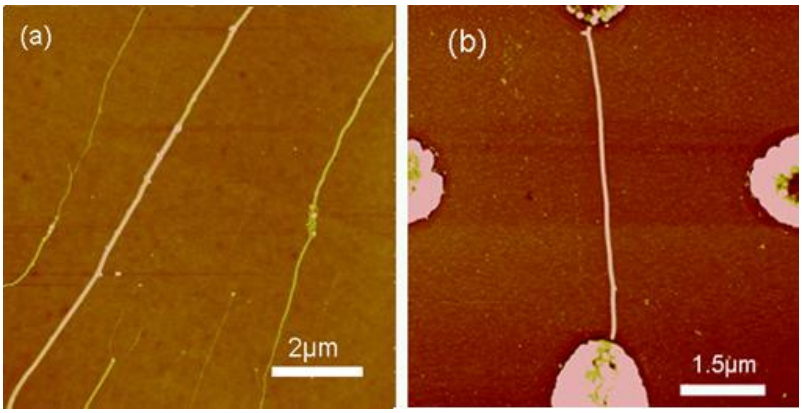

Figure 3.14: a) Example of PPy-DNA nanowires, with diameter ranges from 3-13 nm, aligned on SiO_2. Scale bar 2 (µm) and height scale 25 nm. b) AFM tapping Mode™ image of single PPy-DNA nanowire aligned across two Au electrodes. Scale bar 1.5 µm and height scale 30 nm. Length of the nanowire ℓ =8.5 µm and average diameter D=23.9nm[55]. Spinning speed 250 rpm

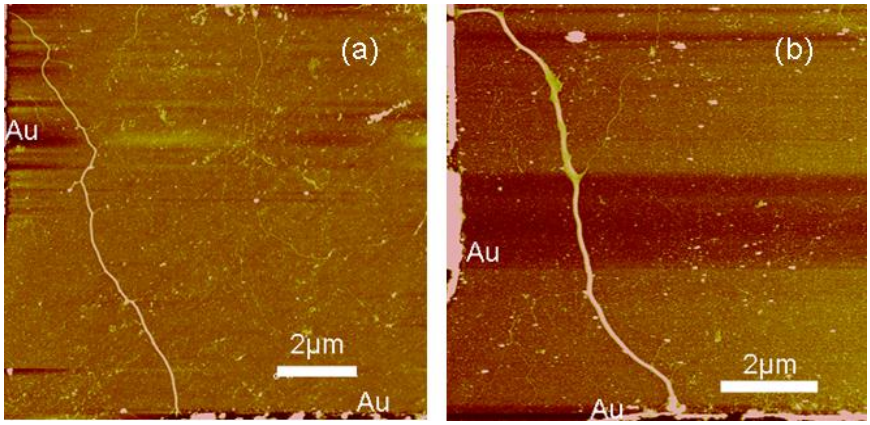

Figure 3.15: a) AFM tapping Mode™ image of single PPy-DNA nanowire aligned across two Au electrodes with spinning speed of 500 rpm. Length of the nanowire about 12 μm and variable diameter ranges from nm. b) AFM tapping Mode™ image of single PPy-DNA nanowire aligned across two Au electrodes. Scale bar 2 μm and height scale 15 nm. Length of the nanowire about 11 μm and variable diameter ranges from 9-20nm.

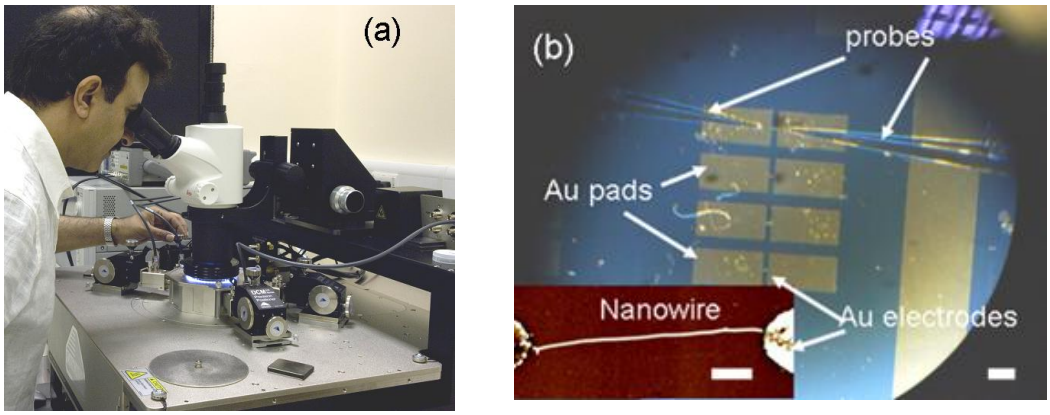

Figure 3.16: a) Probe station used in the electrical measurements and b) Au electrodes inside the probe station, scale bar 0.25 mm. Inset, PPy-DNA nanowire aligned across Au electrodes and inserted inside the chamber, scale bar 1 μm

3.6.6 Diameter uniformity of PPy-DNA nanowire

The nanowire diameter uniformity of a single PPy-DNA nanowire, shown in Figure 3.14 (b), spanning Au microelectrodes can be estimated from the formula [74]:

$$Du = |\Delta D/\ell| \qquad (3.3)$$

Where Du is the diameter uniformity of the nanowire, ΔD is the maximum diameter deviation from the diameter at the center of the nanowire (Dc) and ℓ is the length of the nanowire.

With ℓ=7.8 μm, $Dc = 23.5\ nm$ and $\Delta D = 24.8 - 23.5 = 3.44$ nm calculated between the two ends of the PPy-DNA nanowire as in Table 3.1. Du , found very small (4.4×10^{-4} nm), which indicates that the PPy-DNA nanowire has a high uniformity.

Table 3.2: The maximum diameter difference between the two ends of one PPy-DNA nanowire shown in Figure 3.14b

Nanowire's Diameter at different locations, D (nm)	Nanowire's Length, ℓ (μm)	Deviations from the central diameter (nm)
21.75, 20.06, 21.75, 21.23, 21.24, 21.13, 20.81, 20.81, 22.81, 22.52, 22.95, 24.8,	7.8	1.75, 3.44, 1.75, 2.27, 2.26, 2.37, 2.69, 2.69, 0.69, 0.98, 0.55, 1.30,

3.6.7 FTIR spectroscopy

FTIR spectroscopy was performed on the PPy-DNA nanowires in the range 600-4000 (cm^{-1}) with spectral resolution of 4 cm^{-1} using a Biorad FTS-40 Spectrometer equipped with a liquid-nitrogen-cooled MCT detector. A drop of the solution of about 3 μL was dispensed on Si(100) substrate and left to dry before spectroscopic analysis. FTIR spectra of PPy-DNA nanowires were performed at various temperatures by placing the substrate with the nanowires on its surface into the oven at a given temperature for 10 minutes before the spectra were recorded. The FTIR spectra were recorded at several temperatures between 296 and 493 K. A clean Si chip was used as FTIR background reference.

Oxidation of pyrrole in DNA-containing solutions yielded a material that contained both the cationic PPy and the anionic DNA polymers[22]. Interaction of the two polymer chains in the self-assembled nanowires were investigated. The FTIR spectra obtained indicated that the PPy-DNA sample was an intimate interaction of DNA with PPy in the hybrid polymer. FTIR spectroscopy was also exploited to determine the temperature stability of the nanowires and to assess whether the temperature-dependent conductance was due to chemical changes. This step is important to find out the maximum temperature that nanowires can handle before they decompose or physical change occurs.

Figure 3.17 shows the FTIR spectra of PPy-DNA nanowires measured from RT up to 430K. The FTIR spectra began to exhibit chemical changes (e.g. decrease in water bound absorbance at about 3300 cm^{-1}) as the temperature continued increasing up to

380K because of the evaporation of water. This suggests that the polymer nanowires remain unchanged in the range between 296 and 380K, but start to exhibit chemical change at temperatures higher than 380K due to the loss of water. FTIR spectra obtained indicate the significant chemical changes up to 380K due to the fact that PPy-DNA nanowires are dehydrated, which is consistent with the temperature-dependence of conductivity measurements of PPy-DNA nanowires that will be discussed in the next section.

A full FTIR analysis of the PPy-DNA samples was done in a previous work [22] at Chemical Nanolaboratory, Chemistry School, University of Newcastle. In that analysis, the FTIR spectra obtained for the isolated materials used in the reaction provided evidence of the formation of a supramolecular hybrid polymer containing DNA and polypyrrole.

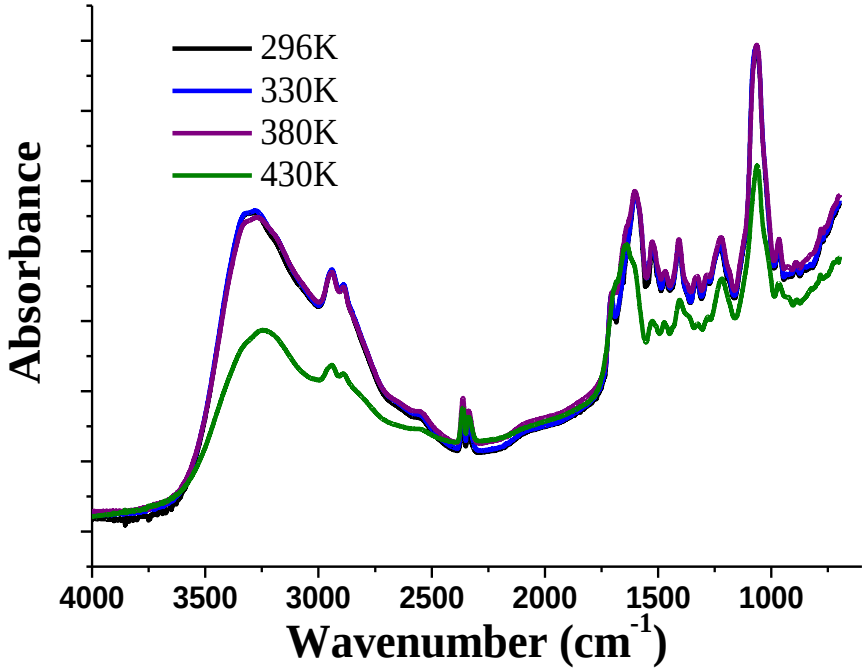

Figure 3.17: FTIR spectra of a drop of solution containing PPy-DNA nanowires recorded at different temperatures from 296 to 430 K. The FTIR spectra exhibit distinct chemical changes (decrease in water bound absorbance at about 3300 cm^{-1}) up to 380 K due to evaporation of water, which indicates removal of moisture [55]

3.6.8 I-V curves varying with temperature of PPy-DNA nanowire

The temperature dependence of I-V curves of a single PPy-DNA nanowire shown in Figure 3.14(b) have been investigated by placing the chip containing the nanowire in the probe station, where the temperature was controlled and monitored. A series of applied voltages (V) current (I) passing through the nanowire were recorded. The temperature was then raised and allowed to stabilise before the same measurements were recorded again. This process was repeated over a range of temperatures, up to 400 K. I-V curves depicted in Figure 3.18 show that the current passing through the nanowires increases with increasing temperature. The I-V data of the PPy-DNA nanowire shown was recorded in the range between -1.3V and 1.2V, and over a range of temperatures using a thermal chuck system (Model ETC-200 L, ESPEC, Japan).

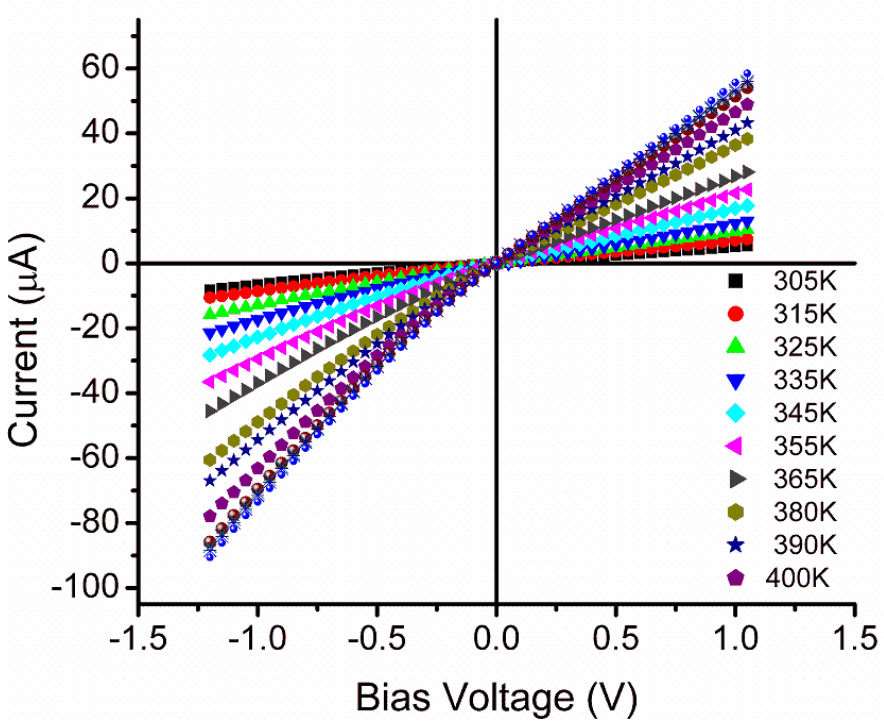

Figure 3.18: Temperature dependence of I-V curves of a single PPy-DNA nanowire aligned across two Au electrodes

As discussed before, various models have been employed to describe the temperature dependence of I-V curves of conducting PPy. Most conducting polymers show an increase in conductivity with temperature. However, the precise nature of the temperature dependence might be affected by many factors, such as the polymer structure, degree of crystallinity [75] and dimensionality [72]. The various models of

conduction mechanisms of polymers obtained as a result of the different synthetic routes used that led to different structures of polymer samples. It is worth mentioning here that the water content in polymer nanowires can also play an important role in determining the conduction process.

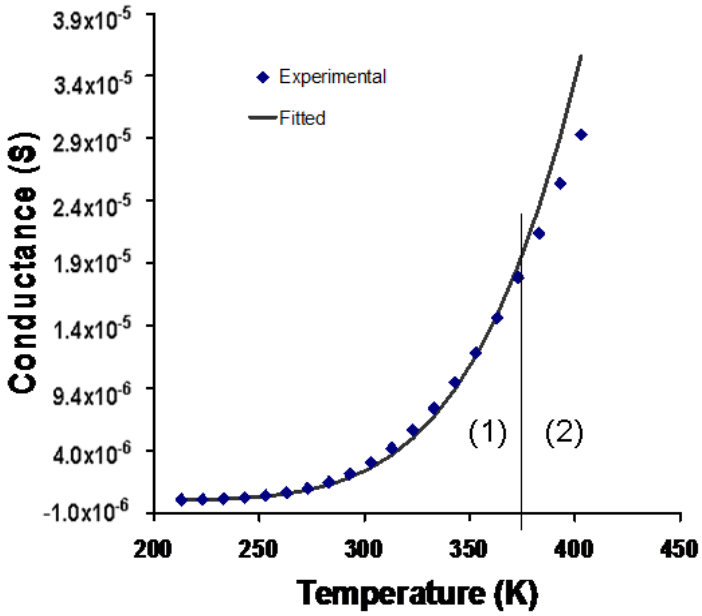

Figure 3.19: Conductance (G) of a single PPy-DNA nanowire varying with temperature. In area (1), theory and experiment agree, as the FTIR result predicts. In area (2), the FTIR result shows water loss, which led to lower nanowire conductance.

I-V curves done on PPy-DNA nanowires show some non-linearity close to the origin. A small tunnelling barrier at the Au electrode and PPy-DNA contacts could be the cause for this behavior. Yet, from the slope of the curves at 0V, the conductance for all the curves was obtained.

In general, the temperature dependence of the conductivity of conjugated polymers has typically been fitted to expressions of the form

$$G = G_0 \exp^{-(T_0/T)^{\beta}} \qquad (3.4)$$

where T_0 is the characteristic temperature and G_0 is a constant that measures the disorder in the nanowire structure, and

$$\beta = 1/(n+1) \qquad (3.5)$$

The parameter β depends on the underlying theoretical model and the dimensionality ($n=0,1,2,3$) of the system. For example, thick films of conducting PPy, prepared chemically, exhibit temperature dependence described by 3D variable range hopping, where β=1/4, while thin films follow the Efros-Shklovskii model with β=1/2 as in [76] and [77] respectively. A simple calculation extending the original variable range hopping model to 1D and 2D structures predicts β=1/2 for nanowires. However in 1D systems, the electron cannot avoid a large barrier and the conductance may be dominated by such 'breaks': Arrhenius behaviour (β =1) is then expected [78].

Figure 3.19 shows the conductance of a single PPy-DNA nanowire varying with temperature. The model in equation (3.4) fits the data accurately to 380K with fitted parameters G_0 = 0.3 S, T_0 = 4000 K and β=1, which suggests that nearest neighbour hopping is the dominant mechanism for electron transport along the prepared PPy-DNA nanowires leading to the exponential behaviour of the conductance. Hopping of carriers is responsible for the exponential increase behaviour of the conductance with increasing temperature. At temperature less than 380K, the conductance follows the model in equation 3.4, but at higher temperature (above 380K), the curve starts to deviate from this model owing to chemical changes as shown by the loss of water bands in the FTIR spectra (Figure 3.17).

Although good temperature-dependent conductance measurements were obtained, and the same general features observed between samples, there are substantial sample-to-sample variations in the conductivity. Using the C-AFM technique and the topography of one of the PPy-DNA nanowires shown in Figure 3.12 (length of 1 μm and a diameter of 20 nm) gives an approximate room-temperature conductivity of $2x10^{-3}$ Scm^{-1}. However, using the two-terminal technique, the room temperature conductivity for the PPy-DNA nanowire (l=8.5 μm and average diameter D=23.9 nm) was calculated as 57.4 Scm^{-1} from the slope of the I-V curve at 0 V. This illustrates the difficulty in obtaining clear-cut values of conductivity because of sample-to-sample variations, and possibly, variations in contact resistance.

Figure 3.19 shows also that PPy-DNA nanowires exhibit a significant increase in electrical conductance with increasing temperature. In the region less than 380 K (area 1), the data agrees with the theory, which in turn agrees with the FTIR result, (FTIR result shows water loss above 380 K). Whereas in area 2, above 380 K, the conductance measured experimentally is less than that measured theoretically, which

might be due to water loss at higher temperatures. Moreover, Figure 3.20 shows the corresponding Arrhenius plot for conductance of single nanowire shown in Figure 3.14 (b). This figure is a plot of log G versus T^{-1} on which the curve is linear over range of temperatures. It shows a straight line, describing the conductance of the form shown in equation 3.4, with $\beta=1$ characteristic of 1-dimensional object such as a nanowire. This behaviour can be understood on the basis of a simple nearest-neighbour hopping model for the reasons mentioned above is quite expected.

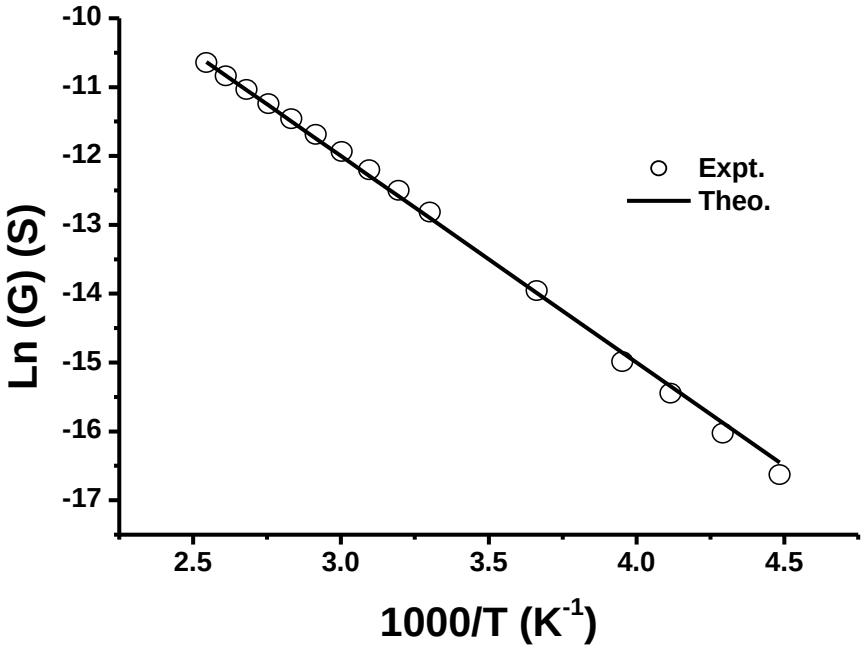

Figure 3.20: Arrhenius plot for the zero-bias conductance of single PPy-DNA nanowire

3.6.9 Stability of PPy-DNA nanowires with temperature

To study their stability with temperature, the PPy-DNA nanowires were heated then cooled down using a probe station with about 1K per minute heating/cooling rate.

During the heating and cooling of the nanowire, I-V curves were recorded. All I-V curves exhibit an increase in conductance with increasing temperature. The conductance measured from the ohmic part of each I-V curve is plotted against temperature as shown in Figure 3.21. The blue curve in the figure represents the heating up process, while the red curve represents the cooling down process. The cooling curve exhibits very small hysteresis.

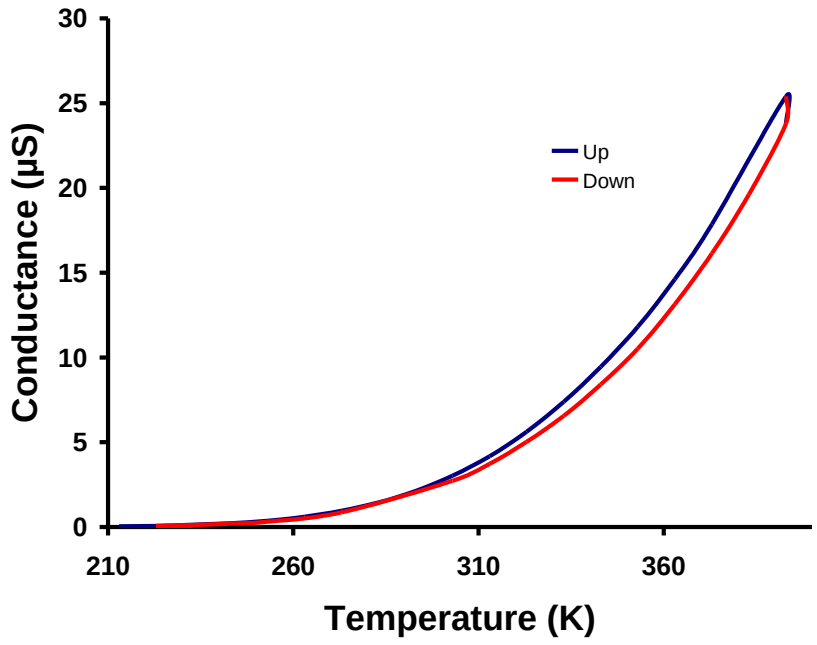

Figure 3.21: Temperature dependence of conductance of the PPy-DNA nanowire recorded for one heating and cooling cycle between RT and 380 K with heating/cooling rate of about 1K/minute

3.7 Conclusions

PPy nanowires formed by polymerization of Py on a DNA template self-assemble into rope-like structures. PPy-DNA nanowires were chemically synthesized using $FeCl_3$ as an oxidant at room temperature. These 'nanoropes' may be quite smooth (diameters 5–30 nm) or may show frayed ends where individual strands are visible.

The PPy-DNA nanowires were examined by FTIR spectroscopy as a function of temperature. FTIR spectra of the polymer nanowires obtained indicate significant chemical changes up to 380 K, due to evaporation of water. A design of microfabricated Au electrodes embedded in SiO_2 was used to facilitate the two terminal I-V measurements. Electrical conduction was studied at room temperature, as well as a function of temperature. At room temperature, the conductivity of PPy-DNA nanowire of 8.5 µm length and 23.9 nm diameter obtained from the two terminal I-V measurements is 57.4 S cm^{-1}, compared to $2x10^{-3}$ S cm^{-1} obtained for 1 µm length and 20 nm diameter nanowire using conductive AFM technique. This difference in conductivity obtained by the two methods may be due to the high contact resistance between the cantilever's tip and the nanowire and sample-to-sample variations.

Temperature-dependence measurements showed a simple Arrhenius behaviour characteristic. It showed that the conductivity of PPy-DNA nanowires increased exponentially with increasing temperature. At temperatures above 380 K, the curve started to deviate from the exponential behaviour which was consistent with the FTIR results. Temperature-dependence measurement results suggested a nearest-neighbour hopping conduction mechanism, and the data indicates that the polymer is thermally stable. Studying the PPy-DNA nanowire properties by this method may open the way to align and characterize similar nanowires that can be used in many nanotechnology applications. This characterization will also help to study and further understand the mechanism of charge transport through PPy-DNA systems.

Finally, further investigation on PPy-DNA nanowires could be suggested, such as the effect of contact resistance on its conductivity using the four probe technique.

Chapter 4: Synthesis and Characterization of Ag-DNA Nanowires

4.1 Introduction

Nanoscale metals have been an area of interest due to their unique physical properties at the nanosize scale, such as quantized conductance [79, 80] and, occasionally, semiconductor behaviour [81]. Due to their low resistivity, silver nanostructures are an area of active research because of possible applications in electronics. There are many attempts to use metal nanoparticles in general [82] and Ag nanoparticles in particular to synthesize nanowires using DNA as a template [18, 83]. For example, Shiqiang, *et al* prepared silver metal nanowires by assembling Ag^+ ions onto DNA templates, and reducing the metal ions using an electrochemical method [84]; Berti, *et al* reported the photo-reduction of DNA-templated silver ions by exposure to UV light resulting in the formation of metallic silver clusters along the DNA molecules [85]; Park, *et al* reported on the electrical conductivity of silver nanowires templated on DNA molecules via two-step chemical deposition of silver upon glutaraldehyde-modified DNA [86]. These attempts were motivated by the desire to decrease the resistance of DNA, which is considered to be in the range of a few GΩ for length of 6.72 nm and 2 nm of diameter [19]. As mentioned before, Braun, *et al* (1998) were the first to demonstrate the possibility to enhance the DNA conductivity using Ag nanoparticles. They synthesised silver nanowires on a DNA template by means of the chemical reduction of silver ions using hydroquinone as a reducing agent [18]. In that work, Ag-DNA nanowires typically up to 15 μm in length and 60-100 nm in diameter showed partly ohmic behaviour in their current–voltage curves with resistances of several MΩ.

In this chapter, the chemical synthesis and characterization of silver (Ag) nanoparticles templated on DNA is presented. The synthesis of silver nanoparticles through the Tollens process was previously demonstrated by Yin, *et al* [87]. However, the time delay in the Tollens process before the reaction occurs is essential in their case to achieve good control over the particle size distribution. In this work, a short time, one-step synthesis process using Tollens' reagent via a chemical route is developed, details of which are included in the next section. The formation of the silver/silver oxide

structure on the DNA template is investigated by means of UV-Vis absorption spectra, FTIR spectroscopy and atomic force microscopy (AFM). The electrical properties of Ag-DNA nanowires were studied using electric force microscopy (EFM) combined with conductive atomic force microscopy (C-AFM) and two terminal electrical measurements.

Note: In this chapter, for convenience Ag-DNA is referred to the 1D nanostructures formed by the action of Tollens' reagent on DNA, even though the chemical characterization of the structures shows the presence of silver oxides as well as metallic Ag.

4.2 Experimental work

4.2.1 Nanowires preparations

Tollens' reagent contains the diamminesilver(I) ion $[Ag(NH_3)_2]^+$. This is made from silver(I) nitrate solution by adding a drop of sodium hydroxide solution to give a precipitate of silver(I) oxide, then adding the minimum dilute ammonia solution required to re-dissolve the precipitate. Freshly prepared Tollens' reagent was used within one hour.

Ag-DNA nanowires were prepared by mixing 20 μL λ-DNA (500 μg/mL) stock solution with 20 μL Tollens' reagent and heated at 50 ºC for about 10 minutes. Ag-DNA nanowires were aligned using the molecular combing technique [15], after a reaction time of 3 days. Typically, 5 μL were dispensed on the substrate and dragged along several times before being removed with a micropipette. AFM images were recorded after the surface was dried at room temperature in a laminar flow hood for 30 minutes.

Bulk samples of Ag-DNA were prepared as follows, 0.5 mL of DNA (sodium salt) solution (162.5 μg/mL;10 mM Tris-HCl pH 8 + 1 mM EDTA) was mixed with 0.5 mL freshly prepared Tollens' reagent and heated at 50ºC for 10 minutes. After complete addition of Tollens' reagent, the solution gradually turned purple in colour. The mixture was allowed to continue reacting at room temperature for 24 hours; a black precipitate of Ag-DNA was formed, and washed with ethanol several times, then dried

at room temperature. For XRD and XPS investigations, a large amount (approximately 100 mg) of the Ag-DNA powder was prepared and collected using the same method.

I should mention here that all the chemical synthesis and reactions were done in the Chemical Nanoscience Laboratory, School of Chemistry, University of Newcastle. The λ-DNA stock solution was also purchased from New England Biolabs UK, and all general reagents, which were of AnalaR grade, were purchased from Sigma-Aldrich.

4.2.2 Infrared spectroscopy

The FTIR spectrum (range 600-4000 cm^{-1} with 4 cm^{-1} spectral resolution) of about 10 μL of dry Ag-DNA solution that deposited on a clean Si(100) substrate was obtained using a Varian 7000 FTIR spectrometer in normal transmission alignment. The spectrum obtained was compared with that of bare DNA solution, with the same amount deposited on a clean Si(100) substrate.

4.2.3 X-ray diffractometer (XRD)

The XRD analysis was recorded from a powder sample using the (XPERT-PRO) XRD system described in chapter 2, section 2.6.3 with graphite monochromatized Cu_{Ka} radiation (λ = 0.15418 nm). A scanning rate of 0.04°/s was applied to record the pattern in the 2θ range from 25 to 70°.

4.2.4 X-ray photoelectron spectroscopy (XPS)

The XPS analysis was performed using an AXIS Ultra X-ray photoelectron spectrometer, with $Al_{K\alpha}$ X-rays as the excitation sources (1486.7eV) operated at 150 W (15 kV, 10 mA). The photoelectrons induced by the X-ray were filtered by a hemispherical analyzer, and recorded by multi-channel detectors at $5x10^{-9}$ Torr chamber pressure. For the survey scan, pass energy was 160 eV and step size 1 eV, while 10 eV pass energy and 0.1 eV step size were set for the high resolution scan. XPS data was collected for Ag-DNA samples prepared as a powder. The powder samples were prepared then placed on a Si(100) substrate ($1cm^2$) and pressed on the surface by another clean Si substrate before being inserted into the XPS chamber. The binding energies obtained in the XPS analysis were corrected for surface charging effects (0.3eV) by the hydrocarbon C_{1s} (284.6 eV) peak, which was used as a

reference. The spectrum was fitted with two Doniach Sunjic doublet functions and with one singlet for the silver plasmon after subtraction of a Shirley-type background.

4.2.5 Scanning conductance microscopy characterizations of Ag-DNA nanowires

AFM imaging of the nanowires was performed in air using a Dimension Nanoscope V system (described in section 2.4.1) with a vibration noise reduction isolation system. Before aligning nanowires, surfaces were cleaned by a series of organic solvents (trichloroethylene, acetone, isopropanol (IPA) and DI water) at about 80°C then blown dry with nitrogen. The substrate was then exposed to Me_3SiCl for about 10 min. Then 2μL of Ag-DNA nanowires solution were dispensed onto the hydrophobic substrate surface, and spun (300rpm) before combing. The chip was left to dry for about one hour. The oxide thickness of the substrate used was 220 nm prepared by dry oxidation and thicknesses determined by a spectrometric thin film analyzer (Filmetrics F40).

In the EFM measurements, an electrostatic field was created between the tip and the sample by applying an independently controlled bias. The bias was applied to the sample while the tip was grounded. The phase shift between the driving frequency and the cantilever resonance frequency is related to the force gradient and is sensitive to polarisability, and to the conductance of nanowires. The first scan is used to acquire the tapping image and in the second scan, the tip is lifted to a height larger than 50 nm above the surface to obtain the EFM phase image.

In the C-AFM measurements, a constant bias was applied between the tip and the sample, while the tip was grounded. The electrical contact between the nanowires and the metallic chuck was made by applying a drop of In/Ga eutectic between the network of nanowires and the chuck. The imaging obtained is called conductive AFM imaging, because it is performed in a contact mode, with an applied bias. The imaged area was typically 1 mm away from the In/Ga contact. For all C-AFM and EFM measurements, MESP probes (n-doped Si cantilevers, with a Co/Cr coating, Veeco Inc.) were used. The probe length was in the range 200-250 μm, with resonant frequency about 79 kHz, quality factor (Q) between 200 and 260, and a spring constant between 1-5 N m^{-1}.

4.3 Results and discussion

4.4.1 Chemical synthesis of Ag-DNA nanowires

In this study, DNA was used as a template to assemble Ag nanowires. The method reported in this chapter is simple and reproducible as described in section 4.2.1. Ag nanowires were formed by reduction of Tollens' reagent in the presence of λ-DNA at room temperature. It is expected that the cationic Ag^+ ions will bind electrostatically to the anionic phosphate backbone of the DNA molecules.

4.4.2 UV-Vis characterization

The interaction between λ-DNA and Tollens' reagent over time was monitored by UV-Vis absorption spectroscopy. The spectrum of bare λ-DNA, recorded at room temperature, exhibits the characteristic absorption band of DNA at 260 nm (Figure 4.1) This spectrum also shows the UV–Vis absorption band of the Ag-DNA solution (440 nm). The solution was allowed to stand for different periods of time at room temperature, and the UV-Vis spectra measured. A shift of the DNA absorption peak (260 nm) towards longer wavelengths was observed.

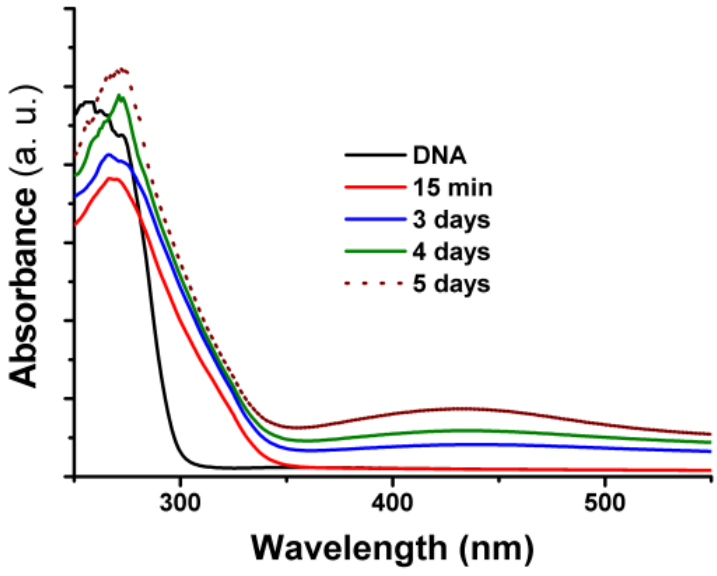

Figure 4.1: UV-Vis absorption spectra of Ag-DNA solution for a range of different incubation time

Figure 4.2 shows a close zoom of the UV-Vis spectra shown in Figure 4.1 in the range from 350-600 nm. It shows that after 3 days, a new band starts to emerge at about 440 nm, which can be attributed to the Ag plasmon and indicates the formation of metallic Ag nanoclusters [88].

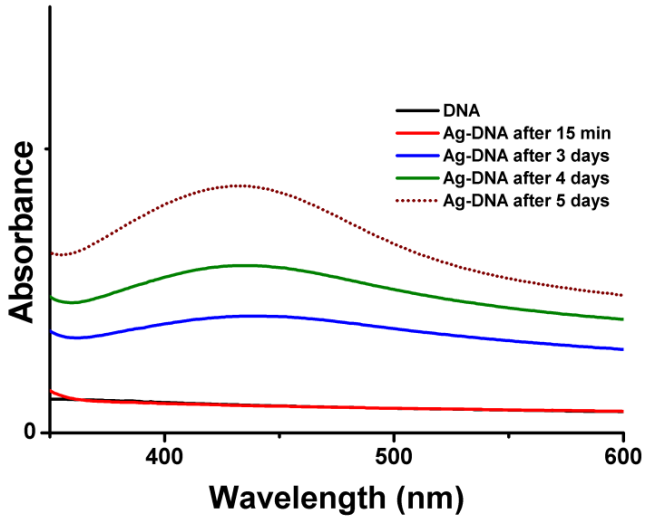

Figure 4.2: UV-Vis absorption spectra of Tollens reagent when mixed with λ-DNA for varying time periods in the range between 400 and 600 nm. The peak formed at 440 nm could be due to formation and agglomeration of Ag nanocrystals

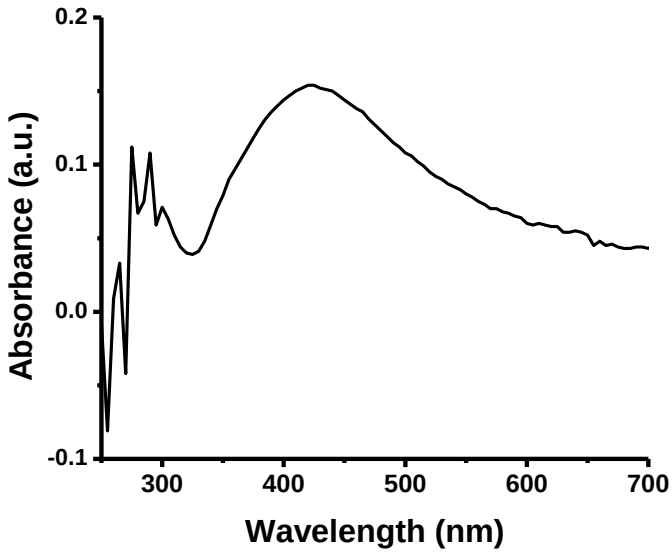

Figure 4.3: UV-Vis absorption spectrum of Ag-DNA powder dissolved in conc. NH_4OH

It should be pointed out here that the peak reported in the literature at 420 nm was attributed to surface plasmon excitation between the metal and dielectric material as in

references [89] and [90]. Zhang, *et al* also attributed the peak at 420 nm to the appearance of spherical Ag nanoparticles [91]. In this work (Figure 4.2), the intensities increase and the peak formed at 440 nm is red shifted. This may be due to the dissolution of smaller Ag clusters. On the other hand, a smaller amount of Ag-DNA powder dissolved in conc. NH_4OH confirms the presence of the peak at 420 nm, as shown in Figure 4.3.

4.4.3 FTIR spectroscopy of silver nanoparticles with DNA

In general, the metal ions interact directly or indirectly with sites characterized by high electron density or negatively charged residues of DNA. Such sites on DNA could be the negatively charged phosphates of the backbone of both strands and the electron donor atoms (N and O) of the bases. The predominant mode of metal binding takes place at the N7 and O6 of guanine and N7 and N1 of adenine bases, as well as the N3 of the pyrimidines [23]. For example, Arakawa *et al* [83] used FTIR spectroscopy to examine the interaction of Ag(I) with calf-thymus DNA. They found that Ag^+ binds to DNA at the N7 of guanine, when present at low cation concentration, whereas at higher metal ion concentrations, Ag-adenine interaction is via the N7 site.

In this work, the FTIR spectral changes of prominent Ag-DNA vibrations were monitored and compared with those of bare λ-DNA (Figure 4.4). The solid line in the spectrum demonstrates the characteristic in-plane vibrations of bare DNA; 977 cm^{-1} (C-O deoxyribose, C-C), 1067 cm^{-1} (P-O or C-O backbone stretch), 1132 cm^{-1} (PO^{2-} symmetric stretch), 1227 cm^{-1} (PO^{2-} asymmetric stretch), 1337 cm^{-1} (C-N stretch thymine, adenine), 1412 cm^{-1} (C-H, N-H deformation, C-N stretch), 1473 cm^{-1} (C8-N coupled with a ring vibration of guanine), 1530 cm^{-1} (in-plane vibrations of cytosine and guanine), 1597 cm^{-1} (purine stretch, N7), 1707 cm^{-1} (guanine and thymine)[92]. The dotted line shows the FTIR spectra after DNA was mixed with Tollens' reagent. It showed major spectral changes of the DNA in-plane vibrations. The guanine band at 1711 cm^{-1} for example is shifted to higher frequency (1667 cm^{-1}) upon silver oxide interaction. Purine stretch band intensity at 1600 cm^{-1} decreased and shifted slightly to 1598 cm^{-1}. The in-plane vibrations of cytosine and guanine at 1530 cm^{-1} have completely disappeared, but the band at 1476 cm^{-1} (C-H, N-H deformation) showed an increase in its intensity and shifted to higher wavelength (1403 cm^{-1}). The C-N stretch

of thymine and adenine (1337 cm^{-1}) intensities also increased and shifted to higher frequency (1360 cm^{-1}).

The disappearance of the phosphate band at 1132 cm^{-1} indicates that the Ag^{+} binds to phosphate groups, and is confirmed by the appearance of a new absorption peak at 838 cm^{-1}. Moreover, the backbone stretch band (P-O, C-O) at 1067 cm^{-1} decreased in intensity and shifted to lower frequency (1051 cm^{-1}). In summary, it is noticeable that the vibrational frequencies of DNA are markedly altered in the presence of Tollens' reagent in the solution containing DNA. This change confirms the intimate interaction between the silver nanoparticles and the DNA.

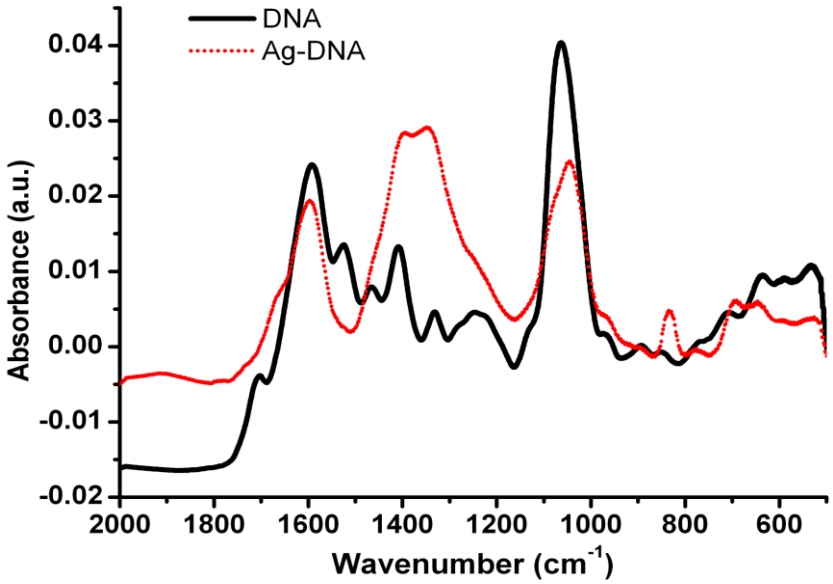

Figure 4.4: Comparison of FTIR spectra of bare λ-DNA before mixing with Tollens' reagent (solid line) and after (dotted line)

4.4.4 X-ray diffraction (XRD) investigations

The X-ray diffraction pattern of Ag-DNA powder sample is shown in Figure 4.5. The predominant peak at $2\theta = 32.36°$ corresponds to the (111) plane of the cubic Ag_2O phase [93] and can be seen along with other relatively weaker peaks at $2\theta = 54.94°$. The XRD also shows diffraction peaks at 27.94°, 46.33°, 39.00° and 42.00° corresponding to Ag_3O_4, and broad peaks at 38.30°(111), 44.68°(200), 64.74°(220), 67.65° and 77.40° (311) corresponding to Ag metal [94]. The unassigned peaks are very likely to be components of the buffer or salts originating from the Tollen's reagent solution.

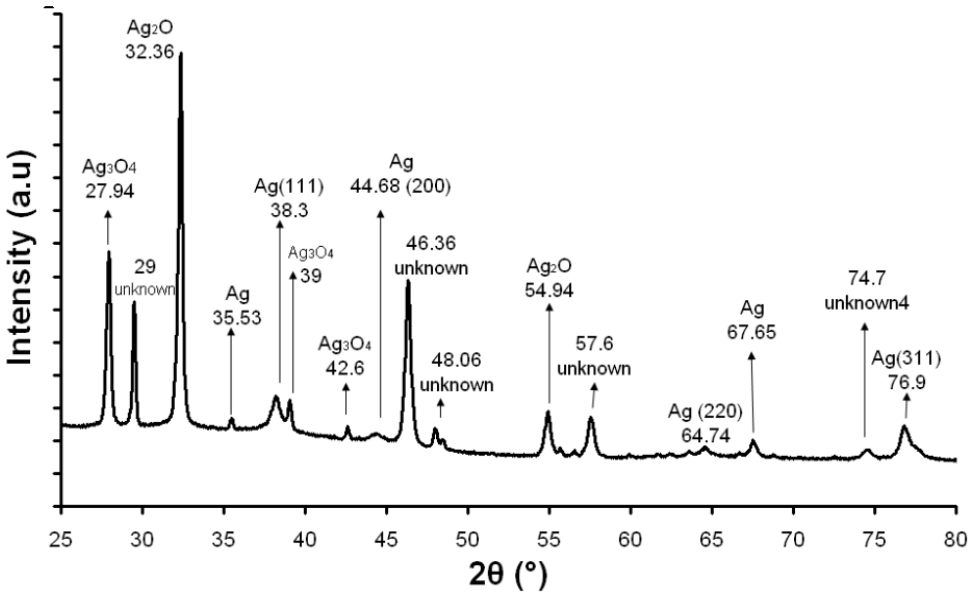

Figure 4.5: XRD spectrum of powder sample of Ag-DNA nanowires

The estimated Ag nanoparticle size calculated from the Scherrer formula [36] confirm the presence of nanocrystals with an average diameter of 24 nm.

4.4.5 X-ray photoelectron spectroscopy (XPS) measurements

All XPS experiments were performed with an Axis Ultra electron spectrometer (Kratos) using a monochromated Al–K_α source operated at a power of 225 W with an X-ray source of hv=1486 eV. A low energy electron gun was used to compensate for the build up of sample surface charging. Axis Ultra XPS software was used to process the data, while analysis of the spectra was carried out using WinSpec software. Binding energies were referenced to the C_{1s} line set at 284.6 eV. The XPS survey spectrum (Figure 4.6) obtained with 160 eV pass energy included peaks arising from Ag_{3p} levels, O_{1s} and small peaks, including N, Na and P. The latter indicates the presence of the DNA.

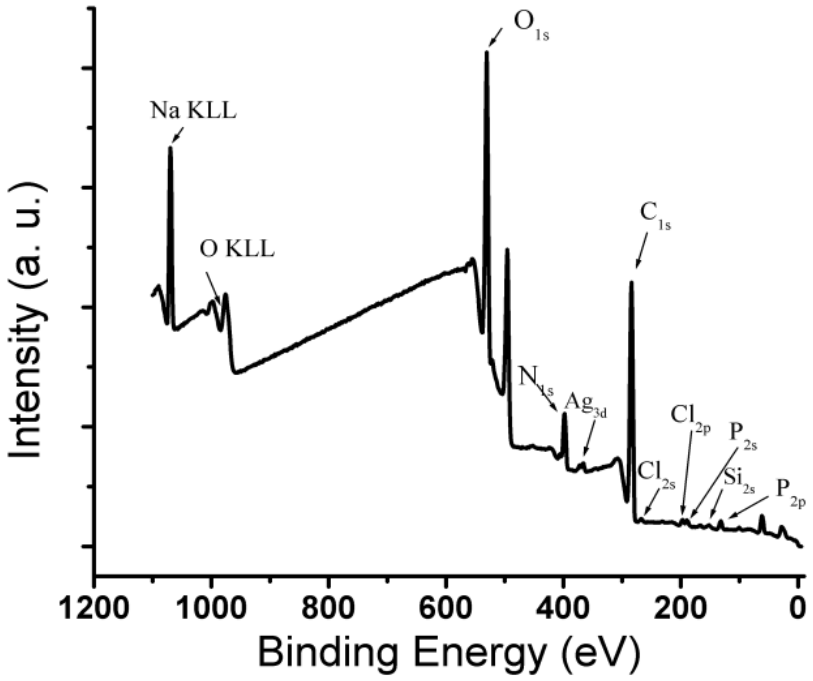

Figure 4.6: XPS survey spectrum obtained from the Ag-DNA nanowire powder sample

The O_{1s} region of the spectrum shown in Figure 4.7 reveals the presence of two components in the band spectrum as indicated by the noticeable shoulder on the O_{1s} peak. After fitting, peaks at 529.38 eV, 531.03 eV and 534.11 eV are seen under the main envelope. These observed peaks are attributed to the presence of oxygen in the Ag nanoparticles, which is in reasonable agreement with the literature [95, 96].

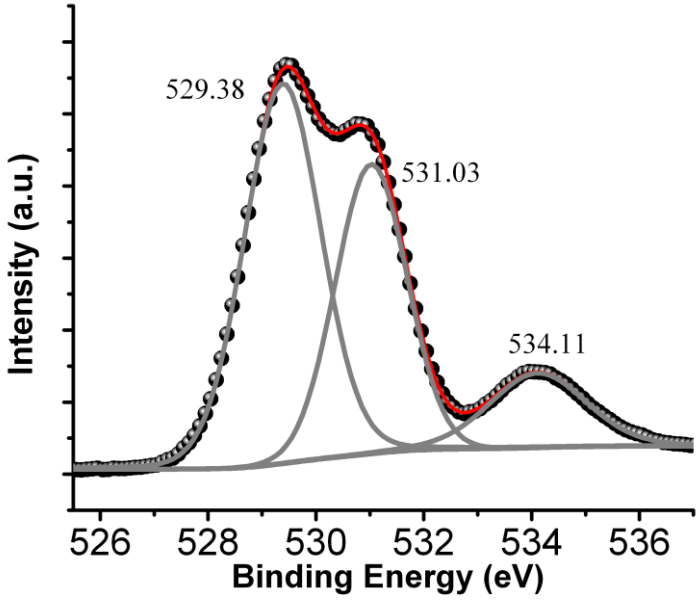

Figure 4.7: XPS spectra of O_{1s} of Ag-DNA powder sample

The hollow circles in the spectrum represent the experimental data, which is superimposed with a solid line representing the fit. Peak (529.38 eV) suggests that the sample contains Ag coated with Ag_2O. As XPS is sensitive to the sample surface, it shows more Ag_2O on the surface than Ag and can be represented schematically as shown in the schematic diagram in Figure 4.8. This result is consistent with the XRD data, which show a mixture of Ag_2O and Ag. Fit components (excluding the Shirley background) are also shown inside the experimental spectrum.

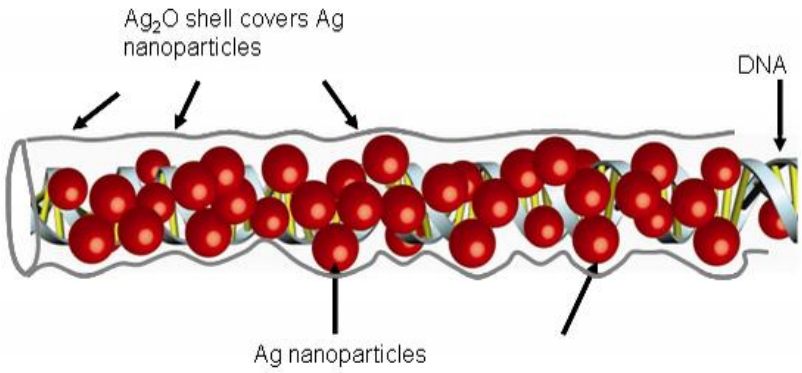

Figure 4.8: Schematic diagram of DNA templated Ag nanoparticels covered by Ag_2O shell

The high resolution XPS of Ag $_{3d}$ peaks obtained from the Ag-DNA powder sample is shown in Figure 4.9. The binding energy (BE) of the $Ag_{3d5/2}$ peak obtained from the powder sample is 367.4 eV, and its full width at half maxima (FWHM) is 1.2 eV and has an intensity of 8.2. The presence of large Ag nanoclusters could be responsible for the relatively high FWHM of the $Ag_{3d5/2}$ peak. These analyses show reasonable agreement with data reported by [97-99]. One can assign the peak at 367.4 ± 0.1 eV to Ag, and the small doublet peak at 368.2 ±0.1 eV to Ag_2O (this is within the experimental errors of the results).

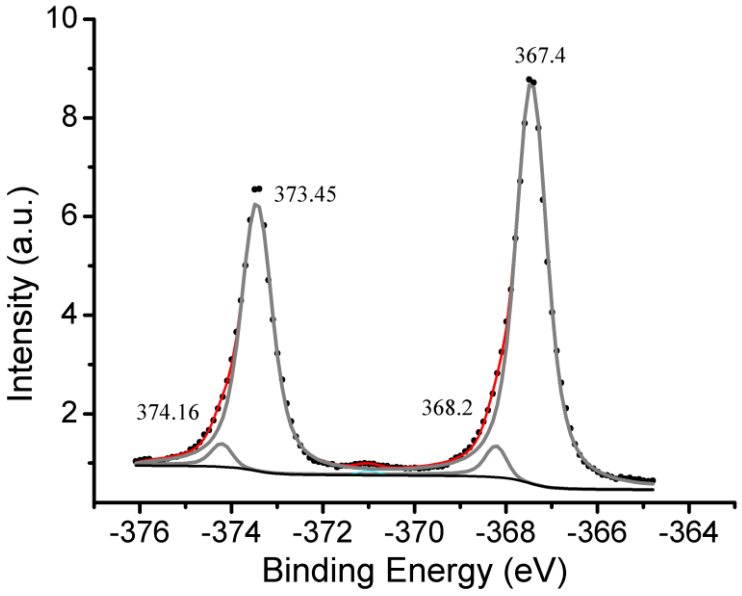

Figure 4.9: High resolution XPS spectrum of the Ag_{3d} region of the Ag-DNA powder sample. Peaks are fitted with two Doniach Sunjic doublets with broadening and one singlet for silver plasmon after subtraction of a Shirley-type background. The solid circles represent the experimental data superimposed with a solid red line correspond to the fit. Fit components are also revealed within the experimental spectrum.

Figure 4.9 also shows an Ag peak at 368.2 eV, which has FWHM of 0.43 eV and intensity of 0.64. This apparently indicates that the presence of Ag_2O in the powder sample is high compared to the Ag. It also shows a single peak at 371 eV, which originates from excitation of the silver surface plasmon at 3.6 eV; this peak is therefore shifted by 3.6 eV from the main Ag $3d_{5/2}$ peak at 367.4 eV with reasonable agreement with Altieri *et al.* [100]. Finally, it should be noted that the XRD data is representative of the composition of the crystalline material throughout the sample, but the XPS data is more sensitive to the surface of the nanowires. Taking the XRD and XPS results together, these experiments show that the Ag-DNA nanowires are best represented as a metallic Ag core coated with an oxide, mainly Ag_2O.

4.4.6 Atomic force microscopy (AFM) studies

AFM investigations show a distinctive morphology associated with the Ag-DNA nanowires. It also shows that silver nanoparticles assemble themselves along the DNA molecules, resulting in nanowires of different diameters (25-90 nm) and varying lengths of up to about 150 μm (Figure 4.10). A mixture of the molecular combing

technique and spin coating is highly effective in aligning Ag-DNA nanowires upon the surface of the substrates.

Spin coating (300 rpm) a drop of solution containing nanowires before molecular combing proves effective in stretching nanowires across the substrate surface. This is an important preliminary step, allowing the nanowires to be easily stretched out and positioned upon a substrate. This step is important for aligning nanowires across two Au electrodes easily for electrical characterizations. Figure 4.10 also shows AFM images of DNA strands covered densely with silver oxide nanoparticles, and few of which remain in the background. Nanowires obtained with different height can be attributed to the presence of bundles of DNA and/or formation of larger nanoparticles.

Ag nanocrystals are shown and noticeable well attached along a long DNA stretch (Figure 4.11). Part of the nanowire exhibits a beads-on-a-string appearance, while the rest of the nanowire forms a continuous nanowire (Figure 4.10). A higher resolution AFM scan size image (Figure 4.12) of these nanowires shows that they are often very rough and granular in appearance. Interestingly, this extremely long Ag-DNA nanowire is much longer than the 16 microns of our λ-DNA. It is therefore clear that the Ag-DNA nanowires can contain more than one DNA molecule and that the Ag also can join together multiple DNA molecules to create a much longer nanowire than the underlying template.

Improving the morphology of Ag deposited on the DNA templates will be discussed in the next chapter. It is expected that the initial stage of the interaction process is the attachment of small Ag nanoparticles to DNA (Figure 4.13), followed by continuous growth along DNA.

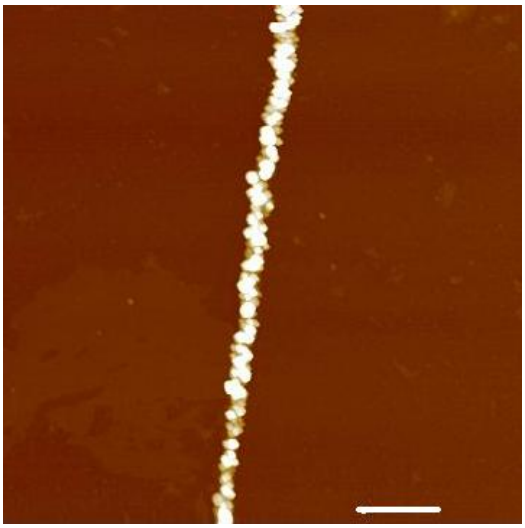

(a)

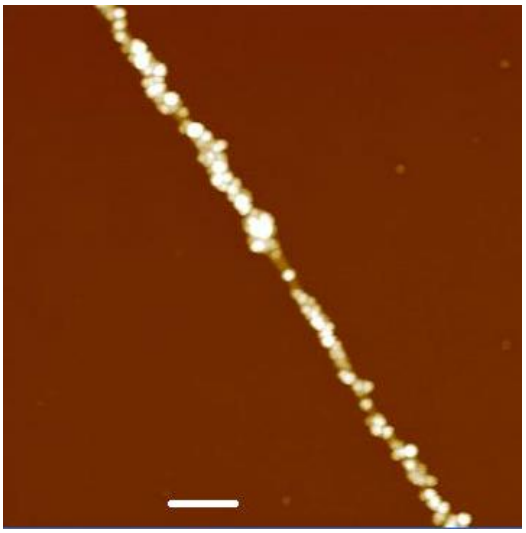

(b)

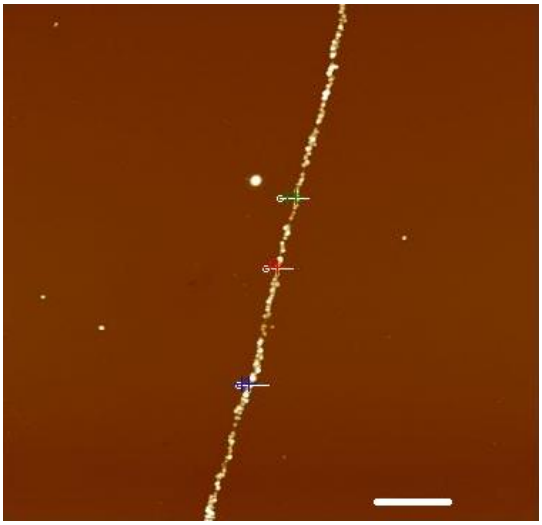

(c)

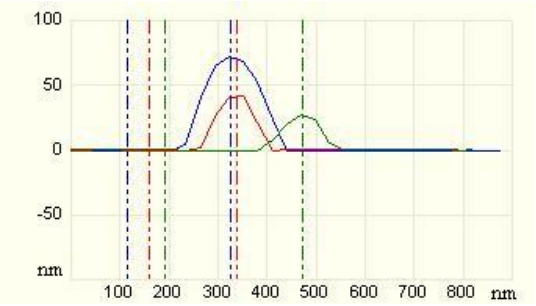

(d)

Figure 4.10: (a) AFM image of DNA-templated Ag nanowire;(a) scale bar 1µm and height scale is 150 nm; (b) 2µm scale bar and height scale 100 nm.(c) scale bar 2µm and height scale 160 nm. Cross section profile of (d) showing variation in the thickness of the nanowire

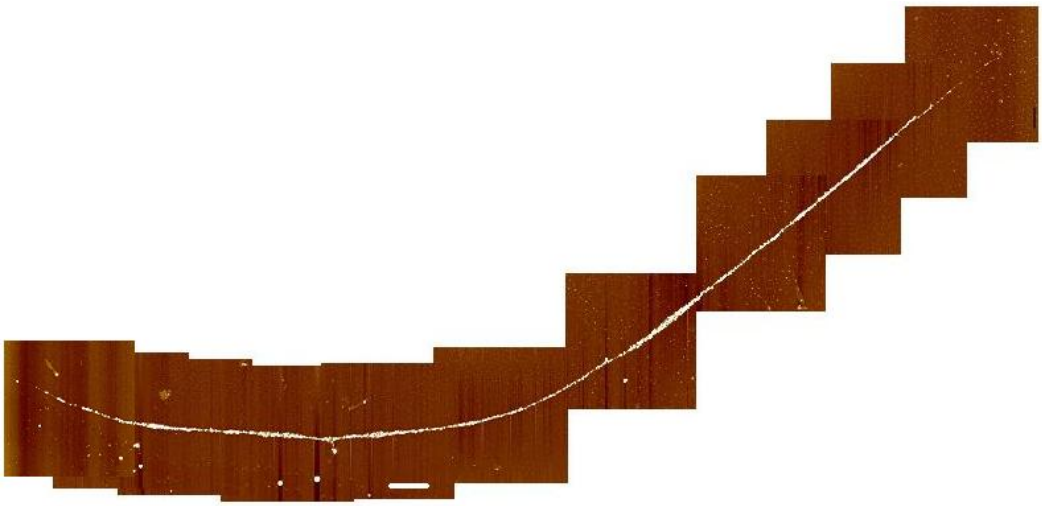

Figure 4.11: AFM Tapping Mode ™ height image of 50 μm long Ag-DNA nanowire. Scale bar indicates 2μm and the height scale is 45 nm

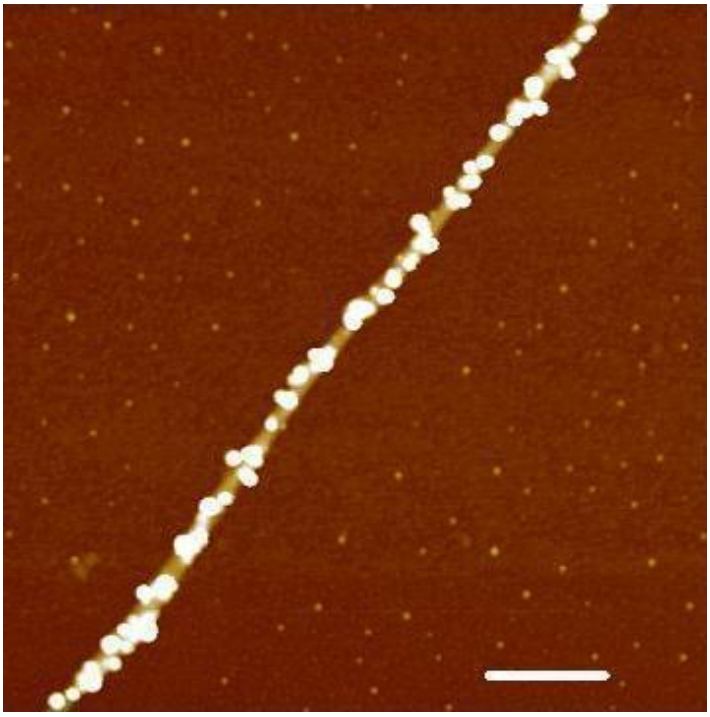

Figure 4.12: AFM Tapping Mode™ image of section of DNA-templated nanowire shown in Figure 4.11. The scale bar is 500nm and height scale 58 nm

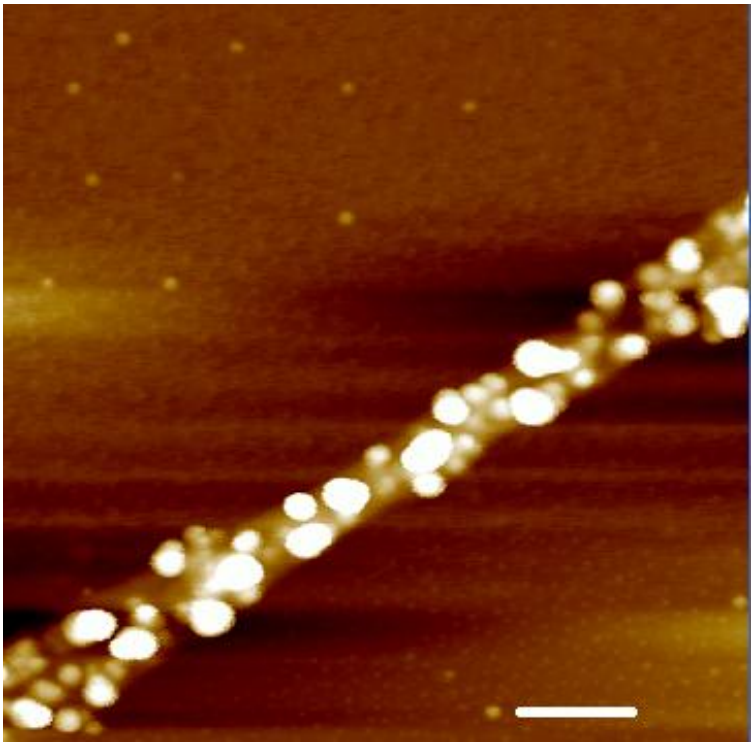

Figure 4.13: A small scale AFM Tapping Mode™ image of the DNA-templated Ag nanowire shown in Figure 4.11. Scale bar is 250 nm and scale height 58 nm. It highlights that nanoparticles imbedded in the DNA are not just attached on the surface

4.4.7 Two terminal I-V measurements

Two Au microelectrodes were manufactured using the photolithography technique (described in detail in chapter 2). Before aligning the nanowire, silicon chips containing the electrodes were treated with chlorotrimethylsilane (Me_3SiCl) vapour for about 15 minutes to reduce the surface wettability. Then, a 3 µL drop of Ag-DNA solution was deposited on the chip and spun (300 rpm). After that the drop was drawn off the surface using a pipette and filter paper leaving a single nanowire (Figure 4.14) connected across the two electrodes. Using probe station, I-V curves of a single nanowire can be measured easily as shown in Figure 4.15.

4.4.8 The temperature dependent measurements

The temperature dependence of I-V curves of a single Ag-DNA nanowire have been investigated using Cascade Microtech Summit 11000 series probe station with Hewlett Packard semiconductor device analyzer (HP/Agilent B1500A) controlled by Agilent

EasyEXPERT software. By placing the chip containing the nanowire on the hot plate, the temperature was monitored and controlled. A series of voltages were applied between the testing electrodes and the current measured. The temperature was then raised and allowed to stabilise before the same measurements were recorded again. This process was repeated over a range of temperatures from 320 to 400K.

The conductance started to stabilize above 310 K even though samples were kept in the dark and isolated from external electrical noise during the measurements.

The temperature dependence curves (Figure 4.16) obtained shows that the conductance increases as temperature increases. This behaviour can be expressed by Arrhenius.

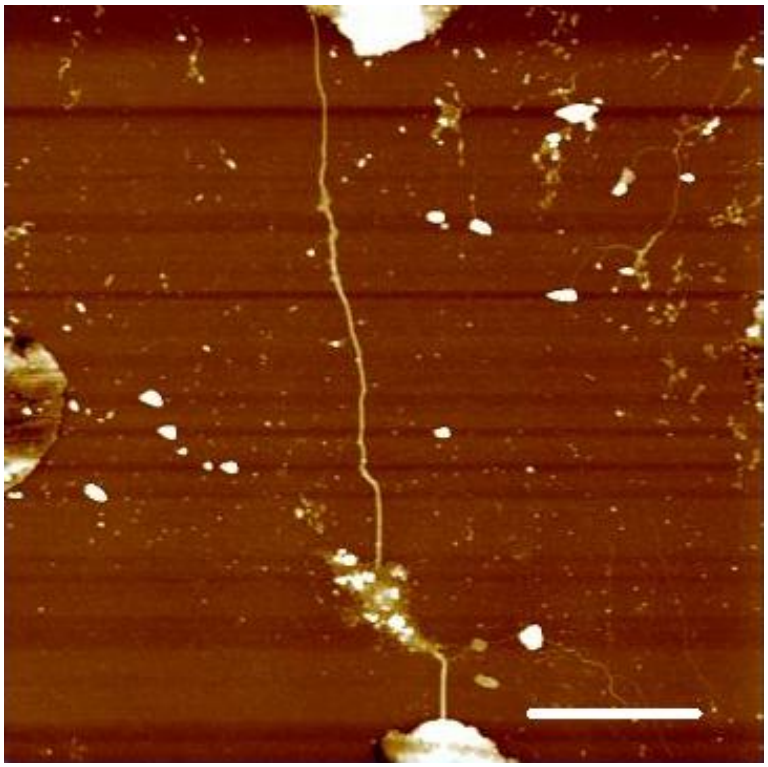

Figure 4.14: AFM Tapping Mode^{TM} image of single Ag-DNA nanowire connected to Au electrodes (nanowire length $\ell \approx 8.5$ µm, average radius ≈ 8 nm). Scale bar 2 µm. and height scale 30 nm[101]

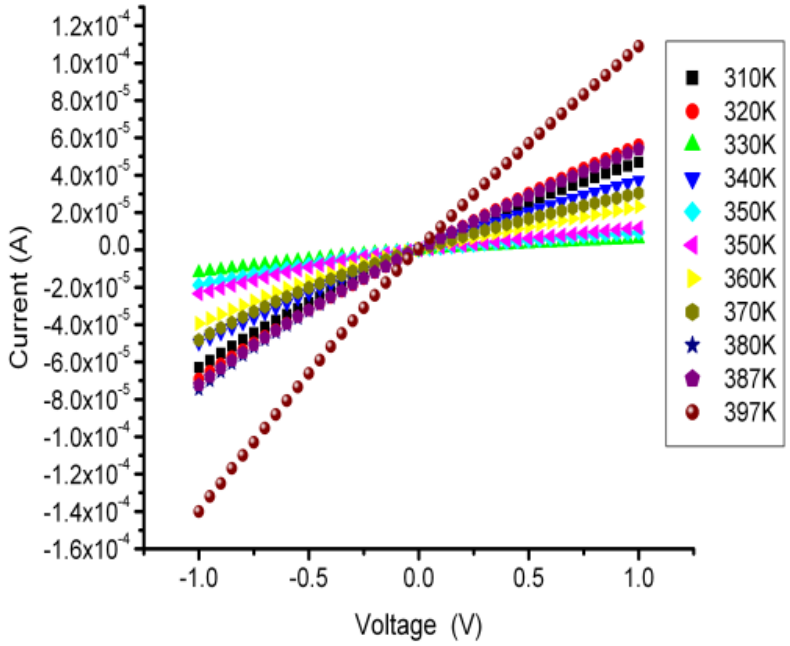

Figure 4.15: Temperature dependence of I-V curves of single Ag-DNA nanowire aligned between two Au electrodes

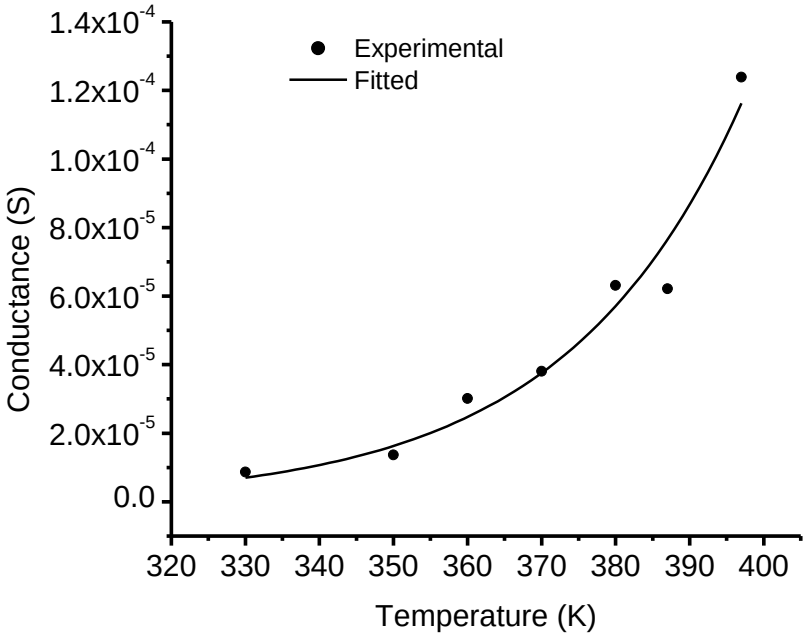

Figure 4.16: Conductance of a single Ag-DNA nanowire varying with temperature

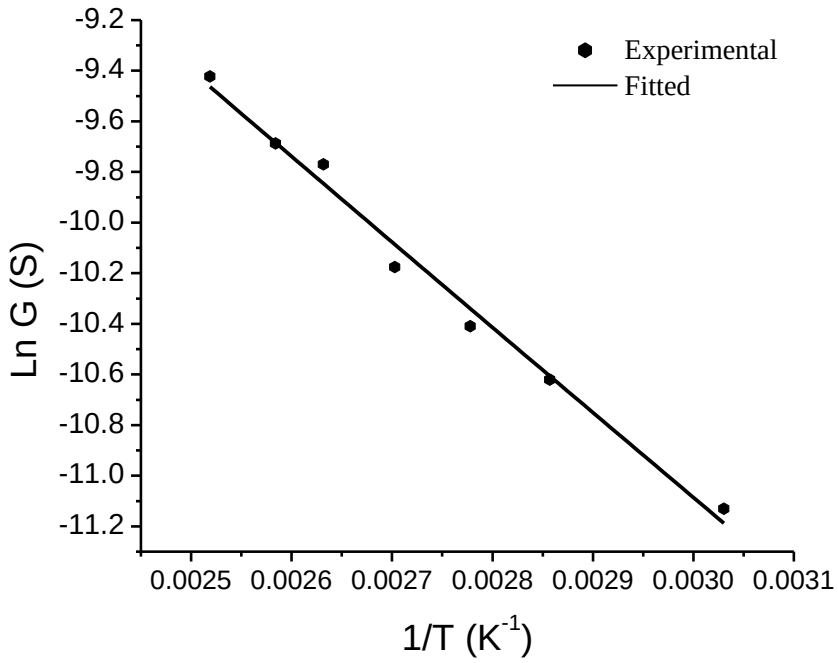

Figure 4.17: Temperature dependence of conductance of single Ag-DNA nanowire

Figure 4.17 shows the plot of $\ln G$ against T^{-1}. From this figure, it is possible to obtain the activation energy $\Delta E = 3450\, k_B$ in unit of k_B, which, interpreted as a band gap (ΔE=2E_g), gives a value of $E_g \approx 0.3$ eV. This data shows that the band gap energy is small compared to the reported band gap for Ag_2O thin film (1µm) 1.46 eV [102] and 1.2 eV [103]. If the value of ΔE were related to the band gap of Ag_2O, as the material heated more charge carriers are expected by thermal excitation. If this were true, ΔE should be close to these numbers. Therefore, it is not reasonable to think that the model describing intrinsic semiconductor and thermal excitation of electrons from the valence semiconductor band. Instead, this suggests that the nanowire should not be regarded as a simple semiconductor, but that a hopping mechanism is responsible for the conductance between localized states or between small adjacent Ag nanoparticles imbedded into the oxide and attached to DNA. This result is supported by the UV-Vis, FTIR, XRD and XPS results, which indicate that nanowires comprise metallic Ag coated with silver oxide and attached to the DNA surface.

4.4.9 Electrostatic force microscopy (EFM) investigation

EFM is a convenient method to study the conductivity of Ag-DNA nanowires. It gives a contactless method of probing the conductance of nanowires. Its simplicity arises from the acquisition of both topographical and electrical properties of the sample in a single experiment. An easy distinction can be made between bare DNA (apparent height 0.5 nm, positive phase-shift in the EFM image) and that of a DNA with a metal coating deposited upon it (diameter is higher than 1 nm, negative phase-shift in the EFM image).

Previous studies [46] showed that conducting single-wall carbon nanotubes have a negative phase-shift, with respect to the background. In contrast, insulating materials like poly(ethylene oxide) nanofibers show a positive phase shift which increases with fiber diameter. Where the phase shift ($\Delta\phi$) for an insulating object also estimated using a model geometry in which the Ag-DNA nanowire is represented by the area of a thin dielectric strip directly under the tip, itself modelled as a disc of radius, R_{tip} as in chapter 3. The first term in the equation is the background contribution due to the tip/oxide/Si capacitance and the second term is due to the tip/Ag-DNA nanowire/Si capacitance. Whilst the phase shift equation (3.1) is based on an approximate geometry, it clearly shows that the phase shift, $\Delta\phi$, is positive for any finite value of the dielectric constant of the nanowire, ε_{nw}. However, when the nanowire is conductive, the charge stored on the Ag-DNA nanowire/Si capacitor can be spread along the whole length of the nanowire. In effect, the second term in the equation becomes much larger. A parabolic dependence of the phase shift on potential is expected for the conductance effect in EFM and this can be distinguished from the linear variation that arises from the electrostatic force caused by trapped charges [55, 59]. Quantitative calculations of the phase shift as a function of nanotube diameter are described in references [46] and adapted in this work in a qualitative fashion to demonstrate the conductive nature of our Ag-DNA nanowires.

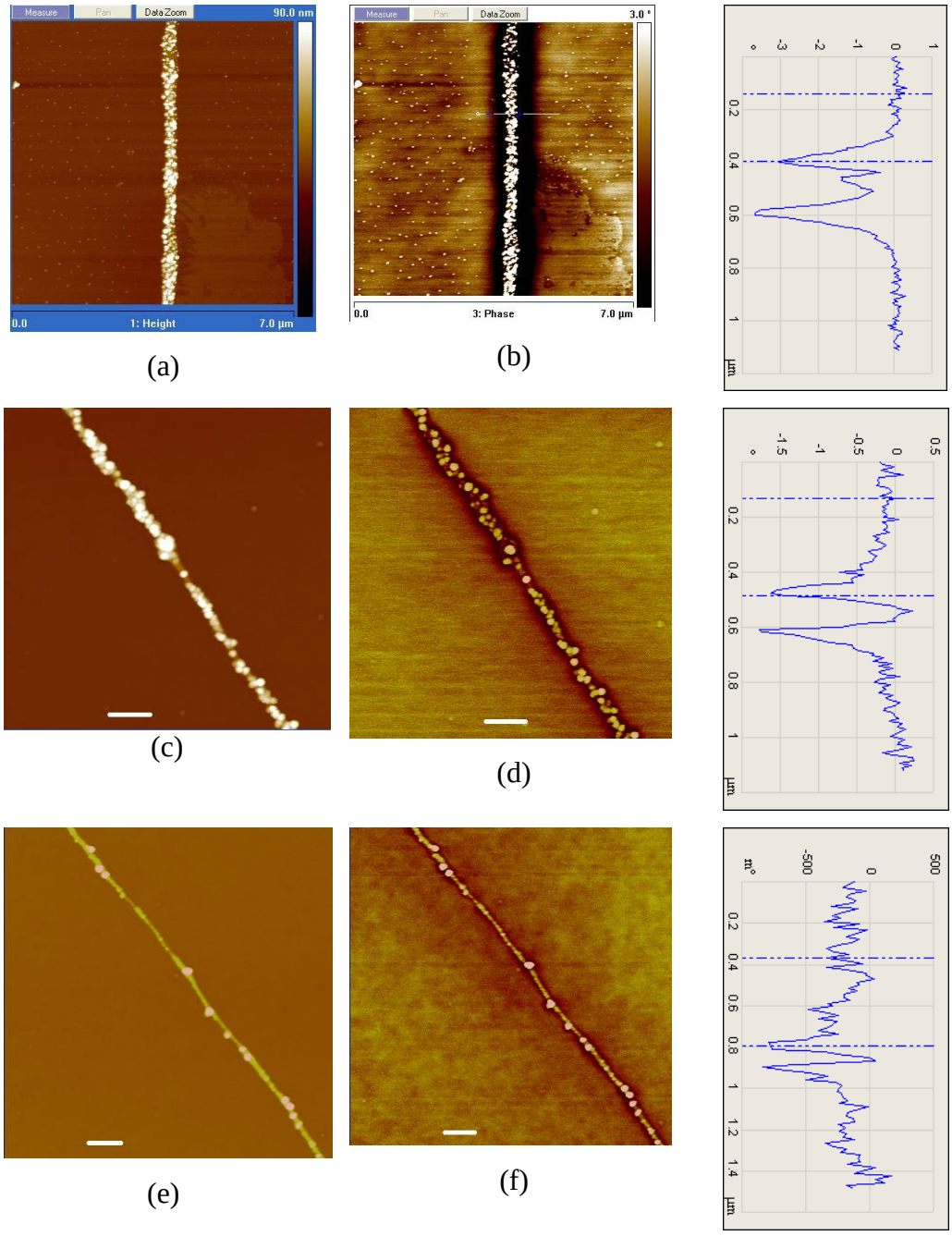

Figure 4.18: AFM Tapping Mode™ images of Ag-DNA nanowires aligned on Si/SiO_2(220 nm) substrate (a,c,e) (scale bar 500nm and height scan 7nm) and its corresponding EFM phase images (b,d,f) (scale bar 500nm and phase scale 3˚). The EFM phase cross sections at the right hand side show that the denser the nanoparticles, the greater the phase shift

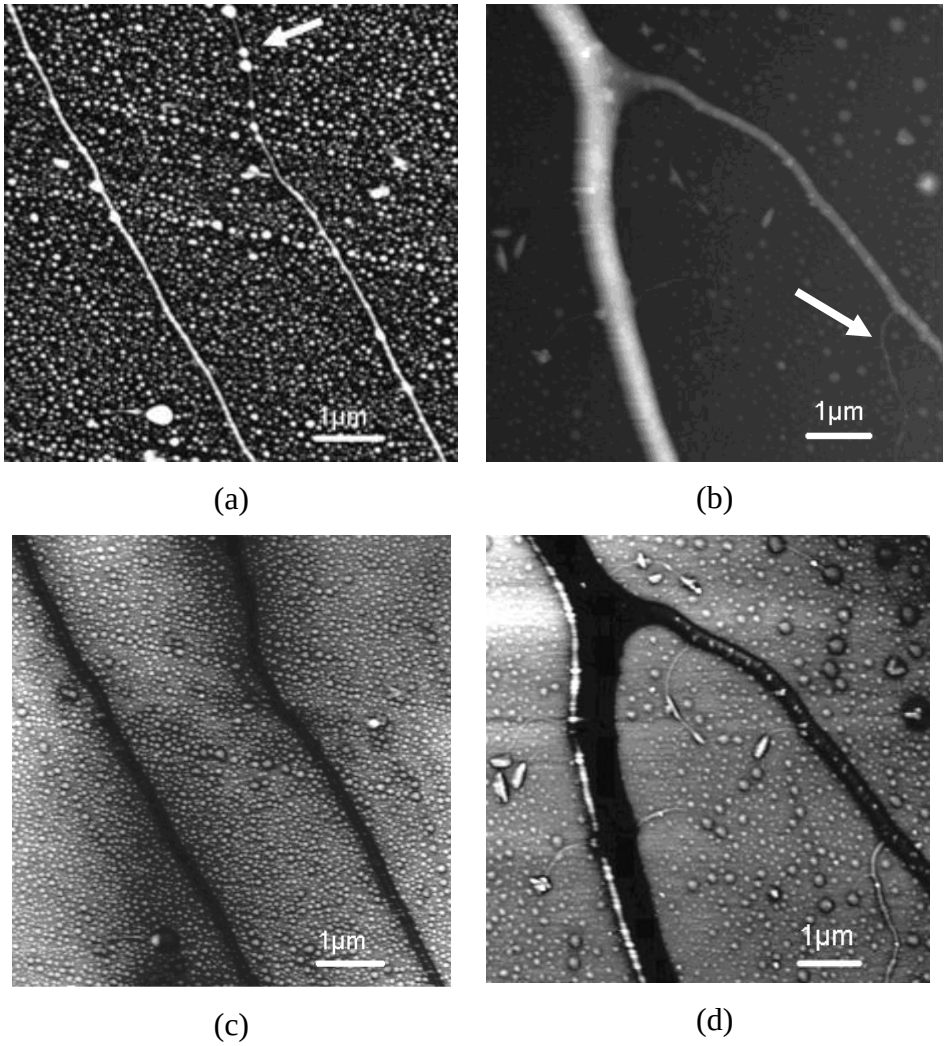

Figure 4.19: Tapping Mode™ AFM images of Ag-DNA nanowire aligned on a Si/SiO_2 (220 nm) surface (a,b,c); Corresponding EFM phase (c,d) shift images(V_{EFM}= -7V, lift height 50 nm and data scale height correspond to 3°). Scale bar 1µm and height scale correspond to a) 35 nm, b) 280 nm [101]

The EFM images (applied bias V=-7V, lift height 50 nm) of more condensed nanoparticles attached to DNA are shown in Figure 4.18 and Figure 4.19. These figures show that the Ag-DNA nanowires exhibit dark lines compared to the white background of the insulator SiO_2 surface. Although the surface is covered with many Ag particles that are not templated, the continuous conduction pathway along the DNA-templated strand is clearly visible as the dark lines in Figure 4.19 c & d. This is a very useful aspect of EFM; it allows to image conduction pathways and demonstrate the electrical contact between the grains in the Ag-DNA nanowires. Part of the nanowire shown in Figure 4.19 (a) appears not completely covered by Ag nanoparticles (indicated by arrow), even though its EFM image (c) exhibits a negative (dark) contrast in this region. This suggests that the nanoparticles are nevertheless

connected by Ag deposits along the DNA structure in this region. In contrast, non-templated nanoparticles and bare DNA (arrow in b) exhibit a positive (white) contrast in the EFM image (Figure 4.19 (d)).

A typical phase shift along a line section crossing the nanowire is shown in Figure 4.20. It depicts a parabolic variation of phase-shift (at its maximum point on the cross-section) with voltage, but with a slightly asymmetric shape, which may be attributed to trapped charges in nanocrystals. It can be seen that the nanowire of larger diameter (D=45 nm) exhibits a larger phase-shift than the nanowire of smaller diameter (D=12 nm). This reflects the change in capacitance of the tip/nanowire/substrate system as the wire diameter increases.

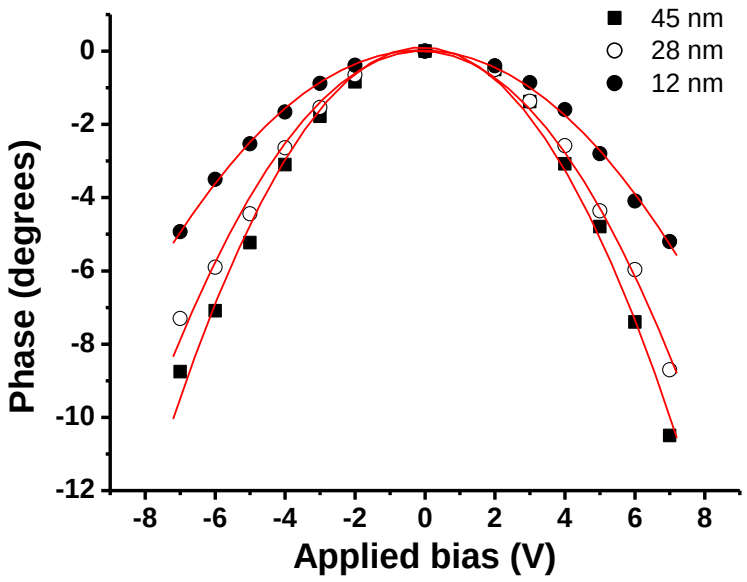

Figure 4.20: Phase shift versus tip sample bias of nanowires with different diameters 45, 28, and 12 nm.

4.4.10 Conductive AFM (C-AFM) investigations

C-AFM has been used to electrically characterize the Ag-DNA nanowires. This technique is quite powerful as it can simultaneously map the topography and the current distribution of the nanowire, in the range of hundreds of femtoamps to nearly microamps [104-106]. C-AFM images are generally acquired in contact mode, with metal-coated cantilevers. In the C-AFM experiment, the Ag-DNA nanowires were deposited and aligned on the Si/SiO_2 substrate, which was connected to the metallic

chuck. The metallic tip of the cantilever was used to act as the other electrical contact. The C-AFM images were recorded at a bias of 0.5 V, applied between the cantilever and the substrate. Figure 4.21(a) shows a contact mode AFM image (height) of a thick Ag-DNA nanowire with a diameter of about 50 nm. The deflection error image of the nanowire (Figure 4.21 (b)), which is the difference between the measured deflection and the setpoint presents a more obvious image of the nanowire. The current map image Figure 4.21 (c) shows areas of high conductivity and low conductivity regions. Evidence of conductivity is only observed on regions of the substrate where the nanowires are located.

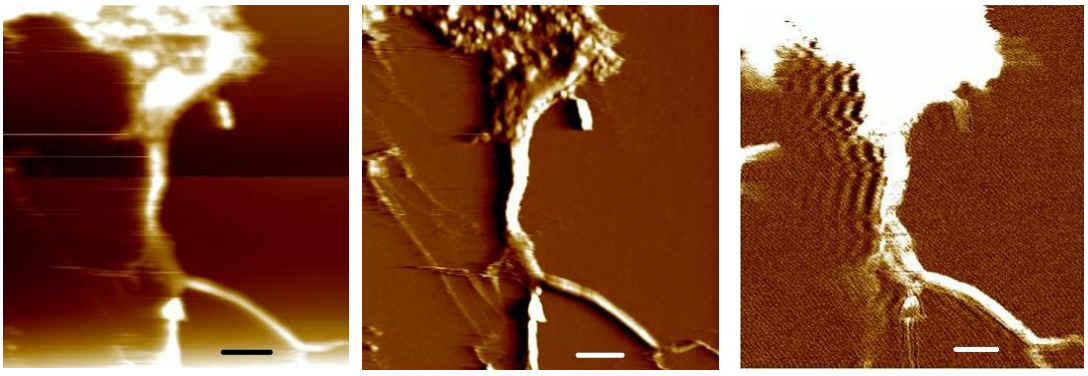

(a) (b) (c)

Figure 4.21: C-AFM of Ag-DNA nanowires aligned on a Si/SiO_2 (220nm) substrate (a) Contact mode image, the data scale corresponds to a height of 60 nm; (b) Deflection error image (the data scale corresponds to a height of 20 nm) and (c) C-AFM current image (the data scale corresponds to a current of 100 nA). The tip-sample bias was 0.5V; the images (a)-(c) were acquired simultaneously. Scale bar 1 μm (a-c)

The closed loop system of the Dimension V instrument makes it possible to reproduce the positioning of the cantilever at a point of interest on the Ag-DNA nanowire and record I-V curves. The tip was therefore positioned in the middle of the nanowires, and I-V curves are recorded for two deflection setpoints.

The bias was swept from -10 to +10V, while the deflection setpoint was gradually increased from 0.5 to 1V. The measured current was then plotted against the drive voltage, as can be seen in (Figure 4.22).

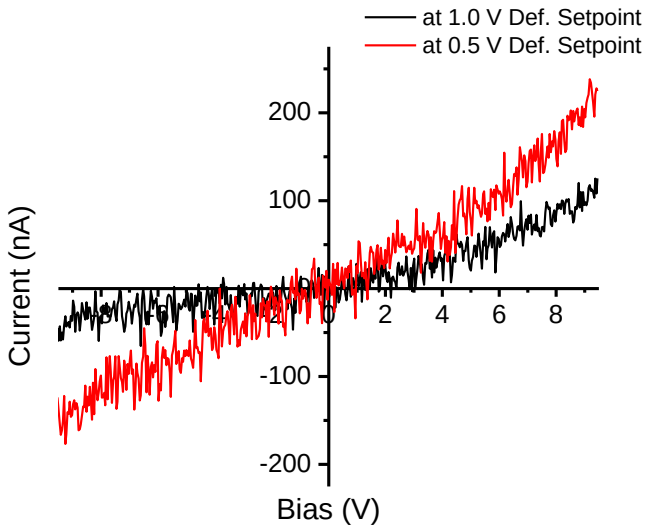

Figure 4.22: C-AFM I-V curves of an Ag-DNA nanowire for different deflection setpoints. Each curve was recorded at the same X-Y position on the sample

The curves exhibit a simple ohmic behaviour. Not surprisingly, as the deflection force increased, the current also increases– this suggests a contribution from the tip/wire contact to the overall resistance. Changes in the I-V characteristics with applied force are a signature of significant contact resistance, which varies as a function of load. At a setpoint of 1.0V, the total resistance is lower than that corresponding to 0.5V deflection setpoint, which indicates the contact resistance, can be reduced by applying a deflection contact force on the nanowire by the tip, as might be expected for an oxide-coated structure.

4.4 Conclusions

In this chapter, the synthesis of Ag nanowires has been reported, through the chemical reduction of Ag^+ using Tollens' reagent, on a DNA template. UV-Vis absorbance spectroscopy confirms the interaction between the λ-DNA and Tollens' reagent. FTIR results have shown that the vibrational frequencies of purine and pyrimidine are markedly altered upon reaction with Tollens' reagent, confirming the interaction between the Ag and DNA bases. XRD and XPS studies confirm the presence of Ag in the Tollens treated DNA samples. The conductivity of uniform Ag-DNA nanowires and nanoropes was investigated and confirmed by EFM and C-AFM techniques. Moreover, two-terminal I-V measurements upon single Ag-DNA nanowires have been also demonstrated, and were produced over ranges of temperatures. This data shows

that the conductance of Ag-DNA nanowires increases as the temperature increases. From the ohmic part of the I-V curve, the conductance was calculated and the temperature dependence of the conductance followed an Arrhenius' behaviour. Interpreting the activation energy as a bandgap is untenable because the value extracted from the data is about 0.6 eV, which is much less than the bulk gap of Ag_2O and incompatible with metallic Ag, even nanoscale Ag. On other hand, if the nanowire were a true metal, it would show an increase in resistance with increasing temperature. Therefore, the data cannot be adequately explained in terms of metallic conduction. The data are described much better by the use of a hopping model in which the activation energy represents the energy barrier between nearest-neighbour sites between which the electron hops.

Chapter 5: Templating Ag on DNA polymer hybrid nanowires: control of the metal growth morphology using functional monomers

5.1 Introduction

Conducting polymers are candidates for use as nanomaterials in electronic applications [107]. Nanowires based on materials such as polypyrrole (PPy) [22], poly(methyl pyrrole), polyaniline [108] and polythiophene [109, 110] have many advantages compared to carbon nanotubes and silicon nanowires because of their tuneable conductivity, flexibility, chemical diversity and ease of processing [111]. An important advantage of conducting polymers is that they can be synthesized in a controlled manner using a variety of protocols, such as chemical synthesis and templated electrochemical synthesis. Further, polymer nanowires are of interest because of the possibility to chemically functionalise the wire using simple methods of organic synthesis to derivatise the monomer, or to incorporate novel properties through the choice of the basic monomer unit. As mentioned in chapter 3, PPy has already been shown to have the electrical properties necessary for use as a molecular conductive nanowire. Also, polythiophene has been used with PPy and is considered ideal for use in synthesis of molecular nanowires. Combining these molecular nanowires and using DNA as a template for them produces easily synthesized nanowires, which exhibit electrical conductivity. DNA has been used as a template on to which metals and conducting polymers can be deposited in the form of nanowires [112, 113]. The advantages of this technique are the simplicity of the chemical procedures and the robust nature of DNA, which is also available in precisely defined lengths. However, DNA-templated metal nanowires are often very rough, even irregular in appearance as shown before in chapter 4, whereas DNA-templated polymers are smooth, but less conductive [114].

In this chapter, the templating of Ag on DNA/polymer nanowires to form hybrid nanowires was investigated. It has been shown that a metal-binding functionality (alkynyl) can be introduced into DNA-templated polymer nanowires by chemical modification of the 2-(thiophen-2-yl)-1H-pyrrole (TP) monomer, and used to improve the morphology of Ag deposited on this hybrid template.

5.2 Materials and methods

λ-DNA (500 ng μL^{-1}) was purchased from New England Biolabs (cat no. N3001 1S, Hitchin, Herts. SG4 0TY United Kingdom). Silver nitrate and all chemicals used in this experiment of AnalaR grade or equivalent were purchased from Sigma–Aldrich and used without any further purification process. All the solutions were prepared in water from a Barnstead nanopure purification train with nominal resistivity 18.2 MΩ cm.

5.3 Methods

It should be noted that chemical synthesis of the alkylation of 2-(thiophen-2-yl)-1H-Py (TP) samples was performed by Dr. Miguel A. Galindo and Jennifer Hannant as in reference [115] in the Chemical Nanoscience Laboratory, School of Chemistry, University of Newcastle, but all the templating reactions and characterization (spectroscopic, AFM imaging and electrical measurements) were conducted by the author.

5.3.1 General procedure of alkylation of 2-(thiophen-2-yl)-1H-pyrrole

Poly-TP (PTP) was prepared by the following method: The solvent dimethylformamide (DMF) (anhydrous) (50 ml) was added to TP (1.0 g, 6.8 mmol) via cannula under nitrogen. Sodium hydride (60 % dispersion in mineral oil) (0.32g, 13.4 mmol) was then added under nitrogen and was left to stir for 30 min at room temperature. 5-chloro-1-pentyne (1.4 ml, 13.4 mmol) was added and the mixture was allowed to stir for 5 hr. Reaction completion was monitored by thin layer chromatography (TLC). Upon completion, the mixture was then filtered through a celite pad to remove any unreacted sodium hydride. Water was added and the resulting mixture was extracted with CH_2Cl_2 and then dried over magnesium sulphate. DMF was removed in vacuum and the mixture was dried.

5.3.2 Templated electroless deposition of silver

λ-DNA solution (20 μL), or an equivalent amount of polymer-templated DNA, was mixed with 20 μL Tollens' reagent and heated at 50°C for 10 min. Tollens' reagent was prepared from a mixture of 200 μL aqueous $AgNO_3$ (0.5% wt/vol) and 5 μL

NaOH (5% wt/vol) and the precipitate was dissolved in 600 μL NH_4OH (conc. NH_4OH diluted 2% in H_2O).

5.3.3 Polymer (TP or alkynyl-TP) templating on DNA

Pentynyl-TP was chemically polymerised by $FeCl_3$ forming poly(ATP) which reacts in basic medium with Tollens' reagent producing poly(Ag-ATP). 5-chloropent-1-yne was then added so that an SN_2 displacement generates the ATP. Sodium hydride was added to facilitate the removal of the proton on the pyrrole, this was observed as effervescence which is due to hydrogen evolution. The sodium cation stabilises the nitrogen anion. In basic medium, ATP reacts with Tollens' reagent forming poly(Ag-ATP). Terminal alkyne hydrogens in poly(ATP) are slightly acidic and in basic medium can be easily deprotonated to form terminal alkyne anions, which tends to form silver-alkyne complexes by interaction with silver cations (Scheme 5.1).

5.3.4 Probe microscopy

Prepared nanowires were deposited by drop coating on Si chips with a 210 nm-thick grown oxide layer formed by dry oxidation as described in chapter 2. Before the deposition, the surface of the substrate was silanised in Me_3SiCl vapour for 10 minutes. Nanowires were aligned by spinning and molecular combing method.

AFM imaging. Tapping mode AFM images were acquired in air using a Dimension Nanoscope V system with NanoProbe tip. AFM images are taken in tapping mode using cantilever of 200-250 μm long, 252 kHz resonant frequency and 1-5 N m^{-1} spring constant.

C-AFM measurements. C-AFM measurements were performed using the same system described in chapter 2, except for using MESP Veeco probes n-doped Si cantilevers, covered by Co/Cr layers with resonant frequency of about 74 kHz, spring constant k = 2.8 N/m and quality factor Q, between 240 and 260. The tip was grounded and ± 7V bias was applied to the chuck holding the chip with nanowires connected to the chuck by means of Ga/In eutectic.

EFM measurements. EFM measurements were carried out using the same system described above, but with a suitable bias applied to create an electrostatic field between the tip and the nanowire. For EFM phase imaging, the lift height was 60 nm, the tip resonant frequency was about 74 kHz, spring constant = 2.8 N m^{-1} and the

quality factor = 260. The tip was grounded and a DC bias was applied to the Si chip (Si(100), p^{++}, doping).

5.4 Results and discussion

By comparison of the three types of Ag nanostructure formed on DNA templates, this experiment has shown that the morphology of the Ag deposit can be controlled by the incorporation of Ag-binding groups in the template (Scheme 5.1). FTIR spectra of poly(alkynyl-TP) films prepared by $FeCl_3$ oxidation [109] show a complex fingerprint region typical of conjugated polymers and the two major bands expected for the alkynyl group: a carbon-carbon triple bond stretch at 2120 cm^{-1} and a C–H stretch due to the sp hybridised C–H bonds at 3302 cm^{-1}. The TP units in the polymer probably do not couple strictly head-to-tail, but with a random orientation. However, this does not affect the measurements and the TP monomer is convenient for incorporation of alkynyl functionality by N-alkylation.

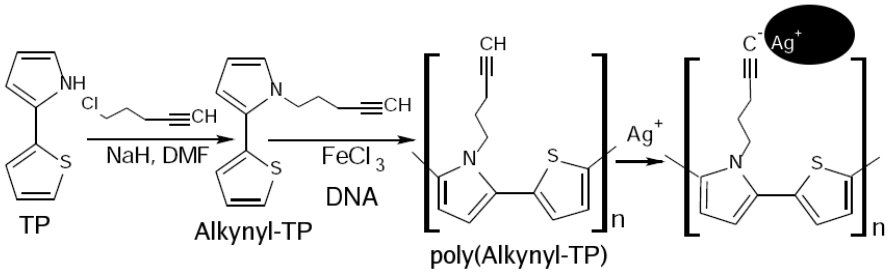

Scheme 5.1: DNA-templated poly(alkynyl-TP) nanowires and deposition of Ag nanocrystals [116]

5.5 AFM characterization

For simplicity, it is helpful to use the notation that Poly(alkynyl-TP)/DNA denotes polymer templated on DNA and Ag/DNA or Ag/poly(alkynyl-TP)/DNA denote the structures formed after electroless deposition of Ag on the bare DNA and the hybrid polymer/DNA templates. Figure 5.1 shows AFM images (height and phase) of these nanostructures. Samples were prepared by the reaction of Tollens' reagent with λ-DNA under ambient light conditions and with mild heating (50°C, 10 min). The growth of Ag nanocrystals along the DNA molecule is clearly observed and C-AFM measurements demonstrate that the nanocrystals are in electrical contact [116]. This beads-on-a-string morphology is quite typical of DNA-templated metals. It has been previously shown in this thesis that conductive polymers produce much more regular

and smooth nanowires when templated on DNA by oxidative chemical polymerisation of the monomer in a solution of λ-DNA. Figure 5.1(b) and (c) are typical AFM images for Ag/poly(alkynyl-TP)/DNA and Ag/poly(TP)/DNA; these nanowires are quite thick (~20 nm) and rather smooth.

The wires lie straight in these images because they have been ‘‘combed” across the surface by the flow in a dragged water droplet. Figure 5.1 (b–d) show another phenomenon which has been noted previously: the compensation of the charge on the double helix by the polymer causes nanowires to wrap around each other to form a nanorope. It is also possible that the Ag nanowire in Figure 5.1 comprises more than one DNA molecule.

The conductive polymer-based nanowires are smooth and regular in structure, but their conductance is much less than for true metals. Nevertheless, chemical functionality can easily be incorporated into the polymer nanowire using a functional monomer. It was decided to modify the TP monomer by attaching a propyl chain with a pendant alkyne group to the N-atom of the Py unit (Scheme 5.1). DNA-templated polymerisation of this monomer produces nanowires and nanoropes indistinguishable (by AFM) from those formed by the unmodified TP. However, when the TP nanowires are treated with Tollens’ reagent, the growth of Ag deposits on the nanowires is strongly influenced by alkynyl group (Figure 5.1). On TP/DNA, the Ag forms a relatively small number of nanocrystals and, compared to those on the alkynyl polymer, they are quite large. This is probably due to the absence of a strong Ag^+ binding site on poly(TP), which results in sporadic nucleation of only a few Ag clusters. On poly(alkynyl-TP), the nucleation of Ag is facile because of the well-known interaction of alkynes and Ag(I): initially Ag^+ forms a sigma bond to the sp carbon after loss of the alkynyl proton, but polymerisation of such complexes via pi-interactions also occurs [117]. On the poly(alkynyl-TP)/DNA nanowire, many small nanocrystals are formed, and they are so close together and uniformly distributed over the template that they are only distinguished in the phase image (Figure 5.1 (d)).

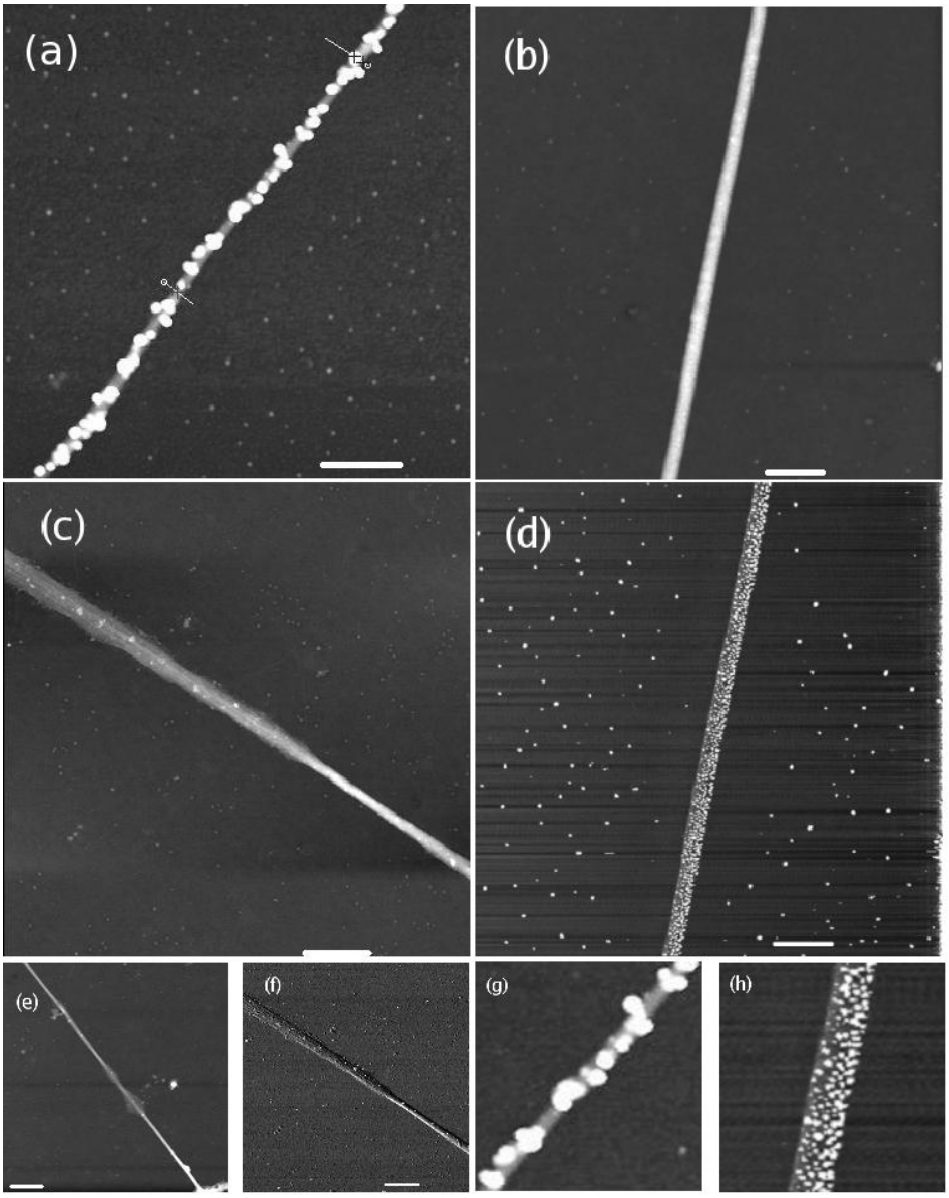

Figure 5.1: Tapping mode AFM images of nanowires on SiO_2/Si. (a) Ag/DNA, height; (b) Ag/poly(alkynyl-TP)/DNA, height; (c) Ag/poly(TP)/DNA, height; (d) Ag/poly(alkynyl-TP)/DNA, phase; (e) Ag/poly(TP)/DNA, larger scale 7μm^2, height image; and (f) Ag/poly(TP)/DNA, phase (g) and (h) show expanded views of (a) and (d), respectively. All scale bars are 1 μm [116]

5.6 Electrical measurements

In order to determine which of the nanostructures are conductive, two-point I–V measurements in C-AFM and a variant of EFM were used.

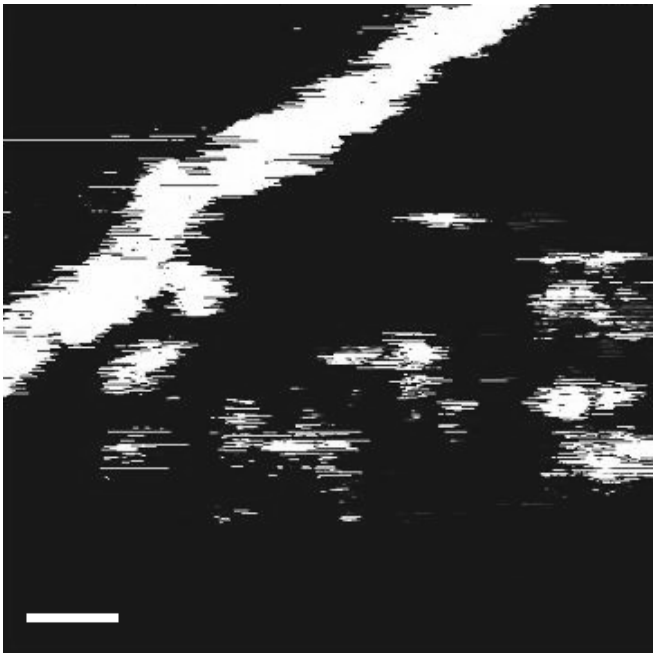

Figure 5.2: A C-AFM current image of an Ag/poly(alkynylTP)/DNA nanowire. The tip/ sample bias potential was 10 V, the scale bar is 1 µm and the grayscale corresponds to 100 nA [116]

Figure 5.2 shows a current image of an Ag/poly(alkynylTP)/DNA nanowire on an Si chip acquired by C-AFM. One contact to the nanowire is a drop of In/Ga eutectic placed on the chip and the other is the metallised AFM tip. When the tip contacts the oxide, no current is observed (black background in (Figure 5.2). However, when the tip touches the nanowires, a current flows (ca. 10^{-7} A @10 V in Figure 5.2). The current pathway to the remote In/Ga contact exceeds the scan range, and therefore C-AFM is unsuited to a precise determination of conductivity, but it does convincingly demonstrate the nanowire is conductive. As was previously noted, nanowires are easily disturbed during contact mode imaging, and therefore the current image does not have the resolution of the tapping mode images of Figure 5.1.

Figure 5.3 shows scanned conductance (phase) images of several nanowires. Ag/DNA nanowires give large, bright spots corresponding to Ag clusters (Figure 5.3a), which are presumably not in good electrical contact with the rest of the wire (dark shadow). Of the other structures, only the Ag/poly(alkynyl-TP)/DNA nanowire shows similarly large negative phase shifts (Figure 5.3 e). Those wires are also much more uniform than the pure Ag/DNA wire (Figure 5.3 c), and this confirms that most of the Ag clusters of Figure 5.3 (e) are in good electrical contact.

The expected parabolic dependence of phase shift on bias for voltages between -7 and +7 V was observed; this confirms the phase is due to the "scanned conductance effect" rather than trapped charge, which produces phase shifts that depend linearly on bias voltage. In the absence of deposited Ag, the polymers show smaller phase shifts, and the negative–positive–negative phase profile previously observed for conductive polymer fibers was observed in this experiment [118]. Figure 5.4 shows the variation of phase shift (over the middle of the wire) with the tip/substrate bias.

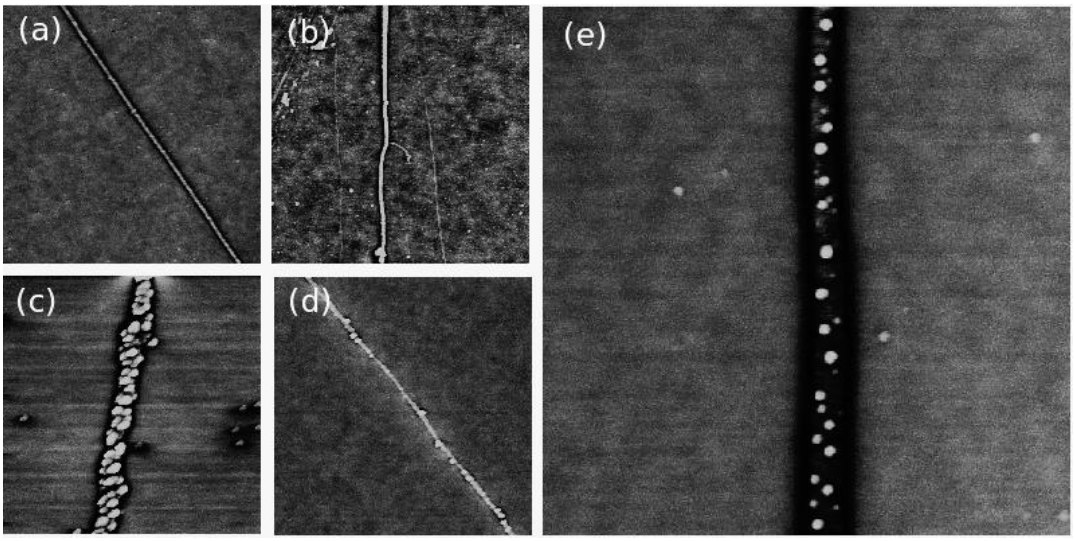

Figure 5.3: EFM phase images of various nanostructures; (a) poly(TP)/DNA; (b) poly(alkynyl-TP)/DNA; (c) Ag/DNA; (d) Ag/ poly(TP)/DNA and (e) Ag/poly(alkynyl-TP)/DNA. The lift height was 60 nm and the grayscale corresponds to 3°. The scan sizes (μm) are (a) 6.3, (b) 4.1, (c) 3.3, (d) 5.4 and (e) 4.0 [116]

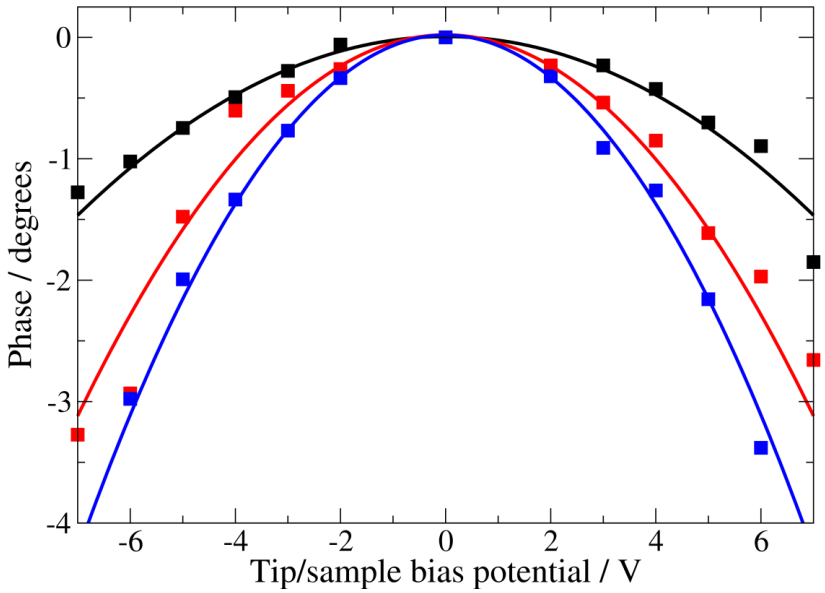

Figure 5.4: EFM phase shift against applied tip/substrate voltage for: poly(alkynyl-TP)/DNA (black); Ag/poly(alkynyl-TP)/DNA (red) and Ag/DNA (blue) [116]

5.7 Conclusions

It has been shown that alkynyl functional groups can be incorporated in conductive polymer nanowires in a convenient manner by chemical modification of the monomer. Alkynyl groups are known to bind Ag^+ and were chosen to encourage nucleation and growth of Ag on the polymer/DNA template; this was demonstrated using tapping mode AFM to image the morphology of the nanowires and conductive AFM and EFM phase imaging to demonstrate their electrical conductivity. The main advantage of using this method is in producing smoother nanowires than normal method of templating Ag directly on DNA. The DNA-templated Ag has a structure that typically consists of small particles of Ag spaced along the template; if the particles are close together, they may be in good electrical contact. The Ag template on the alkynyl polymer template is much smoother, although high resolution phase images do show a nanoparticulate structure. Nevertheless, EFM and C-AFM data show that there is good electrical contact between these particles. The Ag/polymer/DNA nanowires show higher conductance than the polymer /DNA nanowires, which are too resistive for many applications, e.g., interconnects. Further investigation of these metal/polymer hybrids could produce better nanowires with both reasonable conductivity and the smooth morphology of the polymer nanowires.

Chapter 6: Synthesis and characterization of conductive DNA-templated Cu_2O nanowires

6.1 Introduction

Among several methods that have been developed to metalize DNA templates with different metals, cuprous oxide (Cu_2O) has recently received increasing attention as a semiconductor material. Cu_2O is considered a p-type semiconductor with promising applications in many areas such as fabrication of low-cost solar cells [119] and gas sensing [120]. Different Cu_2O nanostructures have been synthesized by many groups; for example, Zhang *et al* prepared Cu_2O nanocrystals via a chemical route. In that work, $NaBH_4$ was used as the reducing agent while DMF was used as a solvent. $NaBH_4$ working as a strong reducing agent, reacts with a trace amount of H_2O in DMF and then reduces $Cu(CH_3COO)_2$ to Cu_2O nanocrystals[120]. Wang *et al* [121] synthesized crystalline Cu_2O nanowires by a chemical method in the presence of a suitable surfactant, polyethelene glycol, at room temperature and Gou *et al* reported another structure, nanocubes of Cu_2O, which can be synthesised by solution-phase methods [122]. Cu_2O nanowires have also been reported using an electrochemical method with an alumina membrane as a template [123] and Orel *et al* [124] demonstrated that Cu_2O nanowires can be chemically prepared using diethylene glycol as the reducing agent.

Different preparations give Cu_2O films with different resistivity. For example, the electrical resistivity at RT of the Cu_2O film prepared by pulsed magnetron sputtering of powder targets, measured using a four-point probe technique was reported to be 412 Ω cm [125], while the resistivity of the electroless-chemical deposited Cu_2O films was of the order of 10^4–10^5 Ω cm [126] which is very high compared to the 10^2–10^3 Ω cm for the bulk Cu_2O [127]. Cu_2O nanoparticles have been synthesized by several groups. However, to my knowledge, Wang *et al* is the only published report of assembled Cu_2O nanoparticles on DNA to form necklace-like 1D nanostructures. Though, the electrical properties of such nanostructures were not reported [128].

In this chapter, a new method to synthesise Cu_2O nanowires using the DNA templating strategy is described and electrically characterised. Formation of Cu_2O upon DNA was

achieved through chemical reduction using an alkaline solution of a cupric citrate complex (Benedict's reagent) and ascorbic acid as the reducing agent in solution at room temperature. The structural properties and chemical composition of nanowires were characterized by means of FTIR spectroscopy, UV-Vis absorption spectroscopy, XRD and XPS. The morphology and electrical properties of the resulting nanowires were investigated by AFM, EFM and C-AFM.

6.2 Experimental work

6.2.1 Preparation of Benedict's reagent

Benedict's reagent was prepared by dissolving 0.173 g of tri-sodium citrate and 0.10 g of anhydrous sodium carbonate in 8 mL nanopure water (solution A). Then 0.173 g of cupric sulphate (pentahydrate) was dissolved in 20 mL nanopure water (solution B). Immediately before use, Benedict's reagent was prepared by mixing 0.2 mL solution A with 0.8 mL solution B.

6.2.2 Preparation and alignment of Cu_2O-DNA nanowires

Cu_2O-DNA nanowires were prepared by mixing 20 μL λ-DNA (500 ng μL^{-1}) solution with 20 μL of freshly prepared Benedict's solution. Then 0.2 M ascorbic acid (aqueous solution) was added in drops to the solution (approx 10 μL); afterwards the mixture was allowed to react at room temperature for 1 hour prior to analysis. Cu_2O-DNA nanowires were aligned by the molecular combing technique[33]. In order to facilitate the alignment of nanowires on Si/SiO_2 substrates; the hydrophobicity of the SiO_2 surface was increased by treating the Si/SiO_2 substrates with chlorotrimethylsilane (Me_3SiCl) vapour for about 10 minutes. Typically, 2-3 μL Cu_2O-DNA solution were dropped on the substrate surface and combed across the surface before removal of the excess solution with a micropipette and/or filter paper.

6.3 Techniques used for characterisations

6.3.1 Fourier transform infrared spectroscopy

FTIR spectra (in the range 500-1800 cm^{-1}) were recorded in absorbance mode with a Bio-Rad Excalibur FTS-40 spectrometer (Varian Inc., Palo Alto, CA) equipped with a liquid nitrogen-cooled deuterated triglycine sulphate (DTGS) detector, and were collected at 128 scans with 4 cm^{-1} resolution. The DNA used was prepared through drop casting of solutions of the DNA upon chemically oxidized Si (100) p-type substrates. Cu_2O-DNA solutions (8 μL) were deposited on a clean Si substrate. Both solutions were allowed to dry for 1 hour prior to analysis.

6.3.2 UV-Vis absorption spectroscopy

The UV-Vis absorbance spectra were recorded on a Thermo Spectronic GENESYS 6 spectrophotometer (wavelength range from 250 to 900 nm). Approximately 0.5 mL of calf-thymus DNA (CT-DNA) solution (162.5 μg/mL; 10 mM Tris-HCl pH 8.0 mMEDTA) was mixed with 0.5 mL freshly prepared Benedict's solution. Then ascorbic acid (0.2 M) was added dropwise to the solution (approx 0.250 mL). After the addition of the ascorbic acid was completed, the Cu^{2+} blue colour gradually turned red (after 10 min). The UV–Vis. spectra of the resulting Cu_2O-DNA could not be taken due to formation of the red precipitate. Therefore, the mixture was allowed to continue reacting at room temperature for 24 hours. After the Cu^{2+} was reduced, the red precipitate (Cu_2O-DNA) was filtered, washed with ethanol and dried. The Cu_2O-DNA powder was then dissolved in DMF for the optical absorption measurements.

6.3.3 X-ray diffraction (XRD)

The XRD analysis was recorded from a powder sample using the XRD system (XPERT-PRO) with graphite monochromatized $Cu_{K\beta}$ radiation ($\lambda = 0.15418$ nm). The scanning rate of 0.03°/s was applied to record the pattern in the 2θ range of 30° to 70°. For XRD measurements about 1 mL CT-DNA solution (162.5 μg/mL; 10 mM Tris-HCl pH 8 +1 mM EDTA) were mixed with 1 mL freshly prepared Benedict's solution. Then ascorbic acid (0.2 M) was added dropwise to the solution (approx 0.5 mL). A red Cu_2O-DNA precipitate was formed. A large amount (approx 100 mg) of the Cu_2O-

DNA powder was prepared and collected using the same procedures described before for XRD analysis.

6.3.4 X-ray photoelectron spectroscopy (XPS)

An Axis-Ultra photoelectron spectrometer equipped with a monochromic Al-Kα X-ray as the excitation source (1486.7eV) with an operating power of 150 W (15 kV, 10 mA) was used to collect photoemission spectra of Cu_2O-DNA sample. The photoelectrons induced by the X-ray excitation were filtered by the hemispherical analyzer, and recorded by multi-channel detectors at a chamber pressure of 3.2×10^{-9} Torr. For the survey scan, the pass energy was 20 eV and the step size was 0.3 eV. The binding energies obtained in the XPS analysis were corrected for surface charging effect (0.5 eV), using C_{1s} (284.6 eV) as a reference. Peaks of the sample were fitted with Doniach Sunjic doublet functions after subtraction of a linear background using the WinSpec programme developed by LISE laboratory, Belgium. The Cu_2O-DNA sample was prepared by depositing 3 μL of solution on a clean Si (100) substrate and then left to dry in air at room temperature in a laminar flow hood to reduce contamination (Envair Limited; 0.6 m/s air flow and 60 rpm fan speed) before being inserted into the XPS chamber.

6.3.5 AFM and EFM investigations

Tapping Mode AFM imaging of surface topography was performed in air on a Dimension Nanoscope V using TESP probes (n-doped Si cantilever), with a resonant frequency of 234-287 kHz. The surfaces of substrates used were cleaned using the method described in chapter 2.

EFM measurements were also carried out in air on a Dimension Nanoscope V system using MESP probes (n-doped Si cantilevers, with a metallic Co/Cr coating), with a resonant frequency of ca. 70 kHz and a quality factor of 200-260. For both AFM systems, vibrational noise was reduced with an isolation table/acoustic enclosure.

In EFM experiments, an electrostatic field is created between the tip and sample by applying an independently controlled bias to the sample, while the tip was grounded. The phase shift is related to the force gradient and is sensitive to the conductance of Cu_2O-DNA nanowires under examination. The EFM phase images show the phase of

the tip oscillation at a set lift height above the sample surface. Samples used in EFM studies were aligned upon Si(100) substrates with a thermally grown oxide layer, ~210 nm thick on top. Processing of data acquired from AFM and EFM experiments was carried out using Nanoscope version 7.00b19 (Veeco Inc., Digital Instruments).

As discussed before in chapter 2, if a nonconductive, but polarizable nanowire is modelled as a thin dielectric strip lying directly under the tip (modelled as a disk of defined radius, R_{tip}), the phase shift can be estimated by equation (2.15). Where Q is the quality factor, k is the cantilever spring constant, *t* is the oxide thickness, and *d* the nanowire diameter. Inspection of equation (2.13) shows that the polarizability of an insulating 1D structure alone can only provide a positive phase shift. However, for conducting nanowires, which allow the charge stored on the Cu_2O-DNA nanowire/Si capacitor to be spread along the length of the wire (L), the second term in equation (2.15), becomes significantly larger (as the length of the capacitor nanowire/substrate is now determined by l rather than by R_{tip}), resulting in a negative phase shift.

For C-AFM measurements, a constant bias was also applied between the tip and the Cu_2O-DNA nanowires (the tip was grounded). Electrical contact was made by applying a drop of In/Ga eutectic to one corner of the chip and to the metallic chuck. The closed loop system of the Dimension V instrument makes possible to reproducibly position the cantilever at a point of interest on the nanowire and record the I-V curve.

6.4 Results and discussion

6.4.1 Chemical synthesis of Cu_2O in DNA-containing solutions

In this study, λ-DNA was also used as a template to direct Cu_2O nanowire assembly. The method reported here is simple and reproducible; the reaction conditions are mild and the reactants need no heating in the experiment. Cu_2O nanowires were formed upon λ-DNA template by chemical reduction of an alkaline cupric citrate complex solution (Benedict's reagent) using ascorbic acid as the reducing agent, in air and at room temperature. Cu^{2+} ions are attached electrostatically to DNA, then reduced to Cu_2O with ascorbic acid.

DNA possesses two possible binding sites; anionic phosphate groups and aromatic bases, which play an important rule in the DNA templating method (non-covalent

interaction) [22]. Here, the Cu^{2+} cations attach electrostatically to the anionic DNA backbone with the intimate interactions between Cu_2O and DNA in the resulting nanowires, confirmed by means of FTIR, UV-Vis, XRD, XPS and AFM. Variations of the synthesis process, described here, may also be valuable for the synthesis of other nanomaterial oxides with significantly higher efficiency.

6.4.2 Fourier transform infrared spectroscopy investigation

FTIR spectra were used to characterize the interaction of Benedict's reagent and λ-DNA. The infrared spectral features related to this discussion are presented in Figure 6.1. The free λ-DNA spectrum (dotted line) shows the characteristic in-plane vibrations of bare DNA; 1118 cm^{-1} (PO_2^- symmetric stretch), 1232 cm^{-1} (PO_2^- asymmetric stretch), 1408 cm^{-1} (C-N stretch thymine, adenine), 1490 cm^{-1} (C8-N coupled with a ring vibration of guanine), 1556 cm^{-1} (in-plane vibrations of cytosine and guanine) and 1658 cm^{-1} (purine stretch, N7)[92]. Cu_2O-DNA spectrum (solid line) shows distinct changes in several λ-DNA vibrational bands; a split band arising from PO^{2-} symmetric stretches (1128 cm^{-1}) and P-O or C-O stretches (1080 cm^{-1}) of the phosphate backbone. A shoulder band is also observed around 1157 cm^{-1} assigned to the asymmetric (O-C-C) dehydroascorbic acid. Moreover, the asymmetric PO_2^- vibration (1232 cm^{-1}) is also observed to be shifted to higher vibrational frequency (1246 cm^{-1}). This observation indicates the direct interaction between Cu species and DNA phosphate backbone.

Furthermore, the strong interaction between Cu_2O and DNA molecules derive from the fact that the DNA backbone is negatively charged, while as-formed Cu_2O is positively charged due to a small stoichiometric excess of Cu^{2+}. Therefore, the particles can be effectively adsorbed onto the DNA molecules via strong electrostatic interactions [128]. The presence of Cu_2O, is confirmed by the characteristic phonon band around 618 cm^{-1} [129] which was observed in the FTIR spectrum. Since Cu_2O-DNA nanowires were prepared from an aqueous DNA solution and Cu^{2+} citrate complex with ascorbic acid; the two strong bands at 1595 and 1398 cm^{-1} can be assigned to asymmetric and symmetric stretching of C=O of the carboxylate group [130] of citrate anion respectively.

In summary, the FTIR results indicate that the vibrational frequencies of λ-DNA are markedly altered upon interaction with the Cu^{2+}, which is evidence of close association

of the inorganic material and the DNA. The observation of the characteristic sharp feature at 618 cm^{-1} also demonstrates that the cupric ion is reduced to cuprous oxide rather than to metallic copper.

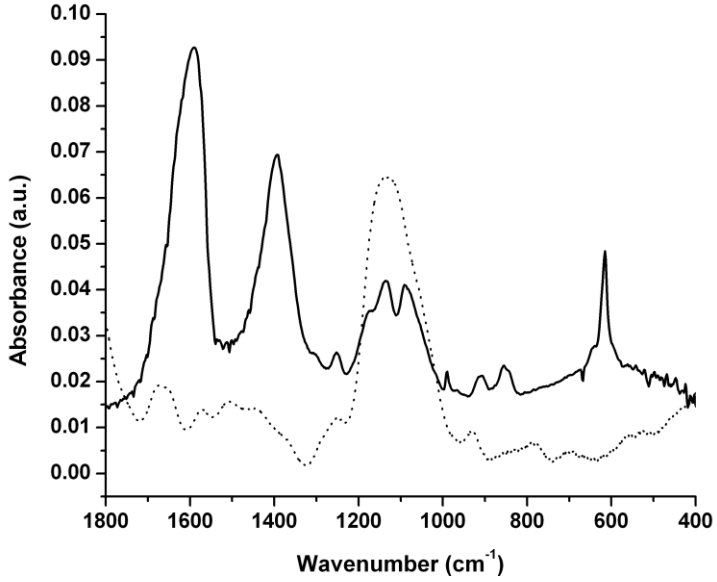

Figure 6.1. FTIR spectrum of Cu_2O nanoparticles upon DNA templates prepared using Benedict's reagent and ascorbic acid (solid line); the Cu_2O nanostructures exhibit a distinct band around 618 cm^{-1}. The FTIR spectrum of bare λ-DNA (dotted line)

6.4.3 UV-Vis absorption spectroscopy

It has previously been reported that the optical absorption of Cu_2O nanoparticles can be affected by its morphology and crystallinity [130, 132]. In this study, the UV-Vis absorption results of bare CT-DNA solution, Benedict's reagent and Cu_2O-DNA powder in DMF were recorded at room temperature (Figure 6.2). The electronic UV-Vis spectrum of the bare CT-DNA solution (dotted line) exhibits the distinct characteristic absorption band of DNA at 260 nm; this peak has shifted toward longer wavelengths (280 nm) indicating that DNA has a strong interaction with Cu species.

The UV-Vis spectrum of Benedict solution shown in Figure 6.2 (dashed line) suggests that the Cu^{2+} citrate complex shows a weak broad absorption in the 600–800 nm range, which vanished upon the addition of the ascorbic acid, indicating the reduction of Cu^{2+}. Moreover, Cu_2O-DNA spectrum (solid line) displays an absorption peak located at 400 nm, which can be attributed to Cu_2O nanocrystals. This absorption also showed an obvious blue shift compared to the absorption at 570 nm of bulk Cu_2O [131].

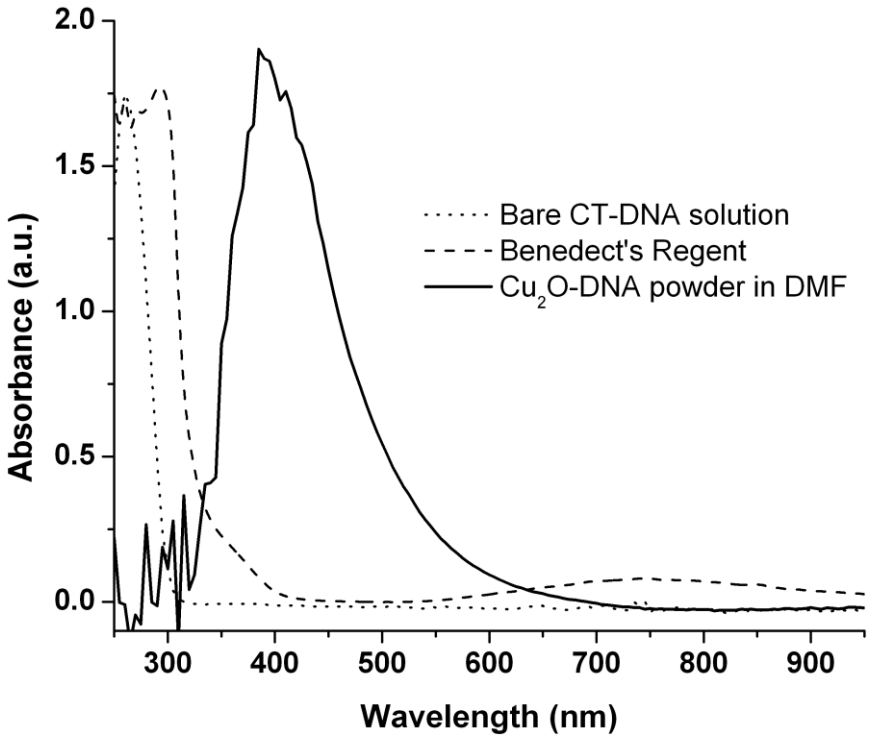

Figure 6.2: UV-Vis absorption spectra of Cu_2O powder prepared in solutions containing CT-DNA, Benedict's solution and ascorbic acid at room temperature. The UV-Vis spectrum of bare CT-DNA solution (dotted) exhibiting an absorption band at 260 nm; the UV-Vis spectrum of Benedict's solution (dashed line) showing broad absorption in the range 600–800 nm, which vanished with the addition of the ascorbic acid, and the UV-Vis spectrum of Cu_2O-DNA powder in DMF (solid) displaying an absorption peak located at about 400 nm, which can be attributed to the presence of Cu_2O nanocrystals

6.4.4 X-ray diffraction (XRD)

X-ray diffraction (XRD) spectroscopy has been used to characterize the Cu species in the Cu_2O-DNA. Figure 6.3 shows the XRD patterns of the Cu_2O from the Cu_2O-DNA powder. The XRD spectrum contains four clear peaks; all of which can be indexed to Cu_2O nanostructures and there are no features due to metallic Cu in the sample. The diffraction peaks at 2θ values 36.1°, 42.3°, 51.1° and 61.3° correspond to the crystal planes of (111), (200), (211) and (220) respectively of crystalline Cu_2O according to the International Centre of Diffraction Data (ICDD). The peak positions are in good agreement with those reported for nano-sized Cu_2O [132, 133]. The average size of the nanocrystals was estimated using the Scherrer formula [36] from the full width at half maxima (FWHM) of the diffraction peaks 36.1°, 42.3°and 46.7°, as can be seen in (Table 6.1) in nm. It may be noted that there is reasonable agreement between Scherrer sizes and the nanocrystals sizes estimated by AFM.

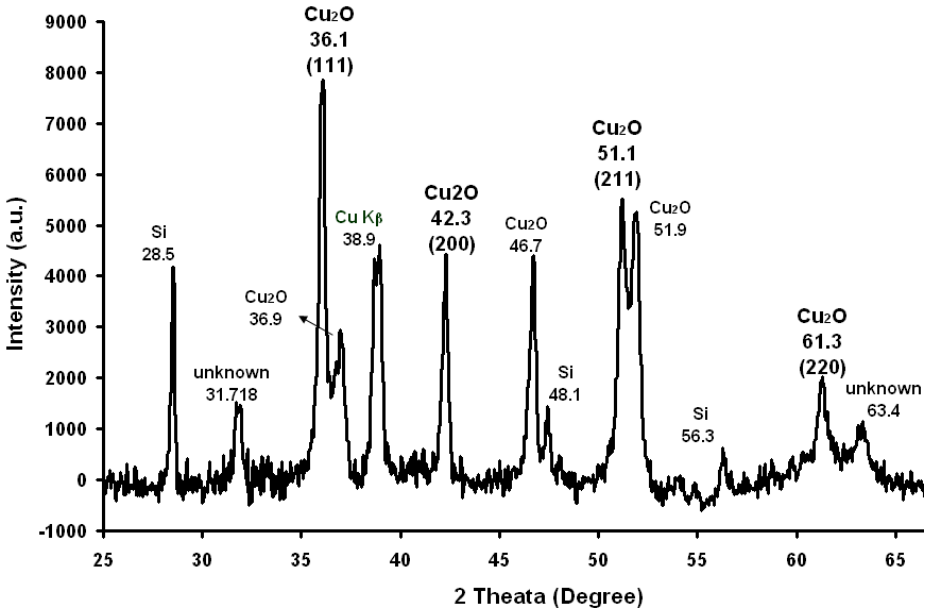

Figure 6.3. XRD pattern of Cu_2O powder prepared in solutions containing CT-DNA, Benedict's solution and ascorbic acid showing the peaks arising from the Cu_2O (111), (200), (211) and (220) reflections[134]. Other peaks arise from unknown contaminants. Unknown peaks could be due to salt contaminations

The diffraction peak at 2θ=38.9° arises from the Cu K_β (radiation source) not the sample itself because none of the well-known Bragg peaks of metallic Cu are present, e.g. at 43 degrees. Also, Si substrate diffraction peaks were observed at 2θ=46.8° to 48.1° and at 56.3°, while a few unassigned peaks emerged, likely due to buffer salts. It should be noted that XRD was carried out on a sample prepared from CT-DNA, which is available in larger quantities than the λ-DNA used for AFM. The particle diameter of Cu_2O on these two forms of DNA was found to be slightly different; however it is not possible to obtain XRD patterns from the small quantities of material prepared from λ -DNA. Nevertheless, correlation of the FTIR and UV-Vis spectral results with those derived from the XRD analysis confirms the sample composition as Cu_2O/DNA.

Table 6.1: Average Cu_2O nanoparticles size estimated by AFM and Scherrer equation

Angle (deg)	Average nanoparticles diameter estimated from AFM (nm)	Nanoparticles diameter calculated from Scherrer equation (nm)
36.1	14.1±0.4	13.1±1.3
42.3		12.0±1.2
46.7		10.3±1.8

6.4.5 X-ray photoelectron spectroscopy (XPS)

X-ray photoelectron spectroscopy (XPS), which is very sensitive to the oxidation state of copper (e.g., Cu^{2+}, Cu^{+} and Cu^{0}), has been used to study the composition of the Cu_2O-DNA surface sample. Synthesis methods, surface state, size and other factors affect the physical properties of Cu_2O nanoparticles, which are not defined obviously as in the case of bulk materials [135]. Fitting the XPS Cu_{2p} spectrum reveals that two peaks located at 932.54 and 953.66 eV respectively can be assigned to the binding energy of $Cu_{2p3/2}$ and $Cu_{2p1/2}$ (Figure 6.4) , which is in a good agreement with data previously reported for Cu_2O nanowires [136]. The binding energies are calculated with reference to C_{1s} binding energy 284.6 eV to compensate the charging effect. The spectrum between 920 and 965 eV indicates a doublet with a peak separation of 21.1 eV owing to the presence of the Cu^{+} state. Further observation of the O_{1s} region of the spectrum shows a binding energy of 530.1 eV, which corresponds to O^{2-} in Cu_2O, consistent with the value reported in the literature [121].

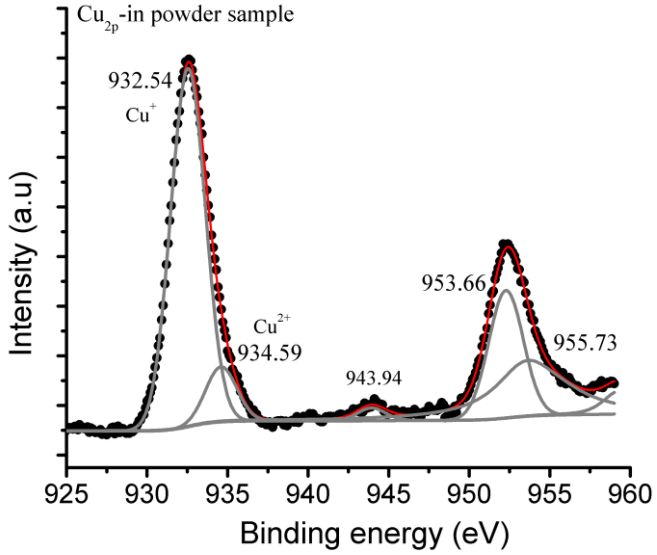

Figure 6.4: XPS spectrum of Cu_2O-DNA nanowires sample. $Cu_{2p3/2}$ and $Cu_{2p1/2}$ appear at 932.54 and 953.66 eV respectively, which can be attributed to the Cu_2O nanostructures.

On the other hand, only a weak satellite feature around 942-944 eV on the higher binding energy side of the Cu_{2p} main peak was observed , which could be due to traces of CuO on the surface of the nanocrystals. It should be noted that the divalent copper compounds show characteristic shake-up satellite peaks on the higher binding energy side of the spectrum [137]. In summary, the XPS results together with XRD suggest

the formation of Cu_2O core structure with perhaps a thin CuO shell upon DNA templates.

6.4.6 Cu_2O-DNA nanowires assembly: AFM characterization

Tapping mode AFM was used to record the morphology of the Cu_2O-DNA nanowires. As discussed before, this mode of AFM uses a probe, which taps the sample surface softly, with the tip oscillating close by its resonant frequency. The cantilever's oscillation amplitude and phase (with respect to the driving force) changes with nanowire surface topography and the image is achieved by monitoring these changes. Imaging of Cu_2O-DNA nanowires in the tapping mode is unlikely to cause damage, because the lateral forces in this mode are reduced in comparison to C-AFM mode. Different AFM images of the nanowires were recorded over different incubation times and different scan sizes. Figure 6.5 (b) shows AFM tapping images of nanowires aligned on Si substrate after two hours of preparation. It depicts many individual DNA molecules with individual Cu_2O nanoparticles in the background that do not nucleate on the DNA template. The AFM image shown in Figure 6.5(a) indicates that a short incubation time (less than 60 minutes) led to Cu_2O nanoparticles not being fully templated on the DNA molecules, and did not form a complete Cu_2O-DNA nanowire. It was noticed that, if the incubation time is shorter than one hour, most of the Cu_2O nanoparticles in the solution did not have the chance to interact completely with the DNA to form a complete Cu_2O-DNA nanowire; instead, a beads-on-string appearance is observed. Figure 6.5 (b) shows the AFM image of Cu_2O nanoparticles assembled along λ-DNA strands to form continuous nanowires aligned on substrate after 2 hours of incubation. Lengths of aligned nanowires ranged from about 2 μm to 16 μm. The AFM image shows that the diameter of bare λ-DNA aligned on the substrate surface, which was about 1 nm is consistent with previous measurements of double-stranded DNA recorded by AFM [34]. The height observed for individual untemplated Cu_2O nanoparticles ranged from 2.7 to 4.5 nm with standard deviation $\sigma = 0.54$, and average = 3.5 nm, while heights of Cu_2O nanoparticles assembled onto DNA chains were in the range, 15–24 nm with standard deviation $\sigma = 2.4$, and 20 nm average. The grains seen about 2.8 nm in height possibly enclose more than one nanoparticle of Cu_2O. Figure 6.5 (b) shows that Cu_2O nanoparticles are assembled and embedded onto the DNA chains, but there are few nanoparticles surrounding the nanowire.

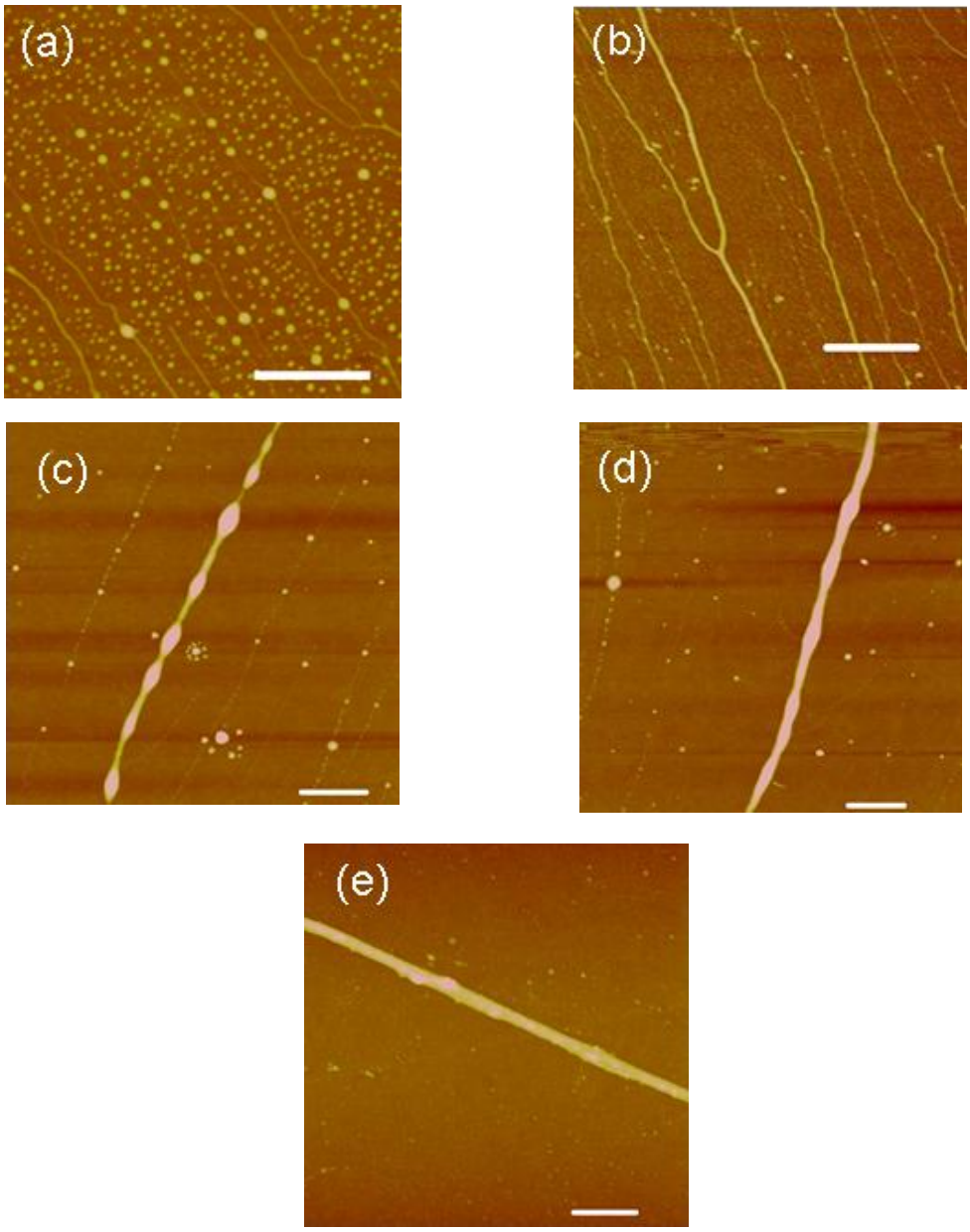

Figure 6.5 AFM images of Cu_2O-DNA nanowires aligned on substrate at different incubation times; a) < 60 min., height scale 25 nm. b) 2 h, height scale 25 nm, c) after 45 days, height scale 30 nm; d) after 53 days, height scale 30 nm; (e) after 210 days, height scale 30 nm. Scale bar 1 μm in all AFM images

It was noticed that within 45 to 53 days DNA strands can undergo a transformation from bead-on-string appearance (Figure 6.5 c and d) to continuous nanowires (Figure 6.5 e) with an aggregation of Cu_2O nanoparticles that is most evident as a morphological change in the strand structure.

The interaction between Cu_2O nanoparticles and negatively charged DNA molecules at that part of the DNA may be weak preventing the Cu_2O from being adsorbed onto it. In addition, a substrate surface highly treated with Me_3SiCl prevents the positively charged Cu_2O nanoparticles from adsorbing to the surface. Moreover, the nanoparticles may not be able to fully assemble onto the DNA templates in a short incubation time. In short, The Cu_2O nanoparticles incubated in the solution containing DNA for different periods of time, in many cases, produce nanoparticles aggregation upon the DNA strands. Whereas, incubation for longer time produce nanoparticles adsorbed onto the DNA molecules exhibiting a beads-on-a-chain morphology as seen by AFM. After very long incubation time, the beads-on-chain morphology starts to disappear and smoother nanowires are observed on the substrate surface.

6.4.7 Electrical characterisation of Cu_2O-DNA nanowires by scanned conductance microscopy (SCM)

As described before, EFM is a form of scanning probe microscopy in which a conductive probe is electrically biased with respect to the sample. This mode is used to measure the electric field gradient distribution above the Cu_2O-DNA nanowire's surface while DC bias is applied between the substrate holding nanowires and the tip, and the measurement is performed via lift mode and two-pass technique. As mentioned in chapter 2, section 2.8, previous results have indicated that conducting 1D structures, like single-wall carbon nanotubes have a negative phase shift, with respect to the background (SiO_2). In contrast, insulating materials show a positive phase shift. Therefore, the electrical conductivity of the Cu_2O-DNA nanowire was tested by EFM as an effective tool to trace its conductivity. A negative-positive-negative phase variation was observed as the tip crossed the Cu_2O-DNA nanowires; this behaviour has been reported before in chapter 3 for conductive polymer nanowires. It is consistent with the absence of significant metallic copper in our Cu_2O-DNA nanowires, which would be expected to give a simple negative phase shift. Upon varying the applied bias and measuring the phase shift at the most negative point, the expected parabolic dependence of phase shift on bias for voltages between -6V and +6V was observed (Figure 6.6 a). The corresponding EFM image is presented in Figure 6.6 (b) (applied bias V= 6V, lift height 50 nm). In all EFM phase images, Cu_2O-DNA nanowires appear as dark lines with a brighter central portion.

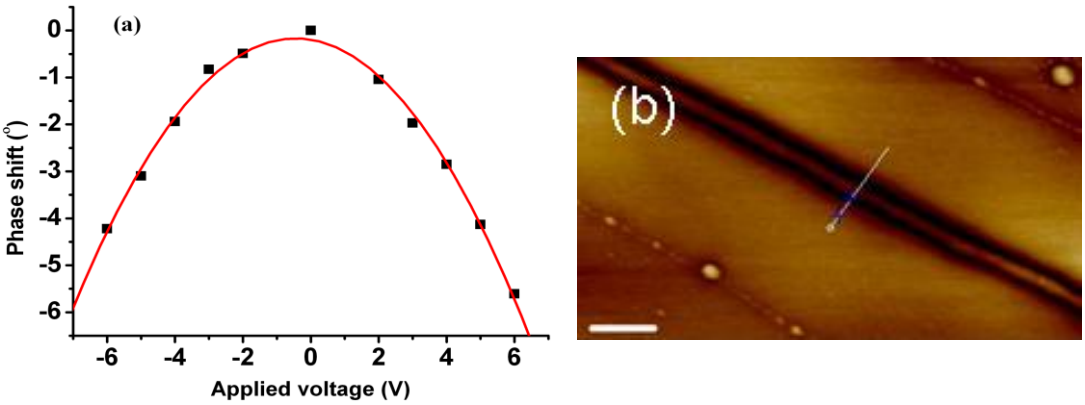

Figure 6.6: a) EFM phase shift as a function of bias voltage of Cu_2O-DNA nanowire. Lift height 50 nm, b) corresponding EFM images (applied bias V= 6V, lift height 50 nm, data scale 10°), scale bar 200 nm where the nanowire (>2 h incubation time) appears as a dark line

6.4.8 Conductive AFM and direct current–voltage characterization

Conductive AFM (C-AFM) techniques hold great promise in nanotechnology applications for providing direct electrical characterization, in addition to surface topography. C-AFM images are generally acquired in contact mode, with metal(Co/Cr)-coated cantilevers. In these C-AFM experiments, networks of Cu_2O-DNA nanowires were deposited upon a thick SiO_2 insulating layer (220 nm) grown on Si substrate, with a eutectic (Ga/In) paste contact connecting the wires to the metallic chuck (Figure 6.7). The metal coated tip was then used to act as the second electrical contact. The imaged area was about 1 mm away from the eutectic contact. When scanning individual nanowire in contact mode, the tip disturbs and moves the nanowire during scanning. For this reason, a network of nanowires was used, instead of a single one, to eliminate this effect.

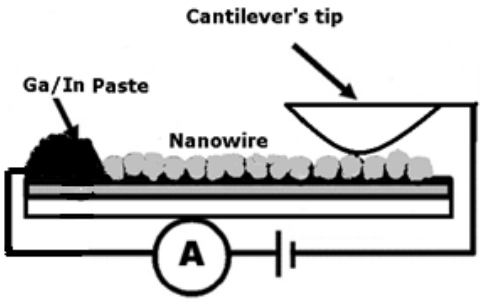

Figure 6.7: Schematic representation of C-AFM arrangement setup[106]

I-V curves obtained from AFM in a conductive mode are shown in Figure 6.8. These curves were repeated for different DC sample biases to ensure that these curves are

producible at room temperature. A symmetric linear behaviour was observed. The electrical resistance of prepared nanowires varied in the range from 0.13 to 0.18 MΩ under different deflection setpoints and at room temperature. The electrical resistance decreased slightly with increasing the vertical contact force (deflection setpoints) due to decreasing the contact resistance between the nanowire and the cantilevers' tip. However this effect is quite small and indicates that tip/sample contact resistance is not so significant for the Cu_2O/DNA nanowires. A breakdown voltage is observed at about -10 V and turn-on voltage at about 10 V for the reverse and forward bias consequently.

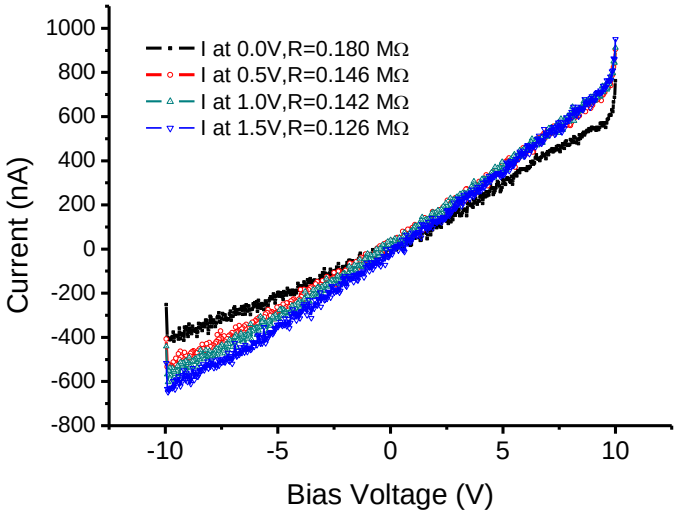

Figure 6.8: C-AFM I-V curves of Cu_2O-DNA with an applied DC sample bias of 5V; the electrical resistivity of the prepared nanowires ranged from 0.13 to 0.180 MΩ under different deflection setpoints (1.5, 1.0, 0.5, and 0.0 V) at room temperature

6.5 Conclusions

In conclusion, it has been shown that DNA molecules can be used as templates for the growth of Cu_2O nanoparticles to form conductive nanowires. Cu_2O nanowires were synthesized on DNA templates using Benedict's reagent and ascorbic acid via a one-step in-situ chemical reduction process. The templating interaction (non-covalent) has been afforded by cationic Cu_2O nanoparticles, which attached electrostatically to the anionic DNA backbone via a self-assembly process. The X-ray photoelectron spectroscopy and X-ray diffraction measurements on the synthesised nanowires mainly showed Cu_2O with a small amount of CuO also present. The morphology of the nanostructured Cu_2O material has also been observed by AFM, showing the nanowire becomes continuous at longer incubation times. Electrical characterisation of the

structures has been investigated by C-AFM exhibiting the electrical resistance in the range from 0.13 to 0.180 MΩ under different deflection setpoints. Prior to use of these nanowires in DNA-based nanoelectronic devices, the author recommends further investigations of their conductivity, especially the variation with temperature using the two-terminal method to investigate the nature of the conduction mechanism.

Chapter 7: Overall Conclusion and Future Work

7.1 Achievements

In this thesis, different conductive nanowires templated by DNA were fabricated and their physical characteristics investigated using different methods. This work is necessary to provide the basis for simple nanowire devices, as a forerunner of more complicated use of nanowires in IC circuits. Test systems were also constructed by the fabrication of Au electrodes using conventional photolithography that act as an interface between the nanoworld (nanowires) and the microworld (microelectrodes). This step in this work was vital to investigate the nanowire conductivity by providing a route to performing detailed electrical measurements of the nanowires. The study was also conducted with the aim of developing increased understanding of the mechanism of charge transport in nanowires. Moreover, this work will help in developing new methods and techniques for conductive nanowire fabrication. These protocols are used to provide greater understanding of the fabricated nanowire characteristics. Fabricated nanowires, in this work, may fulfil the demands for interconnects that can be used in current microdevices chips, as well as future nanodevices. In addition, it may help in finding new ways to reduce the cost and ease the difficulties now facing the semiconductor industry in the methods being used to fabricate nanostructures.

In chapter 3, it is shown that PPy can be templated on λ-DNA molecules to form conductive nanowires; this is demonstrated by two-terminal current–voltage measurements, EFM (as an indirect measurement method) and C-AFM measurements on individual nanowires. Over longer periods of time, a self-assembly process occurs in which conductive polymer/DNA nanowires form rope-like structures (nanoropes). AFM studies show that the assembly process consists of individual wires twisting around each other. In this chapter, it is shown that the conductivity of PPy-DNA nanowires increases exponentially as the temperature increases from room temperature to 380K. Such behaviour can be interpreted in terms of a simple nearest-neighbour hopping model. At temperatures above 380 K the curve starts to deviate from the exponential (Arrhenius) behaviour. In addition, nanowire conductivity was measured over one cycle of heating up and cooling down, and showed relatively good stability with changing temperature.

In chapter 4, the formation of Ag nanostructures on the DNA template using Tollens' reagent was investigated by means of UV-Vis absorption spectroscopy and FTIR spectroscopy. Furthermore AFM, XRD and XPS showed that these structures are best viewed as metallic Ag coated with Ag_2O. The AFM studies revealed that the DNA-templated Ag nanowires formed were very rough. The electrical measurements obtained from Ag-DNA nanowires using EFM and C-AFM showed that these nanowires are conductive. The two-terminal technique used to investigate the conductivity of these nanowires bridging two Au electrodes and the temperature dependent measurements showed that these nanowires do not act as metallic conductors, rather they behave like hopping conductors in the manner their conductance increases with temperature; this is consistent with the picture derived from the XRD and XPS data.

Chapter 5 showed that the metal-binding functionality (alkynyl group) can be introduced into DNA-templated polymer nanowires by chemical modification of the TP, and can be used to improve the morphology of Ag nanoparticles deposited on this hybrid template.

Chapter 6 discussed the investigation of electrically conductive Cu_2O nanowires templated by DNA using an alkaline copper citrate complex solution (Benedict's reagent) and ascorbic acid as reducing agent in air and at room temperature. The advantage of this method lies in its simplicity and mild reaction conditions, as well as short synthesis time. AFM imaging showed that the Cu_2O-DNA nanowires are smoother than Ag-DNA nanowires. Formation of Cu_2O-DNA nanowires were characterized by FTIR spectroscopy, UV-Vis, AFM, XRD and XPS, while conductivity was investigated by C-AFM. Aside from the preparation and characterisation of new nanomaterials, distinctive contributions were made to the methods for measuring electrical properties of nanowires. A simple technique employing C-AFM was developed to assess the contribution of contact resistance to the measured resistance. In this method, the closed-loop positioning system of the AFM was employed to place the tip at particular points along a nanowire and to record I-V curves at these points. The zero-bias conductance at these points depends on the tip/wire contact resistance as well as the length of the nanowire between the tip and a remote second contact. By varying the position of the tip, the length of the nanowire through which the current passes is varied, but the contact resistance does not vary

systematically. A plot of measured resistance against distance shows a linear behaviour with an intercept at zero relative distance that is an estimate of the contact resistance. Using this technique, it was established that the lower conductances measured for polymer/DNA nanowires than metal-templated or other inorganic materials (Cu_2O) on DNA are due to the resistance of the polymer wires rather than any difficulty in making contact to them.

Two-terminal I-V measurements upon single nanowires have been also demonstrated using a combination of spin coating and molecular combing to align the nanowires, which facilitated the I-V measurements over a range of temperatures. These measurements showed that the conductance of all prepared nanowires increases as the temperature increases. From the ohmic part of the I-V curve, the conductance was calculated and the temperature dependence of the conductance followed an Arrhenius' behaviour. The simplest interpretation consistent with the experimental data is a nearest neighbour hopping model.

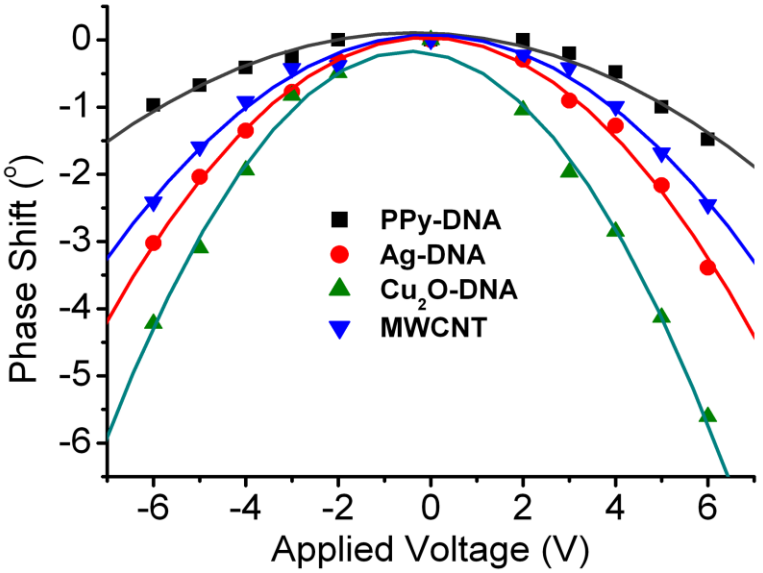

Figure 7.1: EFM phase shift comparison between MWCNT and nanowire samples fabricated.

EFM (also known as scanned conductance microscopy) was developed to provide a rapid and convenient non-contact method for determination of conductance and conducting pathways. At present, it is not possible to use this technique to extract quantitative values of conductance, but it was found to be a very powerful technique to detect conducting objects prior to more difficult experiments being carried out that

require contacts to be prepared. It was also shown that, the effect is in principle sensitive to the material; this is a novel finding because existing theory deals only with the perfect insulator and perfect conductor limits.

A comparison of conductivities between different samples fabricated in this work and multiwall carbon nanotube (MWCNT) using EFM can be shown in Figure 7.1. Cu_2O-DNA nanowires show higher phase shift than PPy-DNA, Ag-DNA nanowires and MWCNT nanowires. All compared nanowires have approximately the same length (~1 μm) and diameter (20-24 nm). These differences in nanowires of the same dimensions show that the EFM method is sensitive to conductance; an observation that cannot be accommodated in the existing theory; further work is however needed to develop the technique to make this experiment quantitative.

Finally, it is worth considering the performance of polymer/DNA nanowires compared to traditional materials. Silicon nanowires can exhibit lower resistivity (measured values span the range 2.6 $x10^{2}$ Ω cm to 2.3$x10^{-2}$ Ω cm, depending on doping level [138]) than most polymer nanowires. However, conducting polymer-DNA nanowires and to some extent Ag or Cu_2O nanowires templated on DNA also have several advantages compared to silicon nanowires. First, they have attractive mechanical properties and processing advantages of polymers while exhibiting useful electrical properties. Second, by controlling the oxidation level of theses nanowires their conductivity can be controlled from the insulating to the semiconducting. Third, they are low-cost, elastic and stable in air. Fourth, they can be synthesized easily by chemical methods at room temperature. Fifth, polymerization can be carried out from aqueous environment in ambient environment, producing one-step synthesis of nanowires templated by DNA. Sixth, the advantage of using DNA as a template is that it is a chemically robust material, which can be obtained in high purity. Seventh, single molecules of DNA of many micrometres long are available and DNA composition and structure are well defined. Finally, polymers are easier to chemically change in order to introduce functionality for the preparation of, for example, sensing elements. This can be done very easily by altering the chemical nature of the monomer through organic synthesis and was demonstrated here by using monomers bearing metal-complexing groups (alkynyl) to aid in the formation of metal/polymer hybrid nanowires.

7.2 Further work

In the conclusion of this research, areas for further investigation on the fabricated nanowires have been identified. These include using more techniques, such as scanning tunnelling microscopy (STM), magnetic field microscopy (MFM), tunnelling atomic force microscope (TUNA) and torsion resonance tunneling atomic force microscopy (TR-TUNA) to increase the data available. MFM can be used to study the ferroelectric and magnetic response of the synthesised nanowires, and the possibility of using it as a storage element for memory devices. On the other hand, TR-TUNA can be utilised to examine the conductivity of nanowires in a further investigation of current transport in nanowires with low conductivity, where non-destructive current mapping technique of the nanowires is possible because the torsional resonance mode has characteristics similar to tapping mode and will disturb the sample less than conventional contact C-AFM. Such a study will provide further support for the C-AFM measurements already done on these nanowires, and a further shed light on the effect of contact resistance on the conductivity of PPy and metal-DNA nanowires. A suggested area of future work involves using the two-terminal technique and applying a high current density continually through nanowire for a given time, and monitoring changes in the nanowire. Moreover, the four-point probe method would be a useful tool to further examine the electrical properties of these nanowires, and is expected to provide valuable information about carrier transport in these nanowires.

In addition, it has been shown that conducting materials exhibit an EFM negative phase shift, while insulating materials exhibit a positive phase shift. Semiconductor materials, for example polyaniline/poly(ethylene oxide) fibres with nanometre size showed a negative-positive-negative phase shift as the tip scanned across. Using simple geometric models discussed in chapter 2, the phase shift was calculated for conductive $(R \to 0)$ and insulating $(R \to \infty)$ nanowires. However it is not yet possible to use EFM to measure the value of the resistance of an individual nanowire. It would be interesting to extend the current theoretical models to show how the EFM experiment responds to arbitrary, finite values of *R*. This will be useful in demonstrating the utility of the EFM technique for tracing conductive pathways in nanoscale systems. Such a study is expected to show the effect of nanowire resistance

on the EFM phase images, and suggest ways that may allow quantitative extraction of conductance data from the EFM images.

Finally, the electrical conductivity of Cu_2O-DNA nanowires at various temperatures is now under further investigation. Also, the author suggests further studies on the possibility of using these nanowires as sensors and additional study of Ag/polymer/DNA nanowires conductivity using the two-terminal method.

Appendix A: Published and Pending work

Articles published prior to the submission time can be found at the end of this thesis and the manuscript of the pending articles shown in the list giving below have been prepared and will be published soon.

i. List of published articles

a. Al-Said, S. A., Pruneanu, S., Nicholas G. W., Houlton, A. and Horrocks , B. R., *Templating Ag on DNA/polymer hybrid nanowires: Control of the metal growth morphology using functional monomers*. Electrochemistry Communications, 2009. 11(3): p. 550-553.

b. Pruneanu, L., O. Al-Said, S. A., G. Borodi, A. Houlton, and B. Horrocks, *Template and template-free preparation of one-dimensional metallic nanostructures*. Journal of Materials Science, 2010. 45(12): p. 3151-3159.

c. Pruneanu, S., Al-Said S. A., *et al*., *Self-Assembly of DNA-Templated Polypyrrole Nanowires: Spontaneous Formation of Conductive Nanoropes*. Advanced Functional Materials, 2008. 18(16): p. 2444-2454.

d. Reda, H., Mariam A., Al-Said, S. A., Nicholas G. Wright, Andrew Houlton and Benjamin R. Horrocks, *Synthesis and Characterization of Self-Assembled Polyindole Nanowires on DNA Template*, ACS NANO, 2010, (DOI: 10.1021/nn9014533).

e. Hannant, J., Hedley, J. H., Pate, J., Walli, A., Al-Said S. A., et al., *Modification of DNA-templated conductive polymer nanowires via click chemistry.* Chemical Communications. 46(32): p. 5870-5872. (Contributed the electreical characterizations part of the article)

ii. List of pending articles

a. Al-Said, S. A., Reda, H. ,Nicholas G. W., Houlton, A. and Horrocks , B. R., *Synthesis and Characterization of Ag-DNA Nanowires, ...*

b. Al-Said, S. A., Reda, H., Nicholas G. W., Houlton, A. and Horrocks, B. R., *Electrical Conductivity of PPy-DNA Nanoropes*. Journal of Applied Physics, ...

c. Al-Said, S. A., Reda, H. ,Nicholas G. W., Houlton, A. and Horrocks , B. R., *Synthesis and characterization of conductive DNA-templated Cu_2O/DNA nanowires*, .

d. Reda, H., Mariam A., Al-Said, S. A. ,Nicholas G. Wright, Andrew Houlton and Benjamin R. Horrocks, *Synthesis and Characterization of Self-Assembled palladium Nanowires on DNA Template*,…

References

1. Vieu, C., et al., *Electron beam lithography: resolution limits and applications.* Applied Surface Science, 2000. **164**(1-4): p. 111-117.
2. Deguchi, K., H. Namatsu, K. Komatsu, and A. Yoshikawa, *Effects of photoelectrons ejected from the substrate on patterning characteristics in x-ray lithography.* Journal of Vacuum Science & Technology B: Microelectronics and Nanometer Structures, 1987. **5**(2): p. 551-554.
3. Ogawa, T., K. Mochiji, Y. Soda, and T. Kimura, *Effects of secondary electrons from a silion substrate on SR X-ray lithography.* Japanese Journal of Applied Physics, Part 1: Regular Papers and Short Notes and Review Papers, 1989. **28**(10): p. 2070-2073.
4. Ieong, M., B. Doris, J. Kedzierski, K. Rim, and M. Yang, *Silicon Device Scaling to the Sub-10-nm Regime.* Science, 2004. **306**(5704): p. 2057-2060.
5. Li, L., R.R. Gattass, E. Gershgoren, H. Hwang, and J.T. Fourkas, *Achieving lambda/20 Resolution by One-Color Initiation and Deactivation of Polymerization.* Science, 2009. **324**(5929): p. 910-913.
6. Babudri, F., G.M. Farinola, and F. Naso, *Synthesis of conjugated oligomers and polymers: The organometallic way.* Journal of Materials Chemistry, 2004. **14**(1): p. 11-34.
7. Tat'yana, V.V. and N.E. Oleg, *Polypyrrole: a conducting polymer; its synthesis, properties and applications.* Russian Chemical Reviews, 1997. **66**(5): p. 443.
8. Burroughes, J.H., et al., *Light-emitting diodes based on conjugated polymers.* 1990. **347**(6293): p. 539-541.
9. Aleshin, A.N.A., *Polymer Nanofibers and Nanotubes: Charge Transport and Device Applications.* Advanced Materials, 2006. **18**(1): p. 17-27.
10. Gilles Horowitz, *Organic Field-Effect Transistors.* Advanced Materials, 1998. **10**(5): p. 365-377.
11. Ouyang, J., C.-W. Chu, C.R. Szmanda, L. Ma, and Y. Yang, *Programmable polymer thin film and non-volatile memory device.* Nature, 2004. **3**(12): p. 918-922.
12. Kwan, W.L., et al., *Direct observation of localized conduction pathways in photocross-linkable polymer memory.* Journal of Applied Physics, 2009. **105**(12): p. 124516.
13. Galatsis, K., et al., *Emerging memory devices.* Circuits and Devices Magazine, IEEE, 2006. **22**(3): p. 12-21.
14. Watson, J.D. and F.H.C. Crick, *Molecular structure of nucleic acids: A structure for deoxyribose nucleic acid.* Nature, 1953. **171**(4356): p. 737-738.
15. Bensimon, A., et al., *Alignment and sensitive detection of DNA by a moving interface.* Science, 1994. **265**(5181): p. 2096-2098.
16. Becerril, H.A. and A.T. Woolley, *DNA-templated nanofabrication.* Chemical Society reviews, 2009. **38**(2): p. 329-337.

17. Shih, W.C.a.G., A. L., *Electromigration damage and failure distributions in Al-4 wt % Cu interconnects.* J. Appl. Phys., 1998. **84**: p. 2551.

18. Braun, E., Y. Eichen, U. Sivan, and G. Ben-Yoseph, *DNA-templated assembly and electrode attachment of a conducting silver wire.* 1998. **391**(6669): p. 775-778.

19. Iqbal, S.M., G. Balasundaram, S. Ghosh, D.E. Bergstrom, and R. Bashir, *Direct current electrical characterization of ds-DNA in nanogap junctions.* Applied Physics Letters, 2005. **86**(15): p. 153901.

20. Yoichi Otsuka, H.-y.L., Jian-hua Gu, Jeong-O Lee, Kyung-Hwa Yoo, Hidekazu Tanaka, Hitoshi Tabata and Tomoji Kawai, *Influence of Humidity on the Electrical Conductivity of Synthesized DNA Film on Nanogap Electrode.* Jpn. J. Appl. Phys., 2002. **41**(891).

21. Skotheim, T.A., Elsenbaumer, R. L. and Reynolds, J. R. , *Handbook of Conducting Polymers*. 2nd ed. 1998: Marcel Dekker, New York.

22. Dong, L., Hollis, T. , Fishwick, S. , Connolly, B. A. , Wright, N. G. , Horrocks, B. R. , Houlton, A., *Synthesis, Manipulation and Conductivity of Supramolecular Polymer Nanowires.* Chemistry - A European Journal, 2007. **13**(3): p. 822-828.

23. Anastassopoulou, J., *Metal-DNA interactions*, in *Journal of Molecular Structure; Molecular Spectroscopy and Molecular Structure; Proceedings of the XXVIth European Congress on Molecular Spectroscopy, Villeneuve d'Ascq, France, September 1-6, 2002.* 2003. p. 19-26.

24. Keren, K., et al., *Sequence-Specific Molecular Lithography on Single DNA Molecules.* Science, 2002. **297**(5578): p. 72-75.

25. Richter, J., Seidel, R. , Kirsch, R. , M. Mertig, W. Pompe, J. Plaschke, H. K. Schackert, *Nanoscale Palladium Metallization of DNA.* Advanced Materials, 2000. **12**(7): p. 507-510.

26. Ford, W.E., O. Harnack, A. Yasuda, and J.M. Wessels, *Platinated DNA as Precursors to Templated Chains of Metal Nanoparticles.* Advanced Materials, 2001. **13**(23): p. 1793-1797.

27. Kudo, H. and M. Fujihira, *DNA-templated copper nanowire fabrication by a two-step process involving electroless metallization.* Nanotechnology, IEEE Transactions on, 2006. **5**(2): p. 90-92.

28. Dong, L., Hollis, T. , Connolly, B. A. , Wright, N. G. , Horrocks, B. R. , Houlton, A. , *DNA-Templated Semiconductor Nanoparticle Chains and Wires.* Advanced Materials, 2007. **19**(13): p. 1655-1662.

29. Dittmer, W.U. and F.C. Simmel, *Chains of semiconductor nanoparticles templated on DNA.* Applied Physics Letters, 2004. **85**(4): p. 633-635.

30. Houlton, A., A.R. Pike, M. Angel Galindo, and B.R. Horrocks, *DNA-based routes to semiconducting nanomaterials.* Chemical Communications, 2009(14): p. 1797-1806.

31. Kundu, S. and H. Liang, *Photochemical Synthesis of Electrically Conductive CdS Nanowires on DNA Scaffolds.* Advanced Materials, 2008. **20**(4): p. 826-831.

32. Vitali, S. and et al., *DNA-assisted formation of quasi-nanowires from fluorescent CdSe/ZnS nanocrystals.* Nanotechnology, 2006. **17**(2): p. 581.

33. Bensimon, D., A.J. Simon, V. Croquette, and A. Bensimon, *Stretching DNA with a Receding Meniscus: Experiments and Models.* Physical Review Letters, 1995. **74**(23): p. 4754 LP - 4757.

34. Yokota, H., J. Sunwoo, M. Sarikaya, G. van den Engh, and R. Aebersold, *Spin-Stretching of DNA and Protein Molecules for Detection by Fluorescence and Atomic Force Microscopy.* Analytical Chemistry, 1999. **71**(19): p. 4418 LP - 4422.

35. Smith, B.C., *fundamentals of Fourier transform Infrared: A Constantly evolving technology*. 1996, Boca Raton: CRC Press LLC.

36. Patterson, A.L., *The Scherrer Formula for X-Ray Particle Size Determination.* Physical Review, 1939. **56**(10): p. 978.

37. Kittel, C., *Introduction to solid state physics*. 7th ed. 1995, New York: John Wiley & sons Inc. .

38. Duckett, S.a.G., B., *Foundations of spectroscopy*. 2000, New York: Oxford Chemistry Primers.

39. Barnes, G.A., *Surface*. Vol. 1. 1998, New York: Oxford University Press.

40. Albrecht, T.R., P. Grutter, D. Horne, and D. Rugar, *Frequency modulation detection using high-Q cantilevers for enhanced force microscope sensitivity.* Journal of Applied Physics, 1991. **69**(2): p. 668-673.

41. Hassanien, R., Al-Hinai, M, Al-Said, Said A, Little, R, Siller, L, Wright, N G, Houlton, A, Horrocks, B R, *Preparation and Characterization of Conductive and Photoluminescent DNA-Templated Polyindole Nanowires.* ACS Nano, 2010. **4**(4): p. 2149–2159.

42. Ng, C.Y., Chen, T. P. , Lau, H. W. , Liu, Y. , Tse, M. S. , Tan, O. K., Lim, V. S. W. , *Visualizing charge transport in silicon nanocrystals embedded in SiO_2 films with electrostatic force microscopy.* Applied Physics Letters, 2004. **85**(14): p. 2941-2943.

43. Krauss, T.D., O'Brien, Stephen and Brus, Louis E., *Charge and Photoionization Properties of Single Semiconductor Nanocrystals.* The Journal of Physical Chemistry B, 2001. **105**(9): p. 1725-1733.

44. Bockrath, M., Markovic, N., Shepard, A., Tinkham, M., Gurevich, L., Kouwenhoven, L.P., Wu, M.W., Sohn, L.L., *Scanned Conductance Microscopy of Carbon Nanotubes and lamda-DNA.* Nano Lett., 2002. **2**(3): p. 187-190.

45. Gil, A., P.J.d. Pablo, J. Colchero, J. Gomez-Herrero, and A.M. Baro, *Electrostatic scanning force microscopy images of long molecules: single-walled carbon nanotubes and DNA.* Nanotechnology, 2002. **13**(3): p. 309-313.

46. Staii, C., A.T. Johnson, and N.J. Pinto, *Quantitative Analysis of Scanning Conductance Microscopy.* Nano Lett., 2004. **4**(5): p. 859-862.

47. Nishi, R., I. Houda, T. Aramata, Y. Sugawara, and S. Morita, *Phase change detection of attractive force gradient by using a quartz resonator in noncontact atomic force microscopy.* Applied Surface Science, 2000. **157**(4): p. 332-336.

48. Heeger, A.J., *Nobel Lecture: Semiconducting and metallic polymers: The fourth generation of polymeric materials.* Reviews of Modern Physics, 2001. **73**(3): p. 681 LP - 700.

49. Jernigan, J.C. and R.W. Murray, *Consequences of restricted ion mobility in electron transport through films of a polymeric osmium-polypyridine complex.* The Journal of Physical Chemistry, 1987. **91**(8): p. 2030-2032.

50. Dalton, E.F., et al., *Charge transport in electroactive polymers consisting of fixed molecular redox sites.* Chemical Physics, 1990. **141**(1): p. 143-157.

51. Nir, T., P. Yevgeni, R. Noam, and R. Yohai, *Charge Transport in Disordered Organic Materials and Its Relevance to Thin-Film Devices: A Tutorial Review.* Advanced Materials, 2009. **21**(27): p. 2741-2761.

52. Fernando P, Y.W., Oleg L, Itamar W, *Au-Nanoparticle Nanowires Based on DNA and Polylysine Templates.* Angewandte Chemie International Edition, 2002. **41**(13): p. 2323-2327.

53. Mertig, M., L. Colombi Ciacchi, R. Seidel, W. Pompe, and A. De Vita, *DNA as a Selective Metallization Template.* Nano Letters, 2002. **2**(8): p. 841-844.

54. Seidel, R., L. Colombi Ciacchi, M. Weigel, W. Pompe, and M. Mertig, *Synthesis of Platinum Cluster Chains on DNA Templates: Conditions for a Template-Controlled Cluster Growth.* The Journal of Physical Chemistry B, 2004. **108**(30): p. 10801-10811.

55. Pruneanu, S., Al-Said S. A., Liqin Dong, Tom A. Hollis, Miguel A. Galindo, Nicholas G. Wright, Andrew Houlton, Benjamin R. Horrocks,, *Self-Assembly of DNA-Templated Polypyrrole Nanowires: Spontaneous Formation of Conductive Nanoropes.* Advanced Functional Materials, 2008. **18**(16): p. 2444-2454.

56. Victor A. Bloomfield, *Condensation of DNA by multivalent cations: Considerations on mechanism.* Biopolymers, 1991. **31**(13): p. 1471-1481.

57. Kasyanenko, N., Afanasieva, D., Dribinsky, B., Mukhin, D., Nazarova, O., Panarin, E., *DNA interaction with synthetic polymers in solution.* Structural Chemistry, 2007. **18**(4): p. 519-525.

58. Dunlap, D., A. Maggi, M. Soria, and L. Monaco, *Nanoscopic structure of DNA condensed for gene delivery.* Nucl. Acids Res., 1997. **25**(15): p. 3095-3101.

59. Rakitin, A., Aich, P., Papadopoulos, C., Kobzar, Yu., Vedeneev, A. S., Lee, J. S., Xu, J. M., *Metallic Conduction through Engineered DNA: DNA Nanoelectronic Building Blocks.* Physical Review Letters, 2001. **86**(16): p. 3670 LP - 3673.

60. Nagarajan, R., Liu, W., Kumar, J., Tripathy, S.K., Bruno, F.F., Samuelson, L.A., *Manipulating DNA Conformation Using Intertwined Conducting Polymer Chains.* Macromolecules, 2001. **34**(12): p. 3921-3927.

61. Minjun Yan, G.H.B., *A quantitative method for dual-pass electrostatic force microscopy phase measurements.* Surface and Interface Analysis, 2007. **39**(4): p. 354-358.

62. Avlyanov, J.K., H.H. Kuhn, J.Y. Josefowicz, and A.G. MacDiarmid, *In-situ deposited thin films of polypyrrole: conformational changes induced by variation of dopant and substrate surface.* Synthetic Metals, International Conference on Science and Technology of Synthetic Metals, 1997. **84**(1-3): p. 153-154.

63. Jinyeol, K., Daewon SOHN SUNG, KIM, Y., Eung-Ryul, *Fabrication and characterization of conductive polypyrrole thin film prepared by in situ vapor-phase polymerization.* Synthetic metals, 2003. **132**(3): p. 309-313.

64. Wu, C.-G., Chen, C-Y *Chemical deposition of ordered conducting polypyrrole films on modified inorganic substrates.* J. Mater. Chem, 1997. **7**: p. 1409 - 1413.

65. Park, J.G., S.H. Lee, B. Kim, and Y.W. Park, *Electrical resistivity of polypyrrole nanotube measured by conductive scanning probe microscope: The role of contact force.* Applied Physics Letters, 2002. **81**(24): p. 4625-4627.

66. Bocharova, V., Kiriy, A. , Vinzelberg, H. , Mönch, I. , Stamm, M. , *Polypyrrole Nanowires Grown from Single Adsorbed Polyelectrolyte Molecules13.* Angewandte Chemie International Edition, 2005. **44**(39): p. 6391-6394.

67. Shaktawat, V., Jain, N., Saxena, R., Saxena, N.S., Sharma, K., Sharma, T.P., *Temperature dependence of electrical conduction in pure and doped polypyrrole.* Polymer Bulletin, 2006. **57**(4): p. 535-543.

68. Barde, W.S., S.V. Pakade, and S.P. Yawale, *Ionic conductivity in polypyrrole-poly (vinyl acetate) films synthesized by chemical oxidative polymerization method.* Journal of Non-Crystalline Solids, Non-Oxide and New Optical Glasses 15 - Proceedings of the 15th International Symposium on Non-Oxide Glasses and New Optical Glasses, 2007. **353**(13-15): p. 1460-1465.

69. Bof Bufon, C.C., Heinzel, T., *Transport properties of chemically synthesized polypyrrole thin films.* Physical Review B - Condensed Matter and Materials Physics, 2007. **76**(24).

70. Gence, L., et al., *Size related transport mechanisms in hybrid metal-polymer nanowires.* physica status solidi (a), 2008. **205**(6): p. 1447-1450.

71. Shen, J., et al., *Electrical properties of a single electrochemically template-synthesized polypyrrole nanowire.* Applied Physics Letters, 2006. **88**(25): p. 253106.

72. Spatz, J.P., et al., *Observation of crossover from three- to two-dimensional variable-range hopping in template-synthesized polypyrrole and polyaniline.* Physical Review B (Condensed Matter), 1994. **50**(20): p. 14888-14892.

73. Sandra C. Hernandez, D.C., Wilfred Chen, Nosang V. Myung, Ashok Mulchandani, *Single Polypyrrole Nanowire Ammonia Gas Sensor.* Electroanalysis, 2007. **19**(19-20): p. 2125-2130.

74. Tong, L., J. Lou, Z. Ye, G.T. Svacha, and E. Mazur, *Self-modulated taper drawing of silica nanowires.* Nanotechnology, 2005. **16**(9): p. 1445-1448.

75. Kohlman, R.S., T. Ishiguro, H. Kaneko, and A.J. Epstein, *Metallic state of polypryrrole: Effects of disorder.* Synthetic Metals, International Conference on Science and Technology of Synthetic Metals, Proceedings of the International Conference on Science and Technology of Synthetic Metals, 1995. **69**(1-3): p. 325-328.

76. Joo, J.L., J. K., Lee, S. Y., Jang, K. S., Oh, E. J., Epstein, A. J., *Physical characterization of electrochemically and chemically synthesized polypyrroles.* Macromolecules, 2000. **33**(14): p. 5131-5136.

77. Efros, A.L., Shklovskii, B. I., *Coulomb gap and low temperature conductivity of disordered systems.* Journal of Physics C: Solid State Physics, 1975. **8**(4): p. L49-L51.

78. Fogler, M.M., Teber, S., Shklovskii, B. I., *Variable-range hopping in quasi-one-dimensional electron crystals.* Physical Review B, 2004. **69**(3): p. 035413.

79. van Wees, B.J., et al., *Quantum ballistic and adiabatic electron transport studied with quantum point contacts.* Physical Review B, 1991. **43**(15): p. 12431.

80. Liqin, K. and et al., *Ballistic conductance calculation of atomic-scale nanowires of Au and Co.* Nanotechnology, 2007. **18**(9): p. 095709.

81. Maity, A.K., D. Nath, and D. Chakravorty, *Electrical conduction in nanocomposites of copper in silicate glasses.* Journal of Physics: Condensed Matter, 1996. **8**(31): p. 5717-5723.

82. Gu, Q., C. Cheng, and D.T. Haynie, *Cobalt metallization of DNA: toward magnetic nanowires.* Nanotechnology, 2005. **16**: p. 1358-1363.

83. Arakawa, H., J.F. Neault, and H.A. Tajmir-Riahi, *Silver(I) Complexes with DNA and RNA Studied by Fourier Transform Infrared Spectroscopy and Capillary Electrophoresis.* Biophysical Journal, 2001. **81**(3): p. 1580-1587.

84. Cui, S., Y. Liu, Z. Yang, and X. Wei, *Construction of silver nanowires on DNA template by an electrochemical technique.* Materials & Design, 2007. **28**(2): p. 722-725.

85. Berti, L., A. Alessandrini, and P. Facci, *DNA-Templated Photoinduced Silver Deposition.* Journal of the American Chemical Society, 2005. **127**(32): p. 11216-11217.

86. Park, S.H., M.W. Prior, T.H. LaBean, and G. Finkelstein, *Optimized fabrication and electrical analysis of silver nanowires templated on DNA molecules.* Applied Physics Letters, 2006. **89**(3): p. 033901.

87. Yin, Y., Li, Z. Y., Zhong, Z., Gates, B., Xia, Y., Venkateswaran, S., *Synthesis and characterization of stable aqueous dispersions of silver nanoparticles through the Tollens process.* Journal of Materials Chemistry, 2002. **12**(3): p. 522-527.

88. Alqudami, A. and S. Annapoorni, *Fluorescence From Metallic Silver and Iron Nanoparticles Prepared by Exploding Wire Technique.* Plasmonics, 2007. **2**(1): p. 5-13.

89. Xu, G.N., Qiao, X. , Qiu, X., Chen, J., *Preparation and characterization of stable monodisperse silver nanoparticles via photoreduction.* Colloids and Surfaces A: Physicochemical and Engineering Aspects, 2008. **320**(1-3): p. 222-226.

90. Barnes, W.L., A. Dereux, and T.W. Ebbesen, *Surface plasmon subwavelength optics.* Nature, 2003. **424**(6950): p. 824-830.

91. Zhang, W., X. Qiao, and J. Chen, *Synthesis and characterization of silver nanoparticles in AOT microemulsion system.* Chemical Physics, 2006. **330**(3): p. 495-500.

92. Tsuboi, M., *Application of Infrared Spectroscopy to Structure Studies of Nucleic Acids.* Applied Spectroscopy Reviews, 1970. **3**(1): p. 45 - 90.

93. Rivers, S.B., Bernhardt, G., Wright, M.W., Frankel, D.J., Steeves, M.M., Lad, R.J., *Structure, conductivity, and optical absorption of $Ag_{2-x}O$ films.* Thin Solid Films First International Symposium on Transparent Conducting Oxides, 2007. **515**(24): p. 8684-8688.

94. Mingru Z., Z.W., Hongxia Q., Lin Z., Hua Y., and Tiandong X., *Particle Size and Pore Structure Characterization of Silver Nanoparticles Prepared by Confined Arc Plasma.* Journal of Nanomaterials, 2009. **2009**: p. 5.

95. Lim, D.C., I. Lopez-Salido, and Y.D. Kim, *Size selectivity for CO-oxidation of Ag nanoparticles on highly ordered pyrolytic graphite (HOPG).* Surface Science, 2005. **598**(1-3): p. 96-103.

96. Boronin, A.I., Koscheev, S. V., Murzakhmetov, K. T. and V.I. Avdeev, Zhidomirov, G. M., *Associative oxygen species on the oxidized silver surface formed under O_2 microwave excitation.* Applied Surface Science, 2000. **165**(1): p. 9-14.

97. Tjeng, L.H., et al., *Electronic structure of Ag_2O.* Physical Review B, 1990. **41**(5): p. 3190 LP - 3199.

98. Hoflund, G.B., Z.F. Hazos, and G.N. Salaita, *Surface characterization study of Ag, AgO, and Ag_2O using x-ray photoelectron spectroscopy and electron energy-loss spectroscopy.* Physical Review B, 2000. **62**(16): p. 11126 LP - 11133.

99. Murray, B.J., Li, Q., Newberg, J. T., Menke, E. J., J.C. Hemminger, and R.M. Penner, *Shape- and Size-Selective Electrochemical Synthesis of Dispersed Silver(I) Oxide Colloids.* Nano Letters, 2005. **5**(11): p. 2319-2324.

100. Altieri, S., et al., *Charge fluctuations and image potential at oxide-metal interfaces.* Physical Review B, 2002. **66**(15): p. 155432.

101. Pruneanu, S., Olenic, Liliana, Al-Said, A. Said, G. Borodi, A. Houlton, and B. Horrocks, *Template and template-free preparation of one-dimensional metallic nanostructures.* Journal of Materials Science, 2010. **45**(12): p. 3151-3159.

102. Ida, Y., Watase, S., Shinagawa, T., Watanabe, M., , M. Chigane, M. Inaba, A. Tasaka, and M. Izaki, *Direct Electrodeposition of 1.46 eV Bandgap Silver(I) Oxide Semiconductor Films by Electrogenerated Acid.* Chemistry of Materials, 2008. **20**(4): p. 1254-1256.

103. Pierson, J.F. and C. Rousselot, *Stability of reactively sputtered silver oxide films.* Surface and Coatings Technology, 2005. **200**(1-4): p. 276-279.

104. Zhou, X., S.A. Dayeh, D. Aplin, D. Wang, and E.T. Yu. *Scanned electrical probe characterization of carrier transport behavior in InAs nanowires*. 2006: AVS.

105. Oliver, R.A., *Advances in AFM for the electrical characterization of semiconductors.* Reports on Progress in Physics, 2008. **71**(7): p. 076501.

106. Ijiro, K., Y. Matsuo, and Y. Hashimoto, *DNA-Based Silver Nanowires Fabricated by Electroless Plating.* Molecular Crystals and Liquid Crystals, 2006. **445**: p. 207 - 211.

107. Aleshin, A.N., *Quasi-one-dimensional transport in conducting polymer nanowires.* Physics of the Solid State, 2007. **49**(11): p. 2015-2033.

108. Jiaxing, H., V. Shabnam, H.W. Bruce, and B.K. Richard, *Nanostructured Polyaniline Sensors.* Chemistry - A European Journal, 2004. **10**(6): p. 1314-1319.

109. Fichou, D., G. Horowitz, B. Xu, and F. Garnier, *Stoichiometric control of the successive generation of the radical cation and dication of extended alpha-conjugated oligothiophenes: a quantitative model for doped polythiophene.* Synthetic Metals, 1990. **39**(2): p. 243-259.

110. Karim, M.R., K.T. Lim, C.J. Lee, and M.S. Lee, *A facile synthesis of polythiophene nanowires.* Synthetic Metals, 2007. **157**(22-23): p. 1008-1012.

111. Wang, J., et al., *Electrochemical fabrication of conducting polymer nanowires in an integrated microfluidic system.* Chemical Communications, 2006(29): p. 3075-3077.

112. Park, S., J. H. Lim, S. W. Chung, and C.A. Mirkin, *Self-Assembly of Mesoscopic Metal-Polymer Amphiphiles.* Science, 2004. **303**(5656): p. 348-351.

113. Kabela', M.a.H., P., *Na^{+}, Mg^{2+}, and Zn^{2+} Binding to All Tautomers of Adenine, Cytosine, and Thymine and the Eight Most Stable Keto/Enol Tautomers of Guanine: A Correlated ab Initio Quantum Chemical Study.* The Journal of Physical Chemistry B, 2006. **110**(29): p. 14515-14523.

114. Ma, Y., J. Zhang, G. Zhang, and H. He, *Polyaniline Nanowires on Si Surfaces Fabricated with DNA Templates.* J. Am. Chem. Soc., 2004. **126**(22): p. 7097-7101.

115. Niziurski-Mann, R.E., C. Scordilis-Kelley, T.L. Liu, M.P. Cava, and R.T. Carlin, *A mechanistic study of the electrochemical oxidation of 2,5-bis(2-thienyl)pyrroles.* Journal of the American Chemical Society, 1993. **115**(3): p. 887-891.

116. Al-Said, S.A., Hassanien, R., Hannant, J., Galindo, M. A., Pruneanu, S., Pike, A., Houlton, A., Horrocks, B. R., *Templating Ag on DNA/polymer hybrid nanowires: Control of the metal growth morphology using functional monomers.* Electrochemistry Communications, 2009. **11**(3): p. 550-553.

117. Zang, S. Q. and T.C.W. Mak, *Assembly of Silver(I);Organic Networks from Flexible Supramolecular Synthons with Pendant Ethynide Arms Attached to a Naphthyl Skeleton.* Inorganic Chemistry, 2008. **47**(16): p. 7094-7105.

118. Yangxin Z., M.F., James H., Cristian S., A. T. Johnson, Jr., Nicholas J. P., MacDiarmid, A. G. , *Fabrication and electrical characterization of polyaniline-based nanofibers with diameter below 30 nm.* Applied Physics Letters, 2003. **83**(18): p. 3800-3802.

119. Musa, A.O., T. Akomolafe, and M.J. Carter, *Production of cuprous oxide, a solar cell material, by thermal oxidation and a study of its physical and electrical properties.* Solar Energy Materials and Solar Cells, 1998. **51**(3-4): p. 305-316.

120. Zhang, J., Liu, J., Peng, Q., Wang, X., Li, Y., *Nearly Monodisperse Cu_2O and CuO Nanospheres; Preparation and Applications for Sensitive Gas Sensors.* Chemistry of Materials, 2006. **18**(4): p. 867-871.

121. Wang, W.Z., Wang, G.H. , Wang , X.S. , Zhan, Y.J. , Liu, Y.K., Zheng, C.L. , *Synthesis and Characterization of Cu_2O Nanowires by a Novel Reduction Route.* Advanced Materials, 2002. **14**(1): p. 67-69.

122. Gou, L. and C.J. Murphy, *Solution-Phase Synthesis of Cu_2O Nanocubes.* Nano Letters, 2002. **3**(2): p. 231-234.

123. Liu, X.M. and Y.C. Zhou, *Electrochemical deposition and characterization of Cu_2O nanowires.* Applied Physics A: Materials Science & Processing, 2005. **81**(4): p. 685-689.

124. Orel, Z.C., A. Anzlovar, G. Drazic, and M. Zigon, *Cuprous Oxide Nanowires Prepared by an Additive-Free Polyol Process.* Crystal Growth & Design, 2007. **7**(2): p. 453-458.

125. Alkoy, E.M. and P.J. Kelly, *The structure and properties of copper oxide and copper aluminium oxide coatings prepared by pulsed magnetron sputtering of powder targets.* Vacuum, 2005. **79**(3-4): p. 221-230.

126. Shishiyanu, S.T., T.S. Shishiyanu, and O.I. Lupan, *Novel NO_2 gas sensor based on cuprous oxide thin films.* Sensors and Actuators B: Chemical, 2006. **113**(1): p. 468-476.

127. Mathew, X., N.R. Mathews, and P.J. Sebastian, *Temperature dependence of the optical transitions in electrodeposited Cu2O thin films.* Solar Energy Materials and Solar Cells, 2001. **70**(3): p. 277-286.

128. Wang, L., et al., *Electrostatic assembly of Cu_2O nanoparticles on DNA templates.* Applied Surface Science, 2006. **252**(8): p. 2711-2716.

129. Borgohain, K., N. Murase, and S. Mahamuni, *Synthesis and properties of Cu_2O quantum particles.* Journal of Applied Physics, 2002. **92**(3): p. 1292-1297.

130. López-Macipe, A., J. Gómez-Morales, and R. Rodríguez-Clemente, *The Role of pH in the Adsorption of Citrate Ions on Hydroxyapatite.* Journal of Colloid and Interface Science, 1998. **200**(1): p. 114-120.

131. Das, K. and S.K. De, *Optical and photoconductivity studies of Cu_2O nanowires synthesized by solvothermal method.* Journal of Luminescence, 2009. **129**(9): p. 1015-1022.

132. Xu, L., Jiang, L. P., Zhu,J. J., *Sonochemical synthesis and photocatalysis of porous Cu_2O nanospheres with controllable structures.* Nanotechnology, 2009. **20**(4): p. 045605.

133. Jiang, X., T. Herricks, and Y. Xia, *CuO Nanowires Can Be Synthesized by Heating Copper Substrates in Air.* Nano Letters, 2002. **2**(12): p. 1333-1338.

134. Liu, X., B. Geng, Q. Du, J. Ma, and X. Liu, *Temperature-controlled self-assembled synthesis of CuO, Cu_2O and Cu nanoparticles through a single-precursor route.* Materials Science and Engineering: A, 2007. **448**(1-2): p. 7-14.

135. Nikesh, V.V., A.B. Mandale, K.R. Patil, and S. Mahamuni, *X-ray photoelectron spectroscopic investigations of Cu_2O nanoparticles.* Materials Research Bulletin, 2005. **40**(4): p. 694-700.

136. Ghodselahi, T., M.A. Vesaghi, A. Shafiekhani, A. Baghizadeh, and M. Lameii, *XPS study of the Cu Cu_2O core-shell nanoparticles.* Applied Surface Science, 2008. **255**(5, Part 2): p. 2730-2734.

137. Ghijsen, J.T., L. H.van Elp, J.Eskes, H.Westerink, J.Sawatzky, G. A.Czyzyk, M. T., *Electronic structure of Cu_2O and CuO.* Physical Review B, 1988. **38**(16): p. 11322 - 11330.

138. Cui, Y., X. Duan, J. Hu, and C.M. Lieber, *Doping and Electrical Transport in Silicon Nanowires.* The Journal of Physical Chemistry B, 2000. **104**(22): p. 5213-5216.